8-26-2015

Three-Dimensional Microstructural Imaging and Charge Transport Modeling Tools for Fuel Cell Materials

Matthew B. DeGostin
mdegostin1@gmail.com

Three-Dimensional Microstructural Imaging and Charge Transport Modeling Tools for Fuel Cell Materials

Matthew Barra DeGostin

B.S.E., University of Connecticut, 2013

A Thesis

Submitted in Partial Fulfillment of the

Requirements for the Degree of

Master of Science

At the

University of Connecticut

2015

APPROVAL PAGE

Master of Science Thesis

Three-Dimensional Microstructural Imaging and Charge Transport Modeling Tools for Fuel Cell Materials

Presented by

Matthew Barra DeGostin, B.S.E.

Major Advisor_____
Wilson K.S. Chiu

Associate Advisor_____
Brice N. Cassenti

Associate Advisor_____
Michael T. Pettes

University of Connecticut

2015

Acknowledgments:

I would like to offer my deepest gratitude to a number of people, without whom this thesis would not have been possible.

First, I would like to thank my advisor, Professor Wilson Chiu, for his guidance, insight, and support as I have continued to learn and grow as both a student and person. In addition to Professor Chiu, I am very thankful for the support of Professor Brice Cassenti and Dr. Aldo Peracchio, who have patiently guided me through many complicated tasks and who continue to inspire me with their many years of wisdom and experience. I owe many thanks to the past and present members of my research group, including (in Alphabetical order): Alex Cocco, Dr. William Harris, Dr. Andrew Kiss, Dr. Timothy Myles, Dr. Arata Nakajo, Professor George Nelson, Dr. Mar Pérez-Fortes, and many others who have come and gone during my time here. I would also like to thank my advisory committee, Professor Chiu, Professor Cassenti, and Professor Michael Pettes for their efforts.

I would like to acknowledge the support of the beamline scientists who have made the imaging work in this thesis possible: Dr. Jun Wang and Dr. Yu-Chen Karen Chen-Wiegart at the National Synchrotron Light Source, and Dr. Yijin Liu at the Stanford Synchrotron Radiation Lightsource. Additionally, electrospun membrane studies would not have been possible without the support of Dr. Cynthia Lundgren, Dr. Deryn Chu, and Dr. Kyle N. Grew of the U.S. Army Research Laboratory, and Professor Peter Pintauro of Vanderbilt University.

I am grateful for financial support from a number of organizations, including an Energy Frontier Research Center on Science Based Nano-Structure Design and Synthesis of Heterogeneous Functional Materials for Energy Systems (HeteroFoaM Center) funded by the U.S. Department of Energy (Award DE-SC0001061) and the National Science Foundation

(Award CBET-1134052). Financial support from the Army Research Office (award number W911NF-14-1-0298) is also gratefully acknowledged.

Last but not least, I am forever grateful for the support provided to me by my family and friends over the years, whose love and encouragement make all the difference.

Table of Contents

Abstract

Fuel cells and other electrochemical energy storage and conversion technologies are increasingly being used as clean energy alternatives for mobile and stationary power generation. The viability of fuel cells as a marketable energy source continues to benefit from improvements in performance, longevity, and cost. Each of these factors is intimately linked to the performance of materials which constitute these systems, leading to significant research dedicated to optimization of underlying fuel cell components and materials. One common fuel cell type is the polymer electrolyte membrane fuel cell, which is a low temperature device reliant on efficient ion transport and mechanical stability of a solid polymer electrolyte which separates the cell's electrodes. Recent advances in polymer electrolyte fabrication have resulted from the use of a technique called electrospinning, where ion conducting polymer nanofibers are compacted together with an inert supporting matrix, leading to highly conductive and durable membranes. Another common fuel cell type is the solid oxide fuel cell, which utilizes a solid ceramic electrolyte and high operating temperatures to drive charge transport and electrochemical reactions. A commonality among these devices is their reliance on effective transport of ions, electrons, and gases through three-dimensional transport networks that have complex underlying structures, often on the micro- and nano-scales. The present work is dedicated to aiding in fuel cell materials design by developing methods which elucidate the role of three-dimensional microstructure in transport. Digital representations of fuel cell material microstructure are first obtained by either a) artificially generating ideal structures that mimic the behavior of the real system or b) imaging real microstructure samples by a three-dimensional imaging technique, synchrotron-based x-ray nanotomography. An existing charge transport model, called Electrochemical Fin Theory, based on extended surface fin analysis is then adapted for the study

of three-dimensional structures relevant to solid oxide and electrospun polymer electrolyte membrane fuel cells. For each case study, existing transport models are also adapted to determine the applicability and microstructural sensitivity of the new modeling tool. The application and validation of this electrochemical fin modeling approach showcases the benefits of using this technique, which include sensitivity to local inhomogeneities, and significantly reduced computational requirements when compared to traditional mesh-based numerical simulations. Results from these studies are used to obtain a better understanding of how fuel cell microstructure affects species transport.

Chapter 1: Introduction

1.1 Fuel Cells

A fuel cell is a type of electrochemical device that generates electricity via chemical reactions. There are many advantages of fuel cells that make them promising devices for energy storage and conversion, including: high efficiency, mechanical simplicity (i.e. limited moving parts), low emissions, and application diversity [1]. The main disadvantages of current fuel cells are their cost, and the difficulty in storage and accessibility of hydrogen for fuel. One common reason for the high cost of manufacturing and upkeep of fuel cells is the use of precious materials such as platinum for catalysts; however different cost issues arise depending on the type of fuel cell that is being used.

In general, a basic fuel cell consists of an anode, cathode, and electrolyte. The anode typically takes in a fuel such as hydrogen gas, whereupon its electrons are stripped by a chemical reaction and travel through an external circuit to the cathode, thus producing power [1]. In a proton exchange membrane fuel cell (PEMFC), these electrons combine with oxygen that is flowed in to the cathode to form water. To complete this cycle, the positively charged hydrogen ions (i.e. protons) produced in the anode flow through the electrolyte, which must only permit the appropriate ions to flow in order for the cell to operate effectively. If electrons or gas are allowed to travel through the electrolyte, the chemical reactions in each electrode will be disrupted and cell performance will decrease.

The specific reactions that occur in both the anode and cathode are dependent on the type of fuel cell that is being used. Fuel cells are often classified by their electrolyte; however other factors such as the transported ion and the cell's operating temperature may often be applied for classification. Below, two main classifications of fuel cells will be discussed with regard to current challenges and ongoing research; solid oxide fuel cells (SOFC) and polymer electrolyte membrane (PEM) fuel cells. The two types of PEM fuel cells that will be focused on are the PEMFC and alkaline anion exchange membrane fuel cell (AAEMFC).

1.2 Solid Oxide Fuel Cells

1.2.1 Overview

A simple schematic for a SOFC is shown in Fig. 1.1. The defining component of the SOFC is its solid oxide electrolyte, which is typically a ceramic such as yttria-stabilized zirconia (YSZ) [2]. At high temperatures (600-1000°C), this electrolyte allows the conduction of oxygen anions, which are produced by reactions with electrons at its interface with an electron conducting cathode material, such as lanthanum strontium manganite (LSM), and a pore phase which allows the flow of oxygen (O_2) molecules. These oxygen anions travel through the solid electrolyte into the porous anode, where they combine with a fuel such as hydrogen to produce water and lose electrons to an external circuit, thus producing power. Similar to the cathode, the chemical reaction in the anode requires interfaces between the electrolyte material, an electron conducting material (typically Ni), and a pore phase that allows the flow of fuel. These reaction sites are often referred to as triple phase boundaries (TPB), and are critical to SOFC functionality [3].

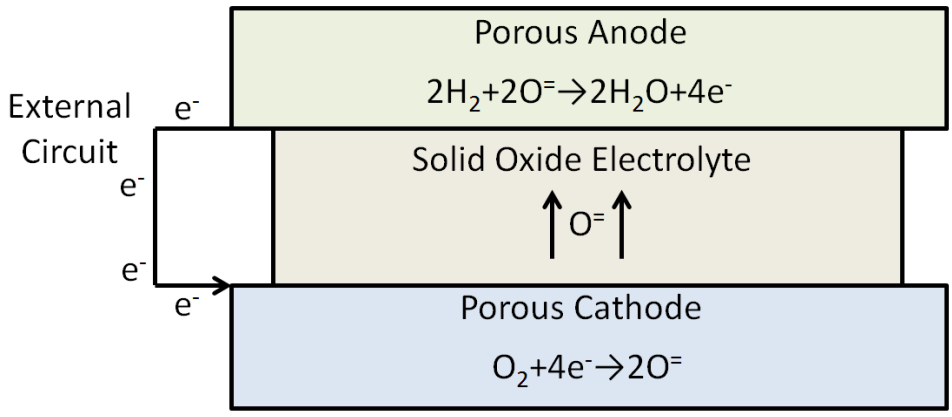

Figure 1.1. A simple diagram of a solid oxide fuel cell and its basic components.

1.2.2* Challenges and Motivation

***Adapted from** [4]

Three immediate benefits of SOFCs are the result of its high operating temperatures; high reaction rates can be achieved without the use of precious catalyst materials, fuel flexibility is achieved via internal reformation in the cell, and the heat from the cell may be used for co-generation resulting in improved system efficiencies. However, the SOFC does not come without its disadvantages. The ceramic materials that are used can be expensive to manufacture and handle [1], resulting in high costs compared to other available energy technologies. High operating temperatures result in longer startup times for the cells and often require the use of more elaborate cooling systems. These high temperatures also can lead to degradation of the cell, via thermal cycling or material mobility over longer operating cycles.

Because of the issues encountered with manufacturing and operating SOFCs, significant research has been performed to reduce costs of these systems, by improving efficiencies and optimizing the use of constituent materials. One growing area of interest is the improvement of the

electrodes which drive SOFC functionality. Advanced electrodes have continuously been developed which combine traditionally-used or new electrode materials with inventive fabrication techniques, resulting in complex electrodes that often have unique structures on the micro and nano-scales [5]. SOFC electrodes should always have high ion and electron conductivities, sufficient porosity for the diffusion of gas, high density of active TPBs for electrochemical reactions, structural support, and good long-term stability [6]. To achieve these goals, one commonly studied electrode structure is the composite electrode, which is fabricated by sintering of ion conducting (YSZ) and electron conducting (LSM or Ni) particles at high temperatures. This type of structure allows ions to flow through the sintered electrolyte particles into the porous electrodes, allowing active TPBs to exist beyond the bulk electrode-electrolyte interfaces [6].

Regardless of the electrode structure studied, the ability of electrode material systems to function effectively is strongly dependent on their underlying microstructure, specifically the composition and location of distinct material phases and relevant interfaces at the micro and nano-scales [7], [8]. In the past few decades, understanding the complex relationship between microstructure and performance has become a focus in the scientific community, with hopes of enabling more intelligent design of such systems for next generation devices [8]. As computing systems have drastically improved, computational modeling tools have also been developed and expanded to aid in experimental electrode fabrication efforts, due to the wide range of microstructures that can be studied computationally and the greater understanding of underlying mechanisms that can be achieved. However, existing modeling tools used to study transport and reactions in complex material systems are not perfect, and often have characteristics that limit their applicability. A

number of the models currently being used are presented here, to highlight the benefits and potential limitations of each with regard to modeling of microstructural transport networks and the design of advanced SOFC electrodes.

Arguably the most common means of modeling microstructural effects on transport and reaction site accessibility in SOFC electrodes is via volume averaged or effective structural properties that describe the behavior of a microstructural network. Effective ionic and electronic conductivities as well as gas diffusivity are all targeted with this approach, and fuel cell performance models that are used to determine the behavior of an entire SOFC system are generally modified via these effective parameters to account for microstructure. To determine these effective transport properties of a range of electrodes, a host of methods have been employed. The quickest way to get an estimate for effective properties is with simplified analytical models such as effective medium theory (EMT) [6], [9] or percolation theory [10]. These types of models typically require describing complex microstructures with a few structural parameters such as volume fraction or average feature size. The main draw of these models is their ease of use and minimal computation requirement; an estimate for effective conductivity or diffusivity of a structure can often be obtained by simply solving a single equation with knowledge of one or two structural parameters. However, these analytical approaches do not allow local effects of specific microstructural configurations to be considered and instead rely on homogeneous, averaged representation of structure.

In the SOFC literature, percolation theory has been adapted by numerous authors [10]–[14] to study microstructural effects on performance by accounting for the percolation effect; that is

when an insufficient amount of a phase is present in an electrode, efficient transport may not occur because of a lack of transport pathways. While some researchers have developed enhancements to percolation theories to account for additional phases or more complex electrode sintering mechanisms [15], [16], the structures that percolation theory considers are assumed to be randomly generated and homogeneously mixed dispersions of spherical particles. In real electrodes, different fabrication methods and conditions may produce structures which are heterogeneous and thus not accurately represented by a homogeneous mixture [17], [18]. In addition, effective properties derived from percolation theory assume an infinitely large domain and thus are based on statistical approximations, which may deviate from structures with heterogeneous transport networks on length-scales relevant to SOFC electrodes.

In order to further understand the effects that local microstructural networks may have on electrode performance, several researchers have numerically generated random lattices and packings of spherical particles as a basis for resistor network calculations utilizing Kirchhoff's circuit laws [19]–[23]. This approach has been used to compute effective transport properties required for system-level performance models [19], [22], as well as polarization resistances which take into account the presence of electrochemical reactions [20]. The resistor network model approach enables discrete structures to be analyzed and local distributions of species and reactions to be determined, however typical resistor network calculations still make the assumption of resistive elements being only spherical in shape or having uniform geometrical features such as inter-particle neck size throughout the entire domain.

A recent trend in SOFC research, as well as materials research in a number of other fields, is an increased interest in studying real three-dimensional microstructures as a means of better understanding the local morphologies of material systems [24]. Before imaging methods were capable of discerning microstructural features in three dimensions, researchers would often have to rely on the aforementioned transport models and were therefore limited to simple representations of complex microstructures. With the recent advancement of three-dimensional imaging techniques for energy materials such as focused ion beam-scanning electron microscopy (FIB-SEM) and x-ray computed nanotomography (XNT) [24], researchers have been able to generate and analyze microstructures by direct imaging of real material samples. There has been a significant amount of research dedicated to measuring microstructural parameters directly from this data such as density of TPB sites, tortuosity, and phase size distributions which can be used in continuum-level models. Digitized representative domains obtained via imaging have also been used to estimate effective transport properties with a wide range of methods, including random-walk [25]–[27], finite volume [28]–[30], and finite element methods [25], [31]–[33]. Representative volume elements (RVE) of SOFC electrodes have also been used as numerical domains for advanced modeling techniques such as lattice Boltzmann methods [34]–[37], which eliminate the need for measurement of effective or volume averaged transport properties and instead model electrochemical performance directly from a given structure. The benefits to using such detailed numerical approaches are their ability to resolve effects of minute structural details, as long as a sufficient mesh is used, and their ability to account for more detailed physics. Electrode structures fabricated via traditional methods such as high-temperature sintering and compaction often have highly amorphous transport pathways and heterogeneous dispersions of reaction sites, which make them good candidates for numerical studies. However, while these

and other related multi-physics simulations with sensitivity to local structure are useful for studying microstructural effects, the dense grids required to delineate local features often significantly increase computational requirements and limit the size of the structure that may be studied. In this regard, promising improvements are being made to mesh-based and particle-based simulations which can reduce the computational requirements of detailed numerical simulations for future design efforts [38].

1.3 Polymer Electrolyte Membrane Fuel Cells

1.3.1 Overview

PEM fuel cells get their name from the solid polymer electrolyte membranes that are critical to their functionality. The two types of PEM fuel cells that are discussed in this work are the PEMFC and the AAEMFC. The basic principles of these two PEM fuel cell types are the same; however there are some crucial differences between the two, including the ion which conducts between electrodes. As described in Section 1.1, and shown in Fig. 1.2a, the PEMFC allows positive hydrogen ions (H^+) to form in the cathode and flow to the anode through the PEM [1]. Alkaline anion exchange membrane fuel cells, on the other hand, require hydroxide ions (OH^-) to first be formed in the cathode, whereupon the anion exchange membrane (AEM) carries them to the anode to be converted into H_2O and release electrons. A schematic of the AAEMFC system is shown in Fig. 1.2b. Another significant difference between PEMFC and AAEMFC is that due to the alkaline conditions of an AAEMFC, cathodic reactions occur more readily, thus overcoming the traditionally high activation overpotential found in PEMFCs. This difference can manifest itself in the use of less expensive metal catalysts than platinum in the electrodes of AAEMFCs.

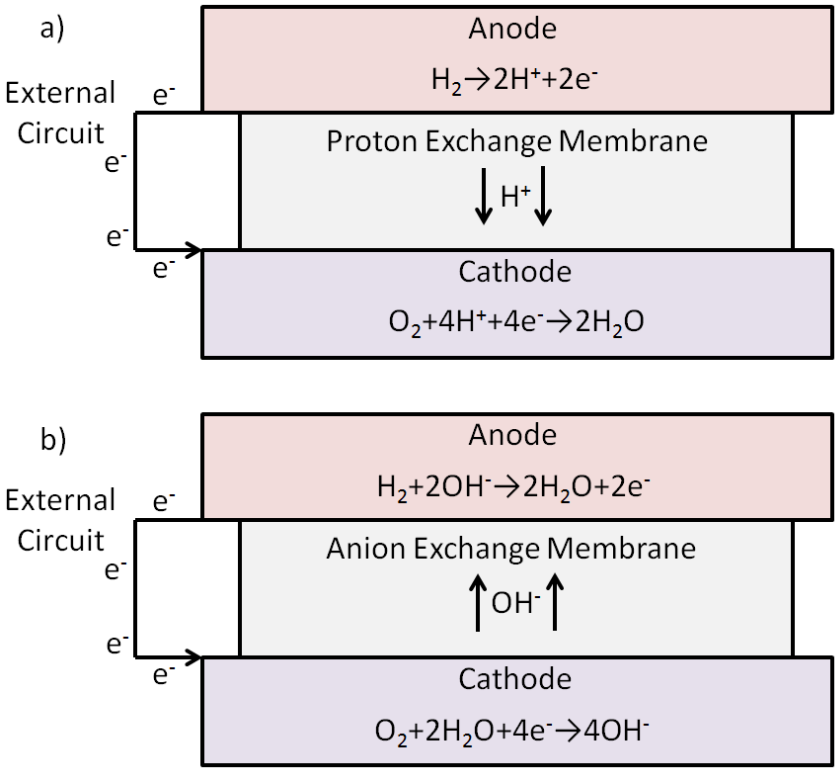

Figure 1.2. Simple diagrams for the a) proton exchange membrane fuel cell, and b) alkaline anion exchange membrane fuel cell.

In both types of PEM fuel cell, the anode, cathode, and polymer electrolyte form the membrane electrode assembly (MEA), which is typically connected in series with additional MEAs between two current collectors for increased power output. Catalyst layers, gas diffusion layers, and flow channels are also used in a PEM fuel cell to facilitate reactions, control membrane hydration, and flow fuel, respectively. In terms of applications, PEM fuel cells run the gamut from portable power applications to combined heat and power systems and as power sources for cars and buses [1].

1.3.2 Challenges and Motivation

In addition to the aforementioned challenges faced with fuel cell design and implementation, PEM fuel cells offer additional challenges to current researchers. One of the most critical issues in PEM fuel cell operation is water management [1]. Ion conduction in the PEM can only be achieved when the electrolyte is hydrated. However, if too much water is present in the MEA, the pores in the electrodes or the gas diffusion layers can become flooded, therefore blocking the passage of fuel to catalyst sites. Ensuring a proper balance of water in the MEA remains a primary design consideration for PEM fuel cell systems. However, in the case of an ideally hydrated membrane, sufficient ion conduction and mechanical stability of the PEM still remains an issue, especially for AAEMFCs [39]–[43].

Membranes for PEMFC and AAEMFC applications are consistently being fabricated and tested to overcome these challenges, ranging from commercial membranes such as Dupont's Nafion [44] and GORE-SELECT [45] for PEMFCs to many independently fabricated membranes [46], [47]. Commercialization of AEMs remains complicated by a number of factors including stability, CO_2 effects, and the lower conductivity of OH^- in bulk water than that of H^+ largely due to the lower mobility of OH^- ions. To improve ionic conductivities, the ion exchange capacity of AEMs is often increased during fabrication, which can lead to increased membrane swelling in the presence of water and decreased mechanical stability. Effective membranes should thus maintain a balance between having high ionic conductivities while also remaining resilient to mechanical degradation.

Recently, a fabrication technique called electrospinning has been used to generate PEMs for fuel cell applications [47]–[53]. Among the many reasons for the increase in popularity of this technique are its ease of use, high versatility, and associated control over membrane morphology. In many of these studies, ion exchange membranes (IEM) are fabricated by spinning a highly conductive ionomer nanofiber (composed of, e.g., Nafion) with an inert, hydrophobic fiber and processing the membranes to produce highly inter-connected three-dimensional networks of ion conducting fibers completely surrounded by a mechanically supportive uncharged matrix [51]. In addition to the wide range of polymeric materials that can be used in the process [54]–[56], electrospinning offers control over membrane volume fraction [48], [51], [52], nanofiber diameter [51], [57]–[59], internal fiber morphology [54], [57], and fiber orientation [54]. Electrospun membranes are a unique class of PEMs due to the unique conducting fiber networks that can result from the fabrication process.

To aid in the development of PEM technologies, significant experimental and computational modeling efforts have been directed at obtaining a better understanding of the transport processes involved during PEM fuel cell operation under a wide range of conditions [39], [60]–[68]. The types of models that are employed to study PEM transport often fall under two categories: microscopic and macroscopic approaches [60]. In both cases, a range of mechanisms for charge transport have been proposed and modeled, including the Grotthuss mechanism, convective processes, bulk diffusion, migration, and surface site hopping [64]. These mechanisms are assumed to be present in the case of H^+ transport in proton exchange membranes as well as OH^- transport in AEMs; however, the presence of any CO_2 in a real AEM, resulting in the conversion of OH^- to the less mobile carbonate and bicarbonate species [39], can complicate the modeling

process. The challenging task of modeling all relevant transport processes in PEMs is further complicated by accurately modeling the effects of microstructure on transport [60], [64]. Microscopic and macroscopic models differ in how they handle microstructural effects. Microscopic models such as molecular dynamics simulations will often attempt to simulate the real polymer material microstructure and underlying transport pathways, based on numerical reconstructions of the polymer structure [69], [70]. On the other hand, macroscopic approaches generally neglect the exact morphological details of the PEM microstructure and instead rely on treating the membrane as a homogeneous medium whose microstructure can be described by simple parameters such as porosity, or by application of macrohomogeneous models such as EMT [71]–[74] or percolation theory [75]–[77]. In some modeling studies, the role of microstructure in PEMs is delegated to fitting parameters which are determined by comparing to experimental data [62], [64].

In the case of electrospun membranes, it is expected that membrane morphologies resulting from the electrospinning process could exhibit transport behavior that is different from traditionally fabricated PEMs. In addition to electrospun nanofibers being composed of a polymer material whose transport behavior may be modeled by the aforementioned approaches, the three-dimensional fibrous transport networks that result from the fabrication process may also affect membrane conductivity. Existing transport models may not be able to properly account for these fibrous network structures; therefore, it is of interest to model the changes in membrane conductivity associated with electrospun membrane morphologies.

1.4 Characterization Methods

1.4.1 Three-Dimensional Microstructural Imaging

The first method used extensively in this work to characterize fuel cell material microstructures is three-dimensional microstructural imaging. According to Cocco et al. [24], a host of materials used in energy conversion and storage technologies such as batteries, fuel cells, solar cells, and catalysts, have been increasingly studied via numerous three-dimensional imaging techniques to resolve intricate details of their structure on the micro and nano-scales. Local imaging methods such as magnetic resonance imaging, x-ray tomography, and FIB-SEM have been used extensively to study fuel cell materials, and are often accompanied by modeling simulations or are used *in situ* to study cell operation and degradation under realistic operating conditions [24].

Synchrotron-based x-ray computed nanotomography (XNT) is used primarily to study SOFC electrode microstructures in this work. This technique, which utilizes high-brilliance synchrotron transmission x-ray microscopes, is a non-destructive method to obtain three-dimensional digital renderings of a sample material, with spatial resolutions on the order of tens of nanometers. A more detailed description of the experimental setup and image processing techniques is discussed in Chapter 2. In addition to the high spatial resolutions that can be achieved with this technique, other information can be extracted including elemental speciation and chemical bonding information. Izzo et al. [78] have used XNT to obtain digitally reconstructed images of the solid and pore phases in a real SOFC anode sample. They were able to use these three-dimensional renderings in numerical simulations of pore phase tortuosity, which is a critical parameter for many microstructural transport models. Using a technique called differential x-ray absorption contrast imaging, Nelson et al. [79] were able to distinguish

the two solid phase, LSM and YSZ, of a SOFC cathode sample. Using this distinction, the locations of TPBs in the structure were able to be tracked and quantified. The XNT procedures used in these works and others studying SOFC microstructures [31], [80]–[82] are utilized here, and are critical to exploring the applicability of the transport models developed and employed in this thesis.

1.4.2* Electrochemical Fin Theory

***Adapted from** [4]

After three-dimensional imaging is performed, characterization of fuel cell microstructures is further carried out by the adaption of an existing charge transport model, electrochemical fin (ECF) theory, first proposed by Nelson et al. [83] in 2011. The purpose of this section is to give a brief overview of electrochemical fin theory and its underlying assumptions; a more detailed description of the theory can be found in Ref. [83]. The initial motivation for the development of electrochemical fin theory was to provide a preliminary design screening tool for advanced electrode design, allowing detailed mesh-based numerical simulations and design optimization to be performed on only the most promising electrode microstructures.

The basic case for an electrochemical fin expands on the work of Tanner et al. [84] and is shown in Fig. 1.3. Prior to defining the governing equations, a number of key assumptions must be noted. First, charge transport through a fin is treated as one-dimensional between the base and tip end areas. This assumption has been shown to maintain accuracy for most axisymmetric geometries, however in the case of fins that contain exceptionally narrow regions or inter-particle necks, charge transfer is over-estimated [83], [85]. External gas transport is assumed to be fast,

thus the concentration of gas species (i.e., fuel) does not vary along the outer surface of the fin. This allows electrochemical surface reactions to be represented by a single scalar charge transfer resistance parameter [83] if the phase of interest is assumed to conduct both ions and electrons (as is the case for mixed ionic-electronic conducting materials). Furthermore, it has been shown experimentally that the electron electrochemical potential in the electronic conducting phase of most composite electrodes or in single solid phase mixed ionic and electronic conducting materials is nearly constant [10], [12], [84], [86]. Therefore, electrochemical fin theory is only used here to model ionic conduction, while electronic conduction and the more complicated mixed-conduction problem are neglected. Finally, space charge effects on ionic transport that can occur near grain boundaries are ignored in this formulation. Nelson et al. [85] have assessed the effects of space charge regions and found that they become significant for very small particles or at highly constrictive inter-particle necks.

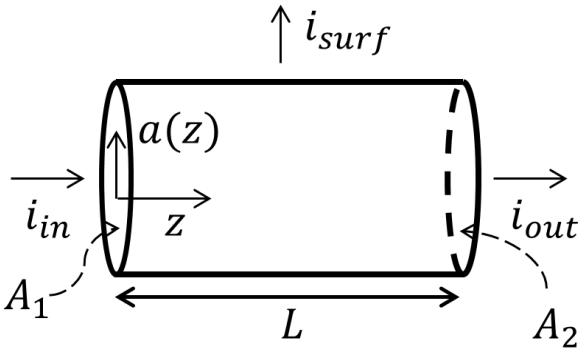

Figure 1.3. An electrochemical fin of constant cross-section and associated geometric parameters. This figure is from Ref. [4].

Beginning with Ohm's law to represent current flow and performing a charge balance on a differential fin element, the governing ODE for charge transport and surface electrochemistry of an axisymmetric fin is shown by Eq. 1.1.

$$a^2(z)\frac{d^2\varphi}{dz^2} + 2a(z)\frac{da}{dz}\frac{d\varphi}{dz} - \frac{2a(z)}{\sigma R}\sqrt{1+\left(\frac{da}{dz}\right)^2}\,\varphi = 0 \tag{1.1}$$

Here, the material properties of the fin, intrinsic conductivity σ and charge transfer resistance R do not vary along the length of the fin. The boundary conditions that can be specified for each fin are a fixed potential or fixed current. The fin's radial profile is defined by the function $a(z)$, where z is the primary transport direction and a is the axisymmetric fin radius. A key component of electrochemical fin theory is the existence of a number of analytical solutions governing the potential, φ, for a range of axisymmetric geometries [87]. Details of the geometries and their corresponding closed-form solutions are given in Chapters 3 and 4, where applicable.

1.5 Goals and Objectives

The remainder of this thesis is dedicated to presenting and validating a method for the characterization and modeling of fuel cell material microstructure, and its effects on charge transport. This begins with Chapter 2, which presents a more detailed description of the XNT imaging technique mentioned in Section 1.4.1. The imaging procedure and critical image processing steps such as filtering and segmentation of reconstructed images are discussed. This type of imaging process is critical to obtaining digitized volumes of real microstructure samples, which are necessary for validation of the transport models used herein.

Chapter 3 describes one case study for charge transport modeling that is focused on SOFC electrode materials. Real microstructures obtained by XNT as well as ideal, artificial structures are studied with respect to charge transport. A unique tool is presented that performs discretization of three-dimensional digital volumes into discrete charge-conducting channels, allowing the direct application of electrochemical fin theory for analysis of ionic conductivity. A volume-averaged model, percolation theory, as well as mesh-based finite element simulations are compared to the electrochemical fin approach, highlighting its advantages and drawbacks as a microstructural modeling tool for both simple and complex structures.

Chapter 4 presents a newly developed model, the Fiber Network (FN) model, which is based on electrochemical fin theory and utilized for the analysis of charge transport in electrospun PEMs. This model aims to numerically generate membranes that are representative of those resulting from a real electrospinning process, whereupon ionic conductivity can be found for the constructed fibrous networks. The goal of this method is to explain the effects that fiber network morphologies might have on PEM charge transport, without considering the detailed effects of transport within each individual fiber. The FN model is compared to published experimental data and other common transport models for predicting membrane conductivities, including EMT and Porous Media Theory, showcasing the importance of capturing the unique microstructural characteristics of electrospun membranes. Results from the FN model are then used to develop a new analytical conductivity model for electrospun membranes, which only requires estimation of a few structural parameters and can accurately predict average membrane conductivity trends considering the effects of fibrous network microstructures.

Chapter 2*: Synchrotron-Based Transmission X-ray Microscopy

***Adapted from** [88]

2.1 Experimental Set-up and Imaging Procedure

In this work, transmission x-ray microscopy (TXM) using a synchrotron x-ray source is used to obtain three-dimensional digital images of fuel cell material samples. The basic configuration for the imaging setup is shown in Fig. 2.1, which is adapted from [89]. In this setup, monochromatic x-rays are directed onto a material sample via a capillary condenser lens, and unfocused x-rays are blocked via a beam stop and pin hole. X-rays that are transmitted through the sample are focused by a Fresnel zone plate objective lens and magnified onto a CCD camera [90] to obtain a transmission image of the sample. This imaging setup is continually benefitted by hardware improvements such as more advanced optics, and continues to improve by the implementation of next generation, high-brilliance synchrotron sources. The current spatial resolutions obtainable by these nano-scale imaging systems are around 17 nm [91].

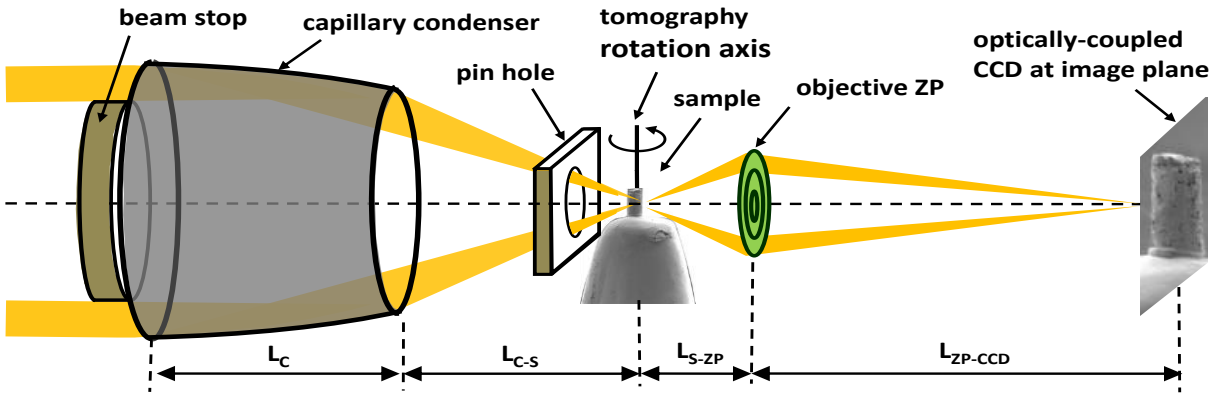

Figure 2.1. A typical synchrotron-based TXM configuration, adapted from [89].

To obtain three-dimensional images of samples, tomographic reconstruction techniques are used. A more detailed description of tomography is given in Section 2.2.1, however the basic experimental imaging procedure is as follows. Using the TXM, projection (transmission) images are taken at a large number of angles that span a 180° sample rotation. After each single projection image is taken, the sample, which is mounted on a stage capable of translation and rotation, is rotated by a small angular increment. The exposure time for each projection image is chosen so that a sufficient amount of x-rays passes through the sample. Once every projection image is taken, the projections can then be processed further. In order to remove background noise from the image, a reference image is generally taken before and after acquisition of the entire imaging data set.

One of the benefits of using a synchrotron x-ray source for TXM is the tunability of the hard x-ray beam's energy. Tuning the x-ray energy allows a sample's constituent phases to be identified since different material phases will often have different x-ray absorption properties at a given energy. Elemental absorption edges are particularly useful, since individual material phases will often exhibit sharp contrast changes across a small x-ray energy range. There are two common imaging techniques that utilize these contrast changes to identify different material phases across an absorption edge; these are differential x-ray absorption contrast imaging [82], and x-ray absorption near-edge structure tomography [89], [92]. A key to these imaging procedures is that samples are created to suit the imaging setup and tomographic reconstruction process. The materials that are being studied, and resulting sample dimensions, must be chosen carefully so that their absorptive properties (i.e. x-ray attenuation lengths) allow sufficiently many photons to pass through the sample during image acquisition. To fabricate samples, FIB-

SEM has been increasingly used because of its precision in extracting and mounting small samples with specific geometries [93]. For the materials studied in this thesis, cylindrical samples of roughly 10 μm diameter and 20 μm height were created and imaged in the TXM.

2.2 Image Processing

The ultimate goal of synchrotron-based XNT is to obtain digital three-dimensional images of a material's interior structure, where each distinguishable material phase is distinctly labeled. To reach this goal, once images are obtained via the experimental setup and procedure outlined above, they must be processed further by a number of steps. These steps often include tomographic reconstruction, filtering, and image segmentation. A brief introduction of these steps and commonly used processing techniques will be discussed in the following sections.

2.2.1 Tomographic Reconstruction of Projection Images

The first step in processing TXM projection images is tomographic reconstruction. The goal of this process is to obtain images of the interior of a sample given a sufficient number of projection images. Each projection image, taken at a certain angle, is said to be composed of a set of line integrals which represent the attenuation behavior of the sample (i.e. the total attenuation, or absorption, of the x-rays that passed through the sample at that point). Once tomographic reconstruction has been performed, what results is a 3-D mapping of the attenuation of the sample, such that material phases with distinct attenuation lengths can be distinguished in 3-D (resulting in phase differentiation).

The goal of tomographic reconstruction is to determine an unknown function (i.e. the interior image of a sample), by inverting the Radon transform that represents the sample (in this case, the Radon transform is the set of all line integrals from all projection images obtained in the imaging procedure). A number of tomographic reconstruction algorithms have been developed and used to invert the Radon transform, including the iterative Algebraic Reconstruction Technique (i-Art), filtered back-projection (FBP), and more recently developed algorithms such as maximum likelihood with expectation maximization (MLEM) [94]–[99]. A common step in applying these algorithms is ensuring all projection images of a sample are aligned about a single rotational axis. In this work, fiducial markers (e.g., gold particles) are attached to cylindrical samples during preparation to allow manual alignment of projection images after acquisition.

2.2.2 Filtering

Once the interior of a sample is reconstructed by one of the above mentioned methods, a number of artifacts may be present that are not indicative of the actual material present in the sample. These artifacts can include pixilation or noise, streaks, and non-uniformity of brightness, among others [100]. Many factors can cause the presence of these artifacts, including the image acquisition itself (beam drift, unfocused optics, etc.), or imperfect image alignment prior to reconstruction. These issues can eventually impact segmentation of the images and result in inaccurate labeling of a material's phases. If voxels are inaccurately labeled, transport modeling and structural property measurements will no longer be indicative of the actual material.

Filtering is the process of digitally removing artifacts in a reconstructed image and enhancing image quality, which aids the segmentation procedure to yield the most accurate representation

of the original sample possible. A more detailed discussion on filtering techniques can be found in [101]; here, only the more common techniques are discussed.

The type of filtering that is applied to an image is dependent on the state of the image once it has been reconstructed, as well as the obvious presence of artifacts that would affect the segmentation process. Most of the aforementioned artifacts including streaks, noise, and pixilation, can be significantly reduced with smoothing filters. Two common smoothing filters that are used are a Gaussian filter and a median filter. A Gaussian filter, also known as a Gaussian blur, is a low-pass filter that imposes a voxel-by-voxel transformation according to a Gaussian function with a specified radius. A median filter, as the name implies, finds the median gray-scale value within a specified neighborhood of the voxel of interest, and replaces the voxel's value with that median. Both of these filter types serve to smooth an image by averaging the gray-scale values present in an image over a certain distance, and are often applied in imaging studies [82], [102]–[104]. One of the drawbacks to using smoothing filters is that they generally do not preserve edges (phase interfaces) from the original image. Smoothing filters do exist that aim to preserve these important features, including a non-linear diffusion filter and a shock filter [105]. In addition to the filters mentioned here, widely used image processing software such as *ImageJ* [106] and *Avizo* (Visualization Sciences Group, Burlington, MA) are continually expanding their libraries of techniques for image enhancement and artifact removal.

2.2.3 Segmentation

Quantitative analysis of a material sample, e.g. modeling and simulation, traditionally relies on each distinct material phase in a sample being represented by a distinct label. Image

segmentation is the process of labeling each voxel in an image according to its corresponding phase. For example, if a porous composite SOFC anode composed of Ni-YSZ were imaged via XNT, a segmentation procedure would be used to assign each voxel in the reconstructed 3-D image as either the Ni, YSZ, or pore phase (for instance by labeling them as 1's, 2's or 3's), in addition to labeling any additional phases that may be present. Numerous algorithms exist for image segmentation which are generally categorized by their working principles; these include global thresholding, locally-adaptive thresholding, and region growing methods [107].

Global thresholding segments an image by making use of the image's histogram to select ranges of voxel values that correspond to particular phases. Each of the voxels in the image is then assigned a value based on which gray-scale range contains it. This method has a number of drawbacks, most notably its sensitivity to noise and pixilation. The presence of noise in a reconstructed image can result in numerous mislabeled voxels when global thresholding is applied, especially when contrast differences between phases are small. In addition to the aforementioned smoothing filters, post-segmentation filters are often used to circumvent these issues. Two operations, erosion and dilation, are commonly used after global thresholding to correct for mislabeled voxels, especially when isolated voxels of a certain phase erroneously appear within broad regions of another.

Global thresholding methods also do not rigorously define the edges and interfaces in a reconstructed image. For cases where preserving edges and interfaces are important, region growing techniques such as watershed segmentation are often used [8], [100], [104], [108], [109]. This technique begins with conservatively thresholding a seed region of a phase,

whereupon the seed regions are artificially expanded until they contact interfaces and fill the entire volume with discrete labels [101]. The interfaces of an image may be found by edge-finding techniques such as gradient mapping. A sample application of watershed segmentation, taken from Ref. [110], is shown in Fig. 2.2. Here, four material phases, including a neodymium-nickelate mixed conducting phase and void space, along with two possible poisoning phases, were segmented with a watershed algorithm. The application of watershed segmentation here allowed the authors to see that one of the poisoning phases tended to form on the surface of the primary conducting phase, which can reduce the surface area available for reactions and lead to performance degradation.

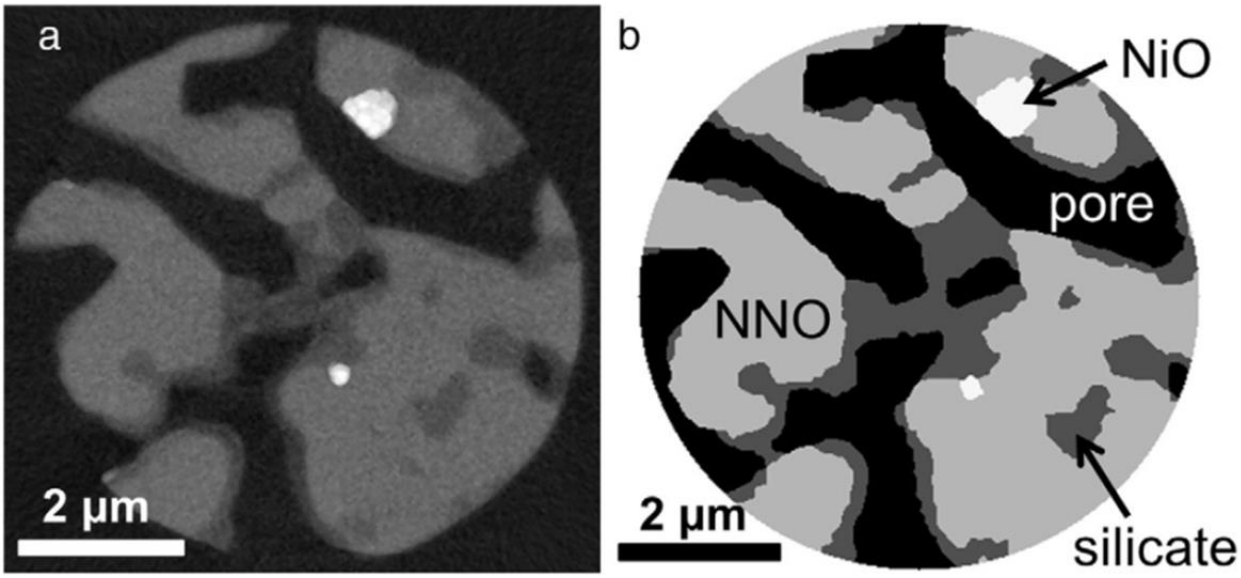

Figure 2.2. a) A cross-sectional view of Nd-nickelate SOFC cathode material obtained by XNT and reconstructed by FBP, and b) the image after watershed segmentation. This image is from Ref. [110].

While global thresholding and region growing techniques are often used, a large number of additional methods are available. Additional discussions of such segmentation techniques are provided in Refs. [105], [107].

Chapter 3*: Solid Oxide Fuel Cell Microstructure Conductivity Analysis

***Adapted from** [4]

3.1 Overview

As was discussed in Section 1.2.2, significant research has been dedicated to developing and utilizing transport models to aid in advanced SOFC electrode design. In an effort to overcome some of the limitations of existing models, the ECF theory described in Section 1.4.2 was developed, allowing complex structures to be represented by a network of axisymmetric charge conducting fins. Recently, Nelson et al. [102] have applied the ECF theory along with skeleton-based partitioning of a digitized sample volume into individual transport channels to study real mixed-conducting electrode materials, exhibiting that the model can compute experimentally validated polarization resistances and potential distributions that compare well to those found with a detailed finite element model. The advantages of using this new modeling tool were immediately evident; specifically, the ability of the theory to account for local microstructural effects such as specific transport channel morphology and network topology without reliance on averaged structural properties, as well as significantly reduced computational times compared to detailed finite element simulations.

However, as discussed by the authors, certain limitations of the algorithm used to construct the fin networks and the application of a non-dimensional form of the fin equation shown in Eq. 1.1 limited the potential accuracy of the approach. More recent developments by Cassenti et al. [87] have yielded closed-form solutions for charge transfer and surface reactions of electrochemical fins with well-defined radial profiles, including positive curvature spherical and negative curvature hyperbolic geometries. In this chapter, the electrode modeling tool of Ref. [102] is

expanded to include enhanced sensitivity to local transport channel morphology, via the application of the analytical solutions presented in Ref. [87], and is applied to the study of charge transport in a wide range of microstructures. Updates to the partitioning tool are described along with a corresponding algorithm to determine ideal fin shapes that best represent individual transport channels in the microstructural network. Extensive application and validation of the updated modeling tool is then presented for simple one-dimensional particle arrays, ideal packed sphere structures, and real microstructures including SOFC electrode samples imaged via XNT methods described in Chapter 2. Results from these charge transport analyses are compared to finite element simulations in Abaqus, as well as percolation theory, to showcase the model's applicability and merits as an electrode design tool.

3.2 Digital Microstructure Generation

3.2.1 Ideal Structures

The idealized structures presented here were all generated with in-house MATLAB codes. The first structures analyzed are simple 1D particle arrays, used to quantify differences in performance for the different particle types as well as approximate error that may be attributed to the simplifying assumption of one dimensional transport. These are generated by stacking spherical, conical, hyperbolic, or exponential fins in a single direction to create a chain of particles. A sample structure using spherical fins is shown in Fig. 3.1a. In order to quantify the effect that inter-particle neck size has for the different structures, a range of these arrays is created for different particle to neck radius ratios using each particle type.

For further assessment of the modeling approach, packed sphere structures with monosized particles are generated. These types of structures are commonly used for percolation studies and also as numerical domains for discrete modeling [18], [19], [22], [26], [27], [30]. Typically, packed sphere structures are generated by randomly depositing and repositioning spherical particles of different types into a volume, and then artificially sintering them together. One example algorithm used for this purpose is the drop-and-roll algorithm [25], [27]. A simpler method for creating structures is to use a pre-determined lattice to fix the locations of each particle in the domain [19]–[21]. Thus, the random nature of the structure is only achieved via random selection of a particle type before it is placed on a lattice point.

Since ideal structures are mainly used for validation of the modeling tool, a simple cubic lattice is chosen as the basis for the packed sphere structures. By nature of the simple cubic lattice, the average coordination number for all the structures generated is $Z = 6$, allowing quick comparison to common percolation studies [10], [111]. The structures are generated by iterating through a grid of lattice points and randomly selecting either an ionic or electronic conducting particle to place, thus simulating the microstructure of a composite SOFC electrode. In these simple structures, every particle is the same size and the volume fraction, contact angles, and volume size are decided by the user.

In this study, the ECF model is used only to analyze ion conduction through the ionic conducting phase. Thus, in the packed sphere structures, any deposited electronic conducting particles are treated as additional void space. This allows each of the voxels in the structures generated to be

represented by 1's for the solid ionic conducting phase, and 0's for the remainder of the volume. The volume fractions of each structure are then re-cast as a void fraction, i.e. a measure of the complement to the phase of interest, instead. For proper comparison to percolation theory, roughly 100 structures of varying void fractions are created. Two of these structures are shown in Fig. 3.1b and c, respectively. Keeping consistent with the theory of Costamagna et al. [10], contact angles are chosen as 15° between the spherical particles. The volume sizes are chosen large enough so as to be statistically representative, but also within a range that allows a detailed finite element comparison on the structures. A number of studies have been performed to discuss proper RVE size to accurately characterize electrode microstructures [30], [31], [112]–[114]. Cai et al. [30] found an electrode to particle size ratio of 7.5 yielded statistically representative volumes for packed sphere structures. Metcalfe et al. [114] and Laurencin et al. [31] both found that a ratio of 14 was sufficient for representative volumes. For the packed sphere structures in this paper, a ratio of 13 was chosen as it approximately meets these published requirements, but also allows for a dense mesh to be used for finite element studies. The particle diameter chosen for these structures is $d = 0.5\ \mu m$, resulting in cubic volumes with side length of $L_V = 6.5\ \mu m$.

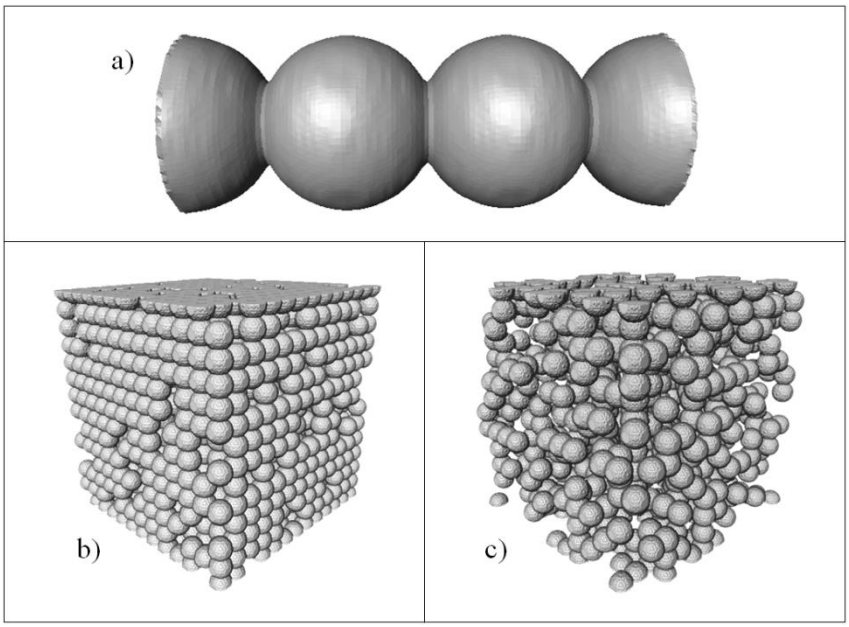

Figure 3.1. Artificially generated structures for model validation, including a) 1D array of spherical particles, b) low porosity ($\varepsilon = 0.46$) packed sphere structure, c) high porosity ($\varepsilon = 0.74$) packed sphere structure. This figure is from Ref. [4].

3.2.2 Real Structures via Synchrotron-Based X-ray Nanotomography

Because of the many simplifications associated with generating packed sphere structures on a simple cubic lattice, using the ECF modeling tool to analyze real electrode data with complex, amorphous transport networks gives necessary insight into the accuracy that can be obtained when capturing microstructural morphology and network topology. Since the goal of studying real structures is to provide us with a larger number of distinct transport networks than is possible via artificial structures, specific phase information aside from geometric configuration is not required. Thus, for any given sample of a composite electrode, for instance a Ni-YSZ (yttria-stabilized zirconia) SOFC anode or lanthanum strontium manganite - yttria-stabilized zirconia (LSM-YSZ) SOFC cathode, up to three connected networks are potentially available for

analysis; one of the electronic conducting phase, one ionic conducting phase, and a pore phase. Likewise, for a single phase mixed ionic–electronic conducting (MIEC) material, there are potentially two connected material networks to analyze, the solid phase and a pore phase. The modeling tool can be configured to assess theoretical ion transport through any of these microstructural networks, as long as separate digital volumes are created where the phase of interest is labeled as 1's, and the remainder of the volume is 0's. In this study, a wide range of SOFC electrode structures have been used including a composite GDC-CFO ceramic membrane containing a $Ce_{0.8}Gd_{0.2}O_2$ (GDC) oxygen ion conductive phase and a $CoFe_2O_4$ (CFO) electronic conductive phase [115], and composite Ni-YSZ anode material samples. Additional model validation is performed via modeling of a porous $Ce_{0.8}Sm_{0.2}O_{1.9}$ (SDC) gas separation membrane material [116], used to exemplify the model's applicability to other material systems. A full list of samples used and the corresponding RVE's extracted is shown in Table 3.1.

To obtain the real electrode samples studied in this work, a series of XNT imaging experiments have been performed according to the steps outlined in Chapter 2. For each of the samples studied, an initial cylinder was extracted from each of the samples using an FEI Strata focused ion beam-scanning electron microscope. These cylinders are on average 8-10 μm in diameter and 15-20 μm in height. The samples were then imaged via transmission X-ray microscope at either the Stanford Synchrotron Radiation Lightsource, beamline 6-2c or the National Synchrotron Light Source, beamline X8C. X-ray nanotomography was performed, yielding a range of transmission images for each sample which were then reconstructed via filtered back projection to produce a three dimensional grayscale data set. Image filtering steps such as median filtering for noise reduction were taken, whereupon watershed segmentation was used to

discretely label individual material phases. From the resulting segmented three-dimensional image stacks, a number of RVEs were then extracted using ImageJ software, whereupon each phase of interest may be isolated in separate digital volumes. The sizes of the RVEs and the phase of interest are also detailed in Table 3.1, along with the voxel size of the samples. RVE sizes for real structures are limited in this study to allow proper detailed comparisons to finite element analyses, inclusive of capturing nano-scale morphological features without reaching memory limitations of a Dell OptiPlex 980 desktop computer with 16 GB RAM.

Sample	RVE Number	Phase of Interest	Cube Side Length (voxels)	Voxel Size (nm)	Void Fraction
GDC-CFO [115]	1	GDC	220	28.5	0.517
GDC-CFO [115]	1	CFO	220	28.5	0.584
GDC-CFO [115]	2	GDC	220	28.5	0.485
GDC-CFO [115]	2	CFO	220	28.5	0.621
GDC-CFO [115]	3	GDC	185	38.9	0.564
GDC-CFO [115]	3	CFO	185	38.9	0.562
GDC-CFO [115]	4	GDC	185	38.9	0.573
GDC-CFO [115]	4	CFO	185	38.9	0.551
SDC50 [116]	1	Pore	220	19.5	0.422
SDC50 [116]	1	SDC	220	19.5	0.578
SDC50 [116]	2	Pore	220	19.5	0.435
SDC50 [116]	2	SDC	220	19.5	0.565
SDC50 [116]	3	Pore	220	19.5	0.422
SDC50 [116]	3	SDC	220	19.5	0.578
Ni-YSZ	1	Ni	200	38.9	0.632
Ni-YSZ [117]	1	Ni	220	19.5	0.744
Ni-YSZ [117]	1	Pore	220	19.5	0.775
LSM [118]	1	Pore	240	19	0.688
SDC40 [116]	1	SDC	200	25	0.397

Table 3.1. Real material microstructures used for this study, including SOFC electrode samples (GDC-CFO, Ni-YSZ, LSM) and a gas separation membrane material (SDC). This table is from Ref. [4].

3.3 Charge Transport Modeling

3.3.1 Electrochemical Fin Model

The ECF model introduced in Section 1.4.2 and utilized in Ref. [102] is expanded in this work to more effectively account for local microstructural effects, by applying the analytical solutions developed in Ref. [87] for various fin shapes. These analytical solutions are described briefly in Section 3.3.1.1, below, followed by descriptions of the updated partitioning tool and methodology used to apply the ECF model to three-dimensional structures. A measure of effective ionic conductivity is used to assess charge transport in the absence of electrochemical reactions for the various structures described in Section 3.2, and compared to predictions from other commonly used models for validation.

3.3.1.1 Closed-Form Solutions for Axisymmetric Fins

To facilitate studying advanced electrode microstructures, Cassenti et al. [87] provided analytical solutions for three axisymmetric fin geometries: a neutral curvature conical frustum, a positive curvature spherical segment, and a negative curvature hyperbolic segment. Additionally, a fourth geometry is considered in this work, that of a fin with a negative curvature smooth exponential profile that results from the application of two dimensionless parameters describing a fin's morphology: sintering quality and resistivity ratio [102]. In Ref. [102], this exponential profile was used exclusively to define every fin in their resulting electrochemical fin resistor networks. For general comparison, the neutral curvature, positive curvature, and negative curvature fin types are shown in Fig. 3.2a, b and c, respectively. For definitions of charge transport and geometric properties for each of the fins, the reader is referred to Fig. 1.3.

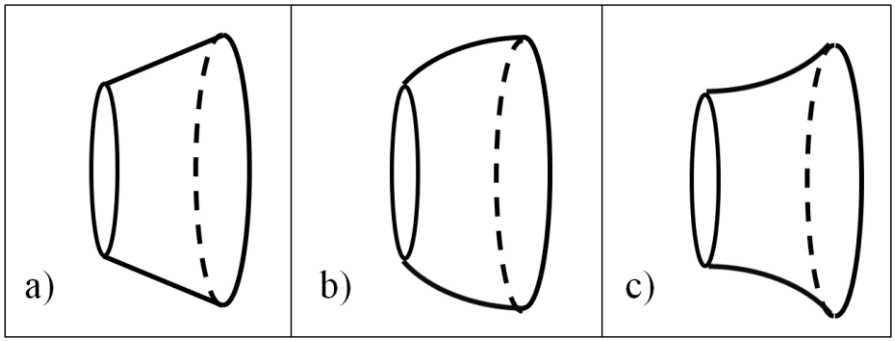

Figure 3.2. Electrochemical fins with a) neutral curvature (conical) profile, b) positive curvature (spherical) profile, and c) negative curvature (hyperbolic or exponential) profile. This figure is from Ref. [4].

The radius for the conical fin geometry takes the form

$$a = kz + z_0 \tag{3.1}$$

The general solution for its variation in potential is then found as

$$\varphi = A_1 I_1\left(2\sqrt{\frac{2\left(1+k^2\right)}{\sigma R k}\left(kz+z_0\right)}\right) + A_2 K_1\left(2\sqrt{\frac{2\left(1+k^2\right)}{\sigma R k}\left(kz+z_0\right)}\right) \tag{3.2}$$

Here, I_1 and K_1 are modified Bessel functions of the first and second kind, and constants A_1 and A_2 can be found by imposing boundary conditions at the endpoints of the fin. The spherical segment has a radius governed by

$$a^2 + \left(z - z_0\right)^2 = \frac{1}{k^2} \tag{3.3}$$

The solution is

$$\varphi = A_1 P_{\nu(1)}\left(k\left(z - z_0\right)\right) + A_2 P_{\nu(2)}\left(k\left(z - z_0\right)\right) \tag{3.4}$$

Here, $\nu(1,2) = -1/2 \pm \sqrt{(1/2)^2 + (2/\sigma Rk)}$ and constants A_1 and A_2 are determined via boundary conditions. The negative curvature hyperbolic fin has a radius given by

$$a(z) = \frac{1}{k}\cosh\left(k\left(z - z_0\right)\right) \tag{3.5}$$

The resulting governing equation can be solved by setting

$$\varphi = \frac{\Phi}{a(z)} \tag{3.6}$$

This yields as a solution

$$\Phi = A_1 e^{\alpha k\left(z - z_0\right)} + A_2 e^{-\alpha k\left(z - z_0\right)} \tag{3.7}$$

Here, $\alpha = \sqrt{1 + 2/\sigma Rk}$ and A_1 and A_2 are constants determined by the boundary conditions. The fourth geometry is determined by casting Eq. 1.1 in terms of dimensionless parameters $z^* = z/L$, $\varphi^* = \varphi/\varphi_b$, $A_c^* = A_c/A_{c,b}$, and $A_s^* = A_s/A_{c,b}$. Noting that cross-sectional area is defined as

$$A_c(z) = \pi a^2(z) \tag{3.8}$$

And surface area is obtained by integrating

$$dA_s(z) = 2\pi a(z)\sqrt{1 + \left(\frac{da}{dz}\right)^2}\, dz \tag{3.9}$$

Eq. 1.1 can now be rewritten as

$$\frac{d^2\varphi^*}{dz^{*2}} + \frac{1}{A_c^*}\frac{dA_c^*}{dz^*}\frac{d\varphi^*}{dz^*} - \frac{L}{\sigma R A_c^*}\frac{dA_s^*}{dz^*}\varphi^* = 0 \tag{3.10}$$

From this equation, two dimensionless parameters can be extracted. The first, sintering quality SQ as defined in Eq. 3.11, describes the variation in the cross-sectional area of a fin. The second, a resistivity ratio defined in Eq. 3.12, describes the ratio of charge transfer resistance to conduction resistance within the fin [102].

$$SQ = \left[\frac{L}{A_c}\frac{dA_c}{dz}\right]^{-1} \tag{3.11}$$

$$\frac{\rho_{io}}{\rho_{ct}} = \frac{L^2}{\sigma R}\frac{1}{A_c}\frac{dA_s}{dz} \tag{3.12}$$

Fixing the sintering quality as a constant and integrating Eq. 3.11 for a single segment yields

$$SQ = \left[\ln\frac{A_2}{A_1}\right]^{-1} \tag{3.13}$$

The radius profile corresponding to this fixed sintering quality is

$$a = a_0 e^{\frac{1}{SQ}\frac{z}{2L}} \tag{3.14}$$

Nelson et al. [102] have also fixed the resistivity ratio as a constant for application to real electrode materials. Plugging Eq. 3.14 into Eq. 3.12, we see that the resistivity ratio cannot be constant. Thus, assuming a fixed value for the resistivity ratio, approximated by Eq. 3.15, results in an error in approximating Eq. 3.12 which was determined to be acceptable for particles with

only moderate changes in radius [102]. The resulting solution for the dimensionless potential distribution, assuming fixed sintering quality and resistivity ratio, is shown in Eq. 3.16.

$$\frac{\rho_{io}}{\rho_{ct}} \approx \frac{L^2}{\sigma R}\frac{A_s}{V} \tag{3.15}$$

$$\varphi^*\left(z^*\right) = A_1 e^{\alpha_1 z^*} + A_2 e^{\alpha_2 z^*} \tag{3.16}$$

Where $\alpha_{1,2} = \frac{1}{2}\left[-\frac{1}{SQ} \pm \sqrt{\frac{1}{SQ^2} + 4\left(\frac{\rho_{io}}{\rho_{ct}}\right)}\right]$ and A_1 and A_2 are arbitrary constants.

It is noted here that if no surface reactions are present, the resistivity ratio becomes zero and the third term of Eq. 3.10 drops out, thus the solution defined by Eq. 3.16 is an exact solution for the exponential fin profile of Eq. 3.14. If surface reactions are present, the error described in Ref. [102] in assuming a constant resistivity ratio would exist.

The solutions for the different fin geometries, shown by Eqs. 3.2, 3.4, 3.7, and 3.16, can be combined to yield a composite solution for networks of electrochemical fins. This approach, which is comparable to common resistor network approaches in the literature, follows Kirchhoff's circuit laws and requires the continuity of current at each node in the structure. Thus, the potential at each node can then be determined given the network connectivity data, material properties σ and R, and the geometry for each fin. The required inputs for each fin geometry are geometry type, fin length, curvature or slope, and axial offset; for the exponential segments, the fin length, surface area to volume ratio, and base and tip areas must be specified.

3.3.1.2 Network Partitioning Tool – A Unique Discretization Approach

The goal of the ECF modeling tool is to approximate real or ideal microstructures as networks of electrochemical fins in order to compute performance characteristics of the original structure. As was mentioned above, each fin in the equivalent network must have a defined geometry, material properties, and network connectivity data. To extract this information, an edge-based partitioning tool was developed in MATLAB, with calls to Avizo skeletonization, watershed, and meshing functions [102]. The basic goal of the partitioning tool is to discretize three-dimensional microstructures into a series of conduction channels, requiring each channel to have an entrance area and an exit area available for bulk charge transport along with an external surface available for electrochemical reactions. The tool is then used to compute necessary parameters for each partitioned segment, allowing an equivalent fin network to be constructed. Details about the basic process, including skeletonization and labeling procedures, are discussed in Ref. [102]. However, it has been noted by the authors that the previously implemented partitioning approach is limited in its ability to capture and model local transport channel morphology.

One goal of this study is to enhance the partitioning tool to facilitate more accurate modeling of the microstructure inclusive of morphological and topological effects, which requires additional steps in the partitioning process. Two partitioning methods are presented in this work and shown schematically in Fig. 3.3; the first being the previously implemented approach and the second includes updates necessary for more accurate capturing of structure morphology. To aid in a description of these approaches, a consistent verbiage must be adopted. In the following discussion, the skeleton computed for any given microstructure is composed of ‘edges’, or

skeleton branches, and ‘nodes’, or vertices. The skeleton information is used to partition the original microstructure into distinctly labeled ‘segments’, which are essentially three dimensional conduction channels. Each ‘segment’ contains a skeleton ‘edge’ as a foundation that dictates the primary transport axis, along with two ‘nodes’ that define the boundaries of the segment and correspond to end areas available for bulk transport. Relevant parameters including length, volume, and inter and intra-phase interfacial surface area are then extracted for each ‘segment’, which are then used to construct corresponding axisymmetric electrochemical ‘fins’. Noting network connectivity obtained from the skeleton information, these ‘fins’ are then combined to form a resistor network representing the original microstructure.

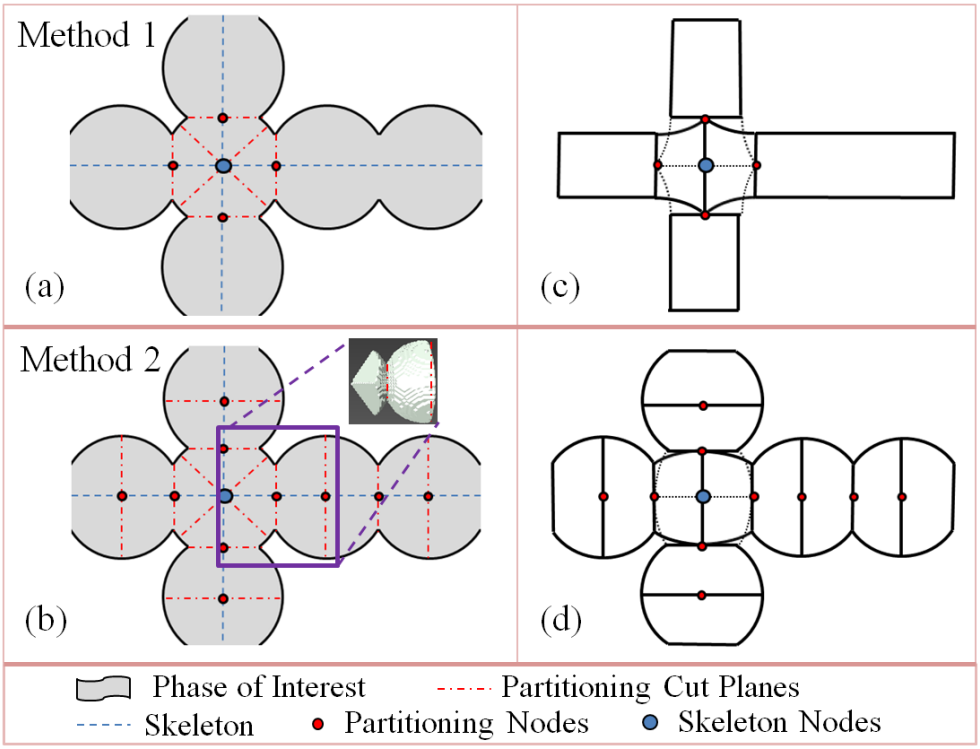

Figure 3.3. Two partitioning methods are shown that can be used to discretize three-dimensional microstructures into charge transport channels. Method 1 (a) uses the skeleton as a basis to partition a structure into segments, and then uses exponential electrochemical fins to build an

equivalent fin network (c). Method 2 (b) automatically sub-partitions the microstructure at local minima and maxima and allows fin shapes to be chosen to best represent the actual microstructure (d). This figure is from Ref. [4].

Partitioning method 1, as shown in Fig. 3.3a and c, was previously utilized in Ref. [102]. As seen in the figure, microstructural networks are partitioned according to skeleton information obtained from Avizo, with certain constraints. Each edge of the skeleton initially corresponds to one resistive component in the equivalent fin network. Edges with a local minimum, or a 'neck', are cut at the neck in order to capture the constrictions and are then represented by two resistive components. This additional cutting process is referred to as sub-partitioning. In this original partitioning approach, sub-partitioning is only performed once per segment, at the intersection between watershed lines in vertex-based partitioning and the skeleton edge point. Thus for edges with multiple constrictions or bulges, such as that shown in Fig. 3.3a, some features remain unaccounted for. Each resulting segment after sub-partitioning is then measured for its end areas, length, and surface area to volume ratio. Edge-based partitioning produces non-flat surfaces (the diamond-shaped regions of a segment depicted in Fig.3.3). When equating this area to the flat circular end area of an axisymmetric fin used to represent the segment, the true cross-sectional area available for conduction would be severely overestimated in most cases. Instead, a projection end area is calculated by counting material contacting a plane projected normal to the skeleton edge at both ends of a segment. Thus, the end area computed is approximated as a flat area, enabling more accurate geometric representation in the equivalent fin network. Segment length is calculated as the length of the smoothed skeleton, and volume is simply measured as the amount of material composing each segment. These computed

geometric parameters are then used to compute the non-dimensional parameters sintering quality and resistivity ratio, which allows each segment to be approximated with a fin whose radius varies according to Eq. 3.14, as shown schematically in Fig. 3.3c. The benefits to this approach are that limited sub-partitioning is used, and the non-dimensional approximation requires only basic geometric information. However, this method does not capture all major necks and bulges in a given microstructure especially for longer segments due to limited sub-partitioning, and representing a structure's transport channels as only exponentially varying fins can lead to inaccurate representations of the microstructure in the resulting electrochemical fin network. A visual example of these potential issues is shown in Fig. 3.3c.

Partitioning method 2, shown in Fig. 3.3b and d, aims to improve the accuracy of the ECF model by implementation of additional, automatic sub-partitioning steps and application of the analytical solutions presented in section 3.3.1.1. The additional sub-partitioning steps are activated and controlled by user-specified minimum and maximum allowable edge lengths. Any edges that are longer than the maximum value specified are subjected to sub-partitioning at remaining local minima or maxima in the corresponding segment, according to the value of the phase distance map at the skeleton points. The minimum edge length is present to ensure segments are not too thin to extract useful information from them (due to limited voxel resolution), which combined with the maximum length results in segments entirely within the specified range of lengths. As shown in Fig. 3.3d, this can result in more accurate capturing of inter-particle necks and constrictions within microstructural networks. The length, external surface area and volume are computed as described in the original approach. However, in order to properly define external surface area available for reactions, each segment's interface area is

classified according to amount contacting void space versus amount contacting material of the same phase. Thus, charge transfer resistance for each equivalent fin in the network can be adjusted based on area available for reactions. In this study, electrochemical reactions are neglected, so this effect is not quantified; however this is seen as an issue for future investigation. The geometric parameters extracted here can then be used as a basis for the shape fitting algorithm outlined in Section 3.3.1.3.

3.3.1.3 Transport Channel Analysis and Fin Shape-Fitting Approach

The information extracted from the partitioning tool must now be used to construct an electrochemical fin network representing the microstructure. Thus, each segment must correspond to an idealized axisymmetric fin shape which best approximates the conductive properties of the segment and its surface electrochemistry. As mentioned previously, each fin requires network connectivity information, material properties, and a defined geometry. The network connectivity information is first determined from the skeleton produced by Avizo. Each partitioned segment, including those produced via sub-partitioning steps, has a corresponding skeleton edge label and two skeleton nodes which determine its boundaries. Segments with shared nodes maintain a physical connection in the microstructure, and thus will connect in the fin network. Material properties σ and R are defined by the user and are set for each fin in the network. The exception to this would be segments with modified values of charge transfer resistance R to account for amount of exposed surface area. Lastly, each fin requires a defined length L, curvature or slope k, axial offset z_0, and geometry type, as discussed in Section 3.3.1.1. These parameters must then be derived from known geometric quantities extracted from each segment in the microstructure. Based on the partitioning approaches outlined above, the end

areas A_1 and A_2, length L, surface area A_s, and volume V can all be measured for each segment. Due to the amorphous nature of real microstructures, it is not plausible to determine an axisymmetric curvature or slope directly from the labelled segments.

In order to avoid material discontinuities, end areas computed from the real structure must remain consistent with the equivalent fin network. Similarly, to avoid adding or removing a significant amount of material, length is also to remain consistent. Making the assumption that the end areas are flat and circular, initial radius a_1 and final radius a_2 of the corresponding fin can be determined by $a_1 = \sqrt{A_1/\pi}$ and $a_2 = \sqrt{A_2/\pi}$. Therefore a_1, a_2 and L are known for each fin based on simple geometric measurements. Given any combination of a_1, a_2, and L, the fin geometries described in Section 3.3.1.1 can be defined within certain constraints.

Conical fins, whose profile is defined in Eq. 3.1, can be formed given any combination of the three parameters. The length of a conical fin is simply equated to segment length, and the slope k and offset z_0 are defined, respectively, as

$$k = \frac{a_2 - a_1}{L} \tag{3.17}$$

And

$$z_0 = a_1 \tag{3.18}$$

Spherical fins, as defined in Eq. 3.3, can also be defined given any combination of end radii and length. The curvature k for a spherical fin can be determined by

$$k = \frac{1}{a_1\sqrt{1+\left(\frac{L^2 - a_1^2 + a_2^2}{2La_1}\right)^2}} \tag{3.19}$$

While the offset z_0 is computed as

$$z_0 = \frac{L^2 - a_1^2 + a_2^2}{2L} \tag{3.20}$$

Given any combination of a_1 and a_2, there are a range of fin lengths, defined by $0 < L \leq \sqrt{\left|a_1^2 - a_2^2\right|}$, where the resulting spherical fin's radial profile is either monotonically increasing or decreasing. However, when $L > \sqrt{\left|a_1^2 - a_2^2\right|}$ the resulting spherical fins bulge out to accompany the extra length and the radius is no longer a monotonic function. Thus, if the lengths of spherical fins are not properly controlled via the maximum length constraint, they may form undesired bulges and over-estimate the radial dimensions of the corresponding transport channel in a real structure.

The hyperbolic radius profile defined by Eq. 3.5 forms a negative curvature fin and has an analytical solution for its potential, shown in Eq. 3.7 [87]. However, given a fin's end radii and length, a corresponding hyperbolic geometry and relevant parameters cannot be found analytically and instead a numerical or graphical approach must be used to determine k and z_0. Due to the significant computational time and manual intervention this would require, exponential fins are instead adapted as the negative curvature fin geometry.

For the case of an exponential fin, the approach described in Ref. [102] is used. This requires calculation of sintering quality and resistivity ratio from Eqs. 3.13 and 3.15, respectively. As mentioned previously, surface reactions are neglected in this work, so approximating the resistivity ratio with a fixed value is not required and an exact analytical solution for the exponential geometry exists.

If there is sufficient knowledge of a particular microstructure beforehand, i.e. in the case of ideal structures composed of well-defined particle shapes, then the relations presented are sufficient to define the necessary fin geometries. However, complex ideal structures and real amorphous microstructures require defining axisymmetric fin shapes to best represent charge transport within the partitioned transport channels. Therefore, an algorithm must be implemented to automatically determine the best fin shape to represent the morphology of each segment. Noting that the end radii and the length have all been fixed for the ideal fin, any given initial radius, final radius, and length combination will correspond to only one spherical geometry, one conical geometry, and one exponential geometry. Due to the requirement of axisymmetric fins, and the amorphous nature of segments extracted from real structures, exact fits are not expected. Instead, a general measure of each segment's shape is used as the basis for choosing between the three geometries. For this purpose, the surface area to volume ratio extracted from each segment is used. With the surface area to volume ratio known for each real partitioned segment, and only three distinct geometries that can be chosen from, a direct numerical comparison can be made between the surface area to volume ratio of the real segment and that of the three possible fin options. The fin shape whose surface area to volume ratio is closest to that of the real segment is then chosen. This criterion for fin selection can be modified as desired. Once this step has been

performed and fin geometries are chosen to best represent each segment, a complete electrochemical fin network may be constructed.

3.3.1.4 Calculating Effective Conductivity

While previous applications of the ECF modeling approach have focused on determining polarization resistance for different structures, the present work computes effective conductivity as the primary indicator of microstructural performance in an effort to focus on accurately capturing the effects of microstructure morphology on charge conduction. For each structure under consideration, two opposing boundaries are chosen and a fixed potential is applied at each boundary. The potential at each node in the structure is then solved and the resultant total current i_{tot} can be calculated as the sum of currents entering each node contacting one of the boundary faces where a fixed potential was applied. The effective conductivity of the structure is determined by

$$\sigma_{eff} = \frac{i_{tot} L_V}{A_{c,V} \Delta\varphi_V} \tag{3.21}$$

The effective conductivity can then be normalized by the intrinsic material conductivity to yield more general results, as shown in Eq. 3.22.

$$\bar{\sigma}_{eff} = \frac{\sigma_{eff}}{\sigma} \tag{3.22}$$

3.3.2 Finite Element Model

Two different types of finite element models are used to compare to the ECF modeling tool conductivity predictions. The Heat Transfer module of Abaqus/CAE 6.9 is used for both of these models, based on its equivalence to the ECF model (i.e. solution of the steady-state heat equation).

The first is an axisymmetric two dimensional model used for comparison with ECF solutions of one dimensional arrays of particles. Within Abaqus, geometries representing the axisymmetric fins were drawn in a two dimensional plane, and the resulting part was meshed using quadratic heat transfer mesh elements allowing accurate characterization of curvature and relevant features. Sample meshes are shown in Fig. 3.4c and d. The material conductivity was defined and boundary conditions were imposed at the end surfaces of the array, corresponding to $z = 0$ and $z = L$. The two sets of boundary conditions applied were a Dirichlet/Neumann combination for computing local potentials along the array and a Dirichlet/Dirichlet combination for computing effective conductivities. Since we are only interested in the conduction problem, no surface flux was imposed for the structures in either case. The application of an axisymmetric two dimensional model to analyze detailed geometry is similar to that performed in Ref. [85], except in this case no space charge regions were modeled and surface flux is removed.

The second finite element model developed for validation was used to solve for transport within three dimensional structures. The inputs for these cases were binary tiff stacks of the phase of interest for either the real or artificial microstructures. In order to generate a mesh, Avizo 7

Standard was used. The tiff images were imported into Avizo whereupon the surface was smoothed and Avizo's Surface Simplification Editor was run. Surface triangulation was controlled so as to capture all relevant features of the structure, including inter-particle necks and small pores. A tetrahedral mesh grid was then generated and imported into Abaqus. The number of mesh elements used to represent the structure is typically dependent on volume size, volume fractions, and feature sizes for each RVE analyzed. In the present work, the number of tetrahedral mesh elements used ranged from 1 million to 5 million, depending on these factors. A sample mesh for a GDC-CFO structure can be seen in Fig. 3.6b. Once in Abaqus, quadratic heat transfer mesh elements were chosen for the structures. Intrinsic conductivity was set, and fixed Dirichlet boundary conditions were applied at two opposing faces of the structure, corresponding to $z = 0$ and $z = L_V$. Transport through the structure was then solved without surface flux. Results could then be viewed, including local fluxes and nodal temperatures (i.e. potentials). The fluxes across the boundaries at $z = 0$ and $z = L_V$ were compared as a verification step and then used to compute effective conductivities via Eq. 3.21. It is important to note that in both finite element models used, steady state temperature distributions are equivalent to electrostatic potential fields and may be directly compared to potential distributions computed by the ECF model.

3.3.3 Percolation Theory

The percolation theory model used to predict effective ionic conductivity was that of Costamagna et al. [10]. The equation used is shown in Eq. 3.23.

$$\sigma_{eff} = \frac{\gamma\sigma(n - n_c)^{\mu}}{(1 - n_c)^{\mu}} \tag{3.23}$$

Here, σ is the intrinsic material conductivity, μ is a universal exponent that is 2.0 in three dimensions, n is the number fraction of the ionic conducting particles, n_c is the percolation threshold, and γ is a fitting parameter of the model taking into account neck size. In order to compare this model to data from ECF theory analysis of the packed sphere structures, n was first computed for each structure by dividing the total number of ionic conducting particles placed by the total number of lattice sites available. This value was then correlated to values of void fraction ε for plotting, based on the packing density of a fully packed structure, which for this study was 0.63. Next, the percolation threshold n_c was set to $n_c = 0.3116$, which has been determined as the site percolation threshold for simple cubic lattices by a number of authors [119], [120]. Lastly, since the contact angle for the packed sphere structures studied was set universally to 15°, we chose $\gamma = 0.5$. Costamagna et al. have reported using this value of γ for structures with a contact angle of 15°. Based on these values, no fitting parameters were used to compare Eq. 3.23 to data obtained via the ECF model.

3.4 Results and Discussion

3.4.1 Transport in Simple Particle Arrays

For each of the four geometry types introduced in Section 3.3.1.1, a range of simple particle arrays was created with varying particle to neck radius ratios. In each array, the largest radii were set to 0.5 μm and the smaller radii were varied accordingly. These arrays were used as inputs in a Microsoft Excel version of the ECF code. For each array, fixed potentials were applied at the inlet and exit, allowing resulting current through the structure to be calculated.

These currents were used to compute normalized effective conductivities for the structures according to Eq. 3.21.

Figure 3.4a shows the resulting conductivities plotted as a function of particle type and radius ratio. When $a_p/a_n > 1$, arrays composed of spherical fins yield the highest conductivities, while arrays of hyperbolic fins have the lowest. Conical and exponential fins produce intermediate results. This effect can be attributed to the average cross-section area available for bulk transport within the constituent fins. An interesting result from this study is the fact that very high radius ratios result in normalized effective conductivities approaching 0 for conical, exponential, and hyperbolic fins, while conductivities for spherical fin arrays decrease at a much slower rate. It is theorized this effect is due mainly to the assumption of one dimensional transport and cross-sectional averaging of the potential in an array.

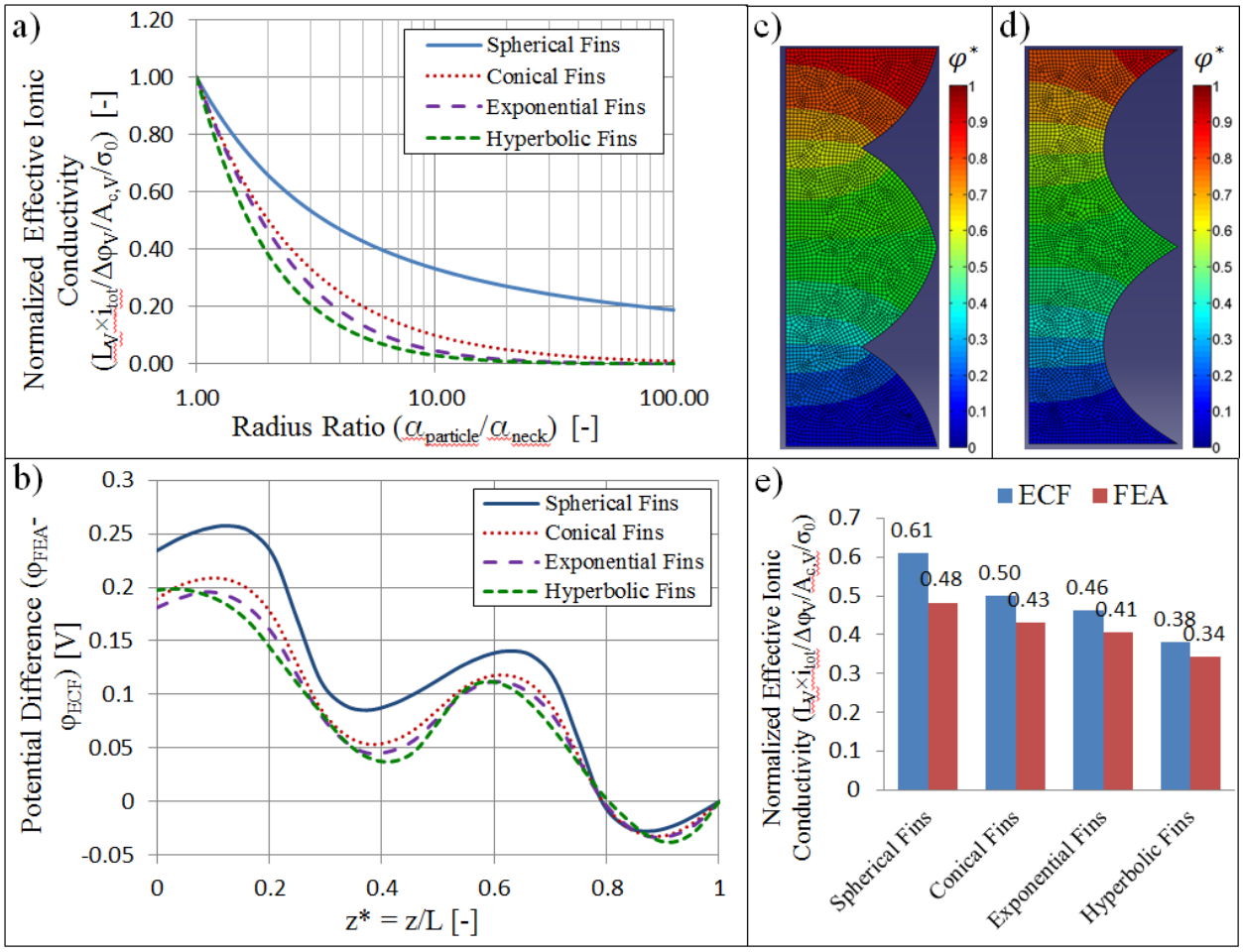

Figure 3.4. a) Normalized effective conductivities of simple arrays composed of different particle types for a range of radius ratios, b) potential difference distributions between electrochemical fin and finite element analysis results for transport through spherical, conical, exponential, and hyperbolic particle arrays, axisymmetric lines of equipotential for arrays composed of c) spherical and d) hyperbolic segments, and e) effective conductivity of one-dimensional particle arrays composed of spherical, conical, exponential, and hyperbolic fins using electrochemical fin (ECF) and finite element analysis (FEA). This figure is from Ref. [4].

To test the effect of the one dimensional transport assumption, arrays with a fixed radius ratio of $a_p/a_n = 2$ were chosen using each fin type. These structures were analyzed using both ECF

theory and Abaqus FEA. The boundary conditions used were a fixed Neumann condition at the array inlet and a fixed Dirichlet condition at the exit. In both cases, a potential distribution was determined throughout the array. In the ECF model, potentials were found at each of the nodes of the structure, and in Abaqus, bulk temperature was computed along the length of the axisymmetric model. This bulk temperature could then be compared directly to the cross-section averaged potentials computed via ECF theory. The difference in potential between the two analyses along the array length is shown in Fig. 3.4b.

It is clear from this figure that the ECF model generally over-predicts conduction through segments, regardless of particle shape. In other words, the assumption of one dimensional transport causes the model to under-estimate the resistance for any given array of particles. Interestingly, the peaks and valleys in Fig. 3.4b do not appear to line up for the different geometry types. Noting the spherical array potential distribution shown in Fig. 3.4c and the hyperbolic distribution of Fig. 3.4d, it appears that the locations where radial current flow is most prominent, i.e. near the spherical necks and near the hyperbolic bulges, correspond to the peaks of greatest error in Fig. 3.4b. These are regions where there is slope discontinuity between particles, and therefore is where the cross-sectional averaging assumption in the ECF method deviates most from the finite element solution. For the case of a spherical particle, the greatest instantaneous change in slope occurs at the neck between adjacent particles, or at the constrictions. Alternatively, the greatest change in slope for hyperbolic particles occurs at the particle bulges. Since constrictions will have a greater impact on particle resistance than bulges, spherical particles generate the greatest difference between the ECF and FEA results; hyperbolic particles have the least error on average, and the other two particle types are intermediate.

The effect that these predictions have on effective conductivity is quantified and shown in Fig. 3.4e, for the case of $a_p/a_n = 2$. Both the ECF and FEA models predict the highest conductivities for spherical particle arrays, followed by conical, exponential, and hyperbolic arrays which maintain the lowest conductivities. However, the performance over-prediction by the ECF model is clearly visible and is most prominent for spherical particles. For smaller radius ratios, this effect is predicted to be not as severe; however it may be exacerbated for arrays with more narrow constrictions.

3.4.2 Conductivity of Ideal Packed Sphere Structures

Fourteen packed sphere structures with varying void fraction were created to analyze the effect that ECF geometry selection has on performance predictions with respect to FEA results. For each case, particle diameter was set to $0.5\ \mu m$, and the overall dimensions of the volume were $6.5x6.5x6.5\ \mu m^3$, represented by $236x236x236\ voxels^3$. The boundary conditions imposed were a fixed potential of $1\ V$ at the top face of each volume and a fixed potential of $0.5\ V$ at the bottom face. Normalized effective conductivities were computed by both the MATLAB version of the ECF code and a FE model in Abaqus.

The partitioning method employed for these structures was method 2, enabling all inter-particle necks to be captured by the partitioning algorithm. Since the structures are idealized structures composed of a single particle type, geometry selection is reduced to choosing a single geometry type for every fin in the resulting ECF network. Based on the results of Fig. 3.4a, a range of effective conductivities is expected depending on which geometry type is chosen.

The normalized effective conductivities found using a single geometry type for each fin in the ECF networks, as well as FEA results, are plotted in Fig. 3.5a. Using spherical fins in the ECF network, the results from the ECF model compare well to those of the FE model, especially considering the fact that the ECF model will consistently over-predict effective conductivity with respect to a more detailed FEA on the same geometry. It is noted that using either conical or exponential fins to represent each resistor in the network would result in under-predicting performance. This showcases the importance of choosing the correct fin geometry to represent the actual segments of an artificial microstructure. Ignoring the effects of geometry, it appears that network topology information is also captured well with the ECF model. In general, the trend of decreasing conductivity with increasing void fraction as shown by the FEA data is found accurately with the ECF approach, and corresponds to the effect of fewer, more tortuous conduction paths being present as void fraction is increased.

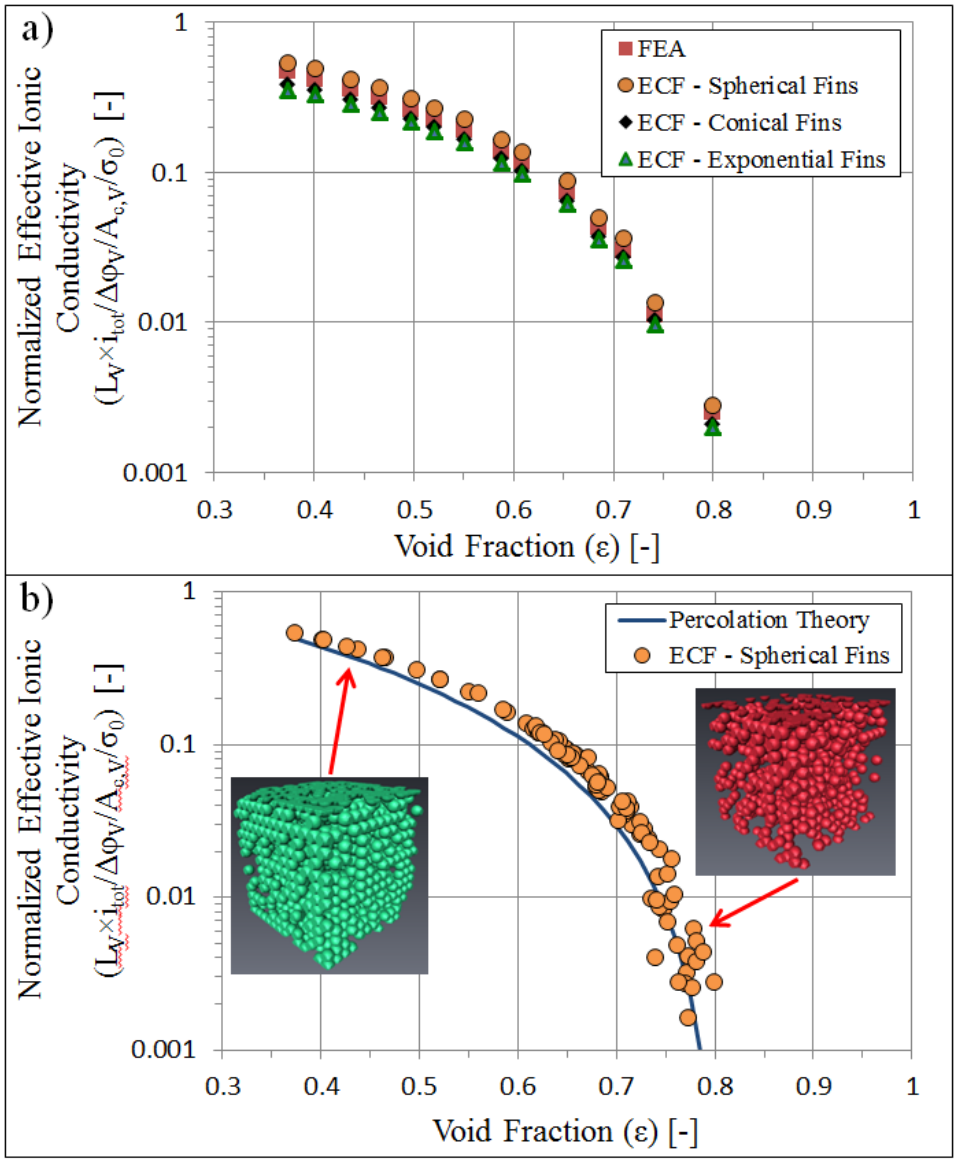

Figure 3.5. a) Normalized effective conductivities computed by finite element analysis (FEA) and the electrochemical fin (ECF) theory for a range of packed sphere structures. Electrochemical fins in the ECF resistor network can be represented by spherical, conical, or exponential fins. b) Normalized effective conductivity of a range of structures as computed by electrochemical fin (ECF) theory and compared to predictions of percolation theory [10]. Inset images are examples of packed sphere structures analyzed. This figure is from Ref. [4].

Regarding computational costs, it has been noted that time and memory required to resolve an electrochemical fin network scales with the number of fins resulting from the edge-based partitioning step. Due to the increased number of sub-partitioning steps partitioning method 2 requires compared to method 1, the number of fins in the equivalent ECF network is increased, thus computational costs are steeper than previous implementations of the model. Using partitioning method 2, the packed sphere structures analyzed yielded resistor networks ranging from 212 fins, for the highest void fraction case, to 13,130 fins for the fully packed case. The solution times for these volumes were 0.24 seconds and 77.87 seconds, respectively; RAM required for the calculations was 0.99 GB and 3.93 GB, respectively. As noted by Nelson et al. [102], computational requirements for the finite element simulations are dependent on the number of mesh elements used to represent a structure. Thus, the improvements in both time and memory required by the ECF model over the FE model are in part due to fewer building block elements required to represent a given microstructure. In the present simulations, each spherical particle was represented by anywhere from 2-6 fins, resulting from the particle's coordination number; however, no strict relation is imposed between coordination number and number of fins used to represent a particle. Regardless of coordination number, each spherical particle would require on the order of hundreds of mesh elements for accurate FE mesh generation. The result is that on average, time required to complete a finite element simulation, excluding the mesh generation step, was roughly 2.5 orders of magnitude greater than the ECF model solution step. Likewise, approximately 10 times the amount of RAM in GB was required to complete the FE analyses on average.

For comparisons with percolation theory, roughly 100 structures were created and analyzed using the ECF model. In these cases, spherical fins were used exclusively to represent segments in the structure. The resulting normalized effective conductivities of the structures are shown in Fig. 3.5b in comparison with predictions of Costamagna's percolation theory. In general, percolation theory does a good job of predicting the trend of decreasing effective conductivity with increasing void fraction. These predictions are especially accurate far away from the percolation threshold of the structures. However, within roughly 10% of the percolation threshold, i.e. when $\varepsilon > 0.7$, percolation theory predictions begin to differ from ECF model results by up to one order of magnitude. In addition to the data points shown, roughly 22% of the structures created with a void fraction between 0.7 and 0.8 did not contain a percolating cluster, and thus are not pictured on this graph.

The large differences seen here showcase some of the limitations of percolation type models that rely on averaged representations of structure. First, it is important to note that the structures analyzed here contained a single particle size and constant contact angle throughout the volumes. More complicated artificial structures, such as those having non-uniform particle size distributions and those with a wide range of neck sizes, are expected to result in even larger variations in performance near the percolation threshold. For more complicated artificial structures, it also becomes difficult to determine percolation thresholds and other fitting parameters used in the prediction of microstructural performance. Percolation thresholds derived from coordination number theories or numerical studies on different lattices [119], [120] may still vary greatly from the percolation threshold of a real, sintered electrode [18]. Lastly, while entire electrodes may be reasonably approximated as infinite domains when considering

microstructural features, active regions of composite electrodes are often much smaller in comparison [12], [35], [121], [122]. Thus, finite domain percolation effects may be present in a real electrode where maintaining fully percolating clusters is most important to overall device performance. This is especially the case when one or more of the phases of interest in an electrode are near their percolation threshold.

3.4.3 Conductivity of Real Microstructures

Each of the real three-dimensional microstructures listed in Table 3.1 was analyzed via the ECF model using partitioning method 2 with shape fitting. Fixed potential boundary conditions were applied across two opposing faces of the structures, and total resulting current was computed from the resolved electrochemical fin network. From the results of this calculation, a three-dimensional potential distribution within the structure may be obtained. The resulting potential distribution is shown in Fig. 3.6a and b for the GDC phase of a GDC-CFO sample microstructure computed using both the ECF model and the FE model described in Section 3.3.2. Normalized effective conductivities were then computed from ECF theory via Eq. 3.21 and compared to results of corresponding FEA in Abaqus. A comparison of normalized effective conductivities is shown in Fig. 3.6c for the two different models for each structure analyzed.

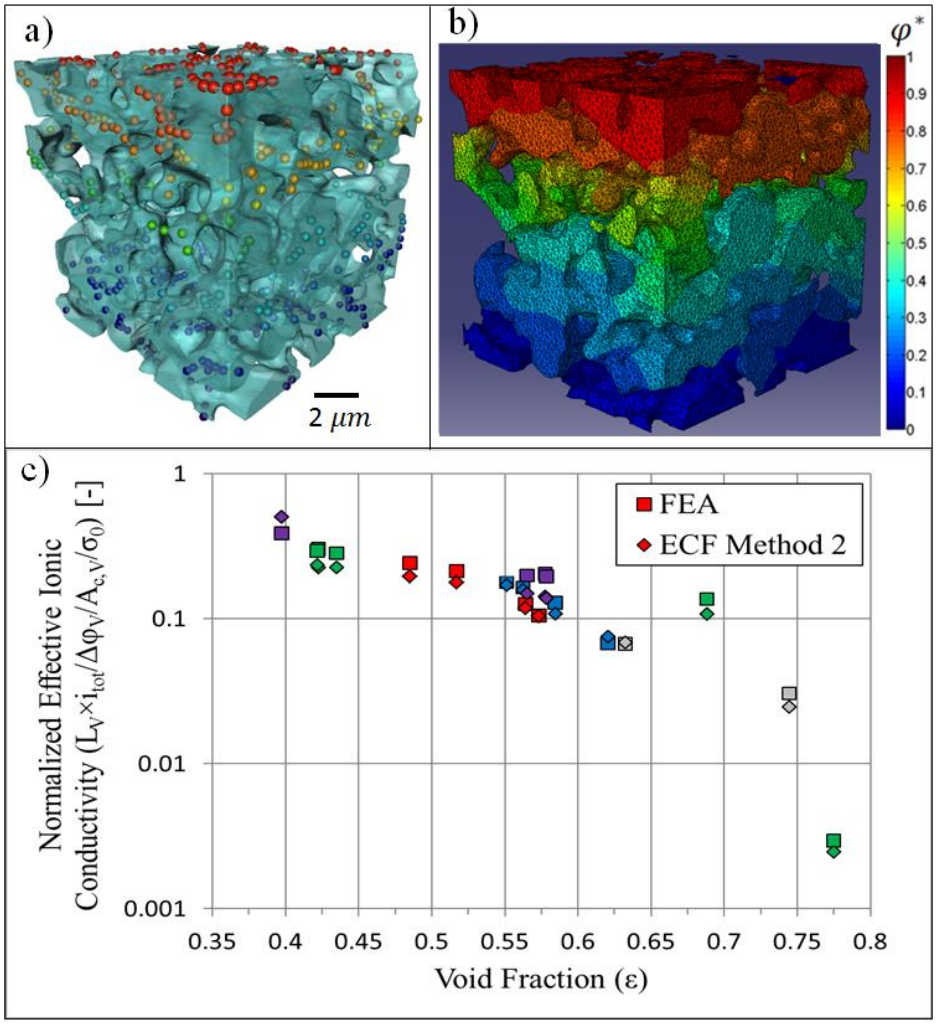

Figure 3.6. Dimensionless potential distributions computed by (a) electrochemical fin theory and (b) finite element analysis for the GDC ($Ce_{0.8}Gd_{0.2}O_2$) phase of a GDC-CFO gas separation membrane material. (c) Normalized effective conductivities of real microstructures as computed by electrochemical fin (ECF) theory and finite element analysis (FEA). Material phases shown are GDC (red), CFO (blue), Pore (green), SDC (purple), and Ni (gray). This figure is from Ref. [4].

It is apparent that a majority of the structures were under-estimated in terms of their conductivity by the ECF model when compared to finite element predictions. In fact, the mean percentage error of ECF predictions compared to the FE model was -12%. One possibility for this under-estimation of conductivity is the manner in which surface area to volume ratio was computed for each of the segments in a structure. While the end areas were measured via projection planes yielding flat surfaces, the external surface area and volume was measured from the actual partitioned segments, thus flat end areas were not imposed during these measurements. A possible result is that segments within material junctions in the structure, where non-flat areas are prominent, yield surface area to volume ratios that are not entirely representative of the conduction path morphology through the junction. An illustration of this possible effect is shown in Fig. 3.7.

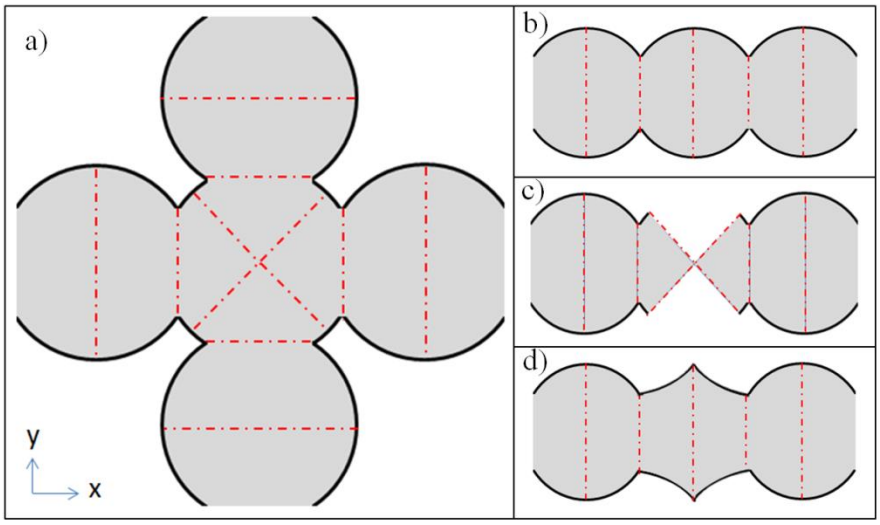

Figure 3.7. A schematic of a material junction including partitioning cut planes is shown (a). The accurate fin network representation of x-direction transport is pictured (b) along with a schematic of the material being counted for surface area and volume calculations (c). A possible

resulting fin network after shape fitting with this method is then shown (d). This figure is from Ref. [4].

The maximum error between the approaches was found to be 30%, which occurred for the SDC40 sample. This structure in particular required the use of 6792 fins in its equivalent ECF network, while the remaining volumes analyzed only required on average 1100 fins. This drastic difference is attributed to the feature sizes of the SDC40 sample compared to the other samples. Indeed, it appears that structures with very small feature sizes relative to voxel resolution of the structures result in some loss of information due to the extensive partitioning required. There are a number of additional approximations made by the ECF model employed that are probable sources of discrepancies between the approaches. First, approximating real amorphous microstructures with a series of axisymmetric fins may produce some error attributed to the complexity of the real conduction channels being analyzed. Second, the assumption of one-dimensional transport, as discussed in Section 3.4.1, can result in slightly over-estimated performance predictions. This effect is more prominent in fins with large changes in cross-sectional area along its transport axis. Third, the requirement of conducting channels with no more than two boundary faces complicates the treatment of material junctions in a structure, possibly resulting in the effect shown in Fig. 3.7. A more reliable means of computing surface area to volume ratio for shape fitting could be obtained by measuring the value entirely via projected planes along the length of a segment's skeleton. Fourth, mesh generation prior to FE simulations is no trivial step. It is expected that small errors in characterizing constrictions and other relevant morphological features of each structure could have a significant impact on the results [33]. While care was taken in ensuring high mesh quality for each structure, it is

uncertain what quantitative effects this may have on final calculations. Finally, imposed boundary conditions differ slightly between the ECF and FEA approaches. In the ECF model, boundary conditions are imposed at nodes which represent circular end areas for segments contacting the boundary face; while in the FE model, boundary conditions are imposed on the real amorphous surfaces contacting the boundary face. Thus, it is possible for the total boundary surface of the real structure to be improperly represented by fin end areas in the ECF model.

For each of the real microstructures analyzed, time to complete the solution step as well as computer memory required are shown for the ECF model and FE model in Fig. 3.8a and b, respectively. From this data it can be seen that on average, finite element solutions require roughly 3 orders of magnitude additional time and 5 times as much RAM. However, these differences in computational costs are highly dependent on the number of fins resulting from the partitioning step, and the number of mesh elements used to represent the structure in the FE model.

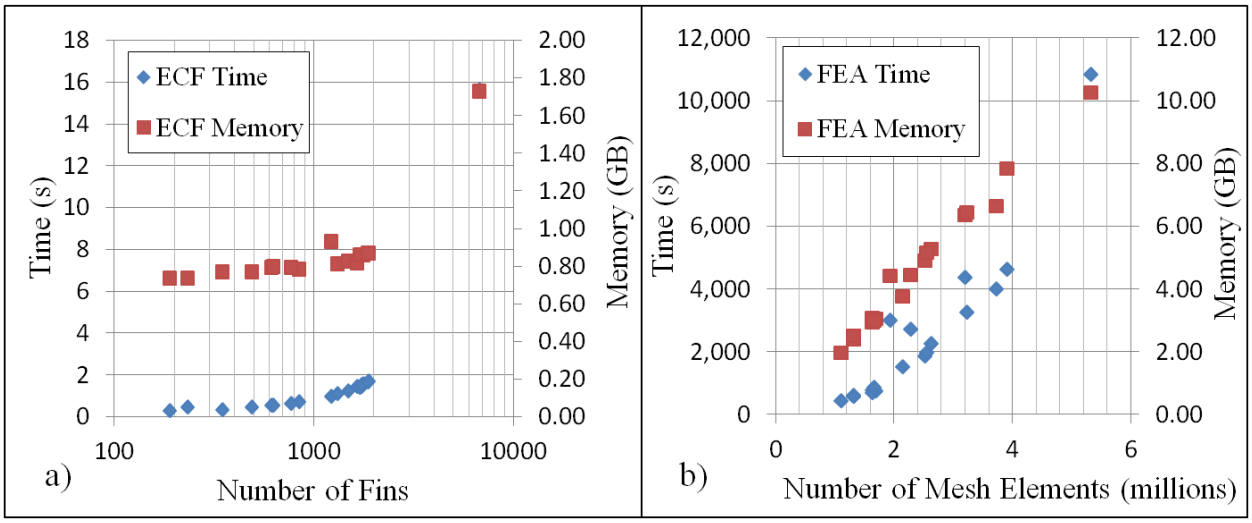

Figure 3.8. Computational time and memory required to complete solution step for real structures using a) electrochemcial fin (ECF) model and b) finite element analysis (FEA) model. This figure is from Ref. [4].

3.4.4 Applicability of the Electrochemical Fin Model

The electrochemical fin model presented herein has been discussed as a complementary approach to detailed numerical models such as finite element or Lattice-Boltzmann methods for the design of advanced electrochemical electrodes. Based on the presented results, the advantages of utilizing such a preliminary design screening tool are three-fold.

First, the analytical solutions for charge transfer that have been developed as part of electrochemical fin theory allow detailed comparison of performance between charge conducting structures without confounding morphological effects with numerical error. If such a comparison were to be made with a mesh-based approach, great care must be taken to ensure

results are mesh-independent; in this context analytical solutions are simpler to draw conclusions from keeping in mind that the solution may be less accurate than finite element or Lattice-Boltzmann methods. The second benefit to using electrochemical fin theory is the significant reduction in computational requirements that results from the use of closed-form analytical solutions and requiring fewer elements to represent a given structure than a more detailed finite element analysis. This is especially the case for artificial or ideal structures that are composed of axisymmetric building blocks, i.e. in the case of packed sphere structures, where the analytical fin solutions are directly representative of the axisymmetric conduction channels being analyzed. A detailed comparison between the ECF approach and a finite element analysis showing computational run time and memory requirements along with accuracy trade-offs is shown in this study and Ref. [102]. The third advantage of the electrochemical fin tool is its underlying analysis of the network structure of a microstructure. The skeletonization step of the partitioning tool results in a detailed network mapping of the underlying transport pathways in a structure. This information may be used for further characterization of connectivity and network topology that is not readily available from traditional mesh-based modeling tools.

3.5 Conclusions

In this study, an electrochemical fin model has been used to model the transport characteristics of artificial and real microstructures, with a focus on SOFC electrode materials. The application of analytical solutions for transport through negative, neutral, and positive curvature fin profiles has enabled the modeling tool to account more accurately for transport channel morphology, allowing performance predictions inclusive of geometry effects. Enhanced geometric sensitivity

has also been obtained by allowing the partitioning tool employed to monitor local variations in cross-section and sub-partition the microstructure at local minima and maxima in the channels.

The effects of an assumption of one dimensional transport have first been assessed for simple arrays containing fins of varying geometries. It was found that electrochemical fin theory will over-estimate the conductivity of a transport channel with respect to more detailed numerical simulations performed with finite element software due to cross-sectional averaging of the potential through a fin. The magnitude of this effect differs based on fin shape and is expected to be more prominent for fins with especially narrow regions.

Effective conductivities of various packed sphere structures were then computed and compared with finite element predictions and percolation theory. The electrochemical fin model is shown to agree well with FEA, given that fin geometries are selected to best represent the underlying structure. Comparing to percolation theory, it is determined that local microstructure effects can produce discrepancies between discrete and averaged approaches which may be critical to modeling performance of material phases in the vicinity of their percolation thresholds.

Real structures were then analyzed to validate the use of electrochemical fin theory as a meso-scale design screening tool. Conductivities computed by electrochemical fin theory are found to be within 30% of finite element calculations for a range of complex microstructures, thus validating the application of the fin model for rapid performance assessment.

It is determined from these results that representing complex microstructural networks via electrochemical fin networks is a viable method of simplifying performance calculations. However, certain underlying assumptions of the modeling approach limits its potential accuracy, perhaps most notably the assumption of one dimensional transport but also the requirement of ideal axisymmetric fins. It is therefore concluded that the ECF model is best used to predict performance of structures whose building blocks are axisymmetric or nearly axisymmetric. In this regard, the modeling tool is capable of providing accurate, rapid assessment of microstructural performance for the directed design of more promising electrodes.

Chapter 4*: Electrospun Polymer Electrolyte Membrane Conductivity Analysis

***Adapted from** [123]

4.1 Overview

As mentioned in Section 1.3.2, electrospinning has been demonstrated as a promising fabrication technique for PEMs that result in membranes with high ionic conductivities and mechanical stability. It is expected that, based on the interplay between charge transport and underlying membrane structure in traditional polymeric fuel cell membranes [64], membranes fabricated via electrospinning could exhibit distinct charge transport behavior based on their underlying microstructural morphologies [124], and therefore react uniquely to adverse conditions such as the presence of CO_2 in AAEMFCs. In order to support further development of advanced membranes (fabricated by e.g., electrospinning), it is warranted to develop and utilize computational and theoretical models that are sensitive to these distinct microstructural morphologies for predicting membrane performance under a wide range of conditions.

In this chapter, numerical and analytical models are developed and presented to predict charge transport in membranes with fiber network microstructures. The Fiber Network (FN) model was first created to predict ionic conductivities of polymeric composite membranes produced by electrospinning. This model relies on the solution of random resistor networks that represent the conducting fiber morphology of the membrane via application of an existing analytical electrochemical fin theory [83]. The model can accommodate a wide range of fibrous membrane morphologies and can be readily combined with more detailed physical models that, for instance, model the effects of CO_2 absorption on OH^- conductivity in AEMs [125]. Here, transport of ions

occurs via simple diffusive mechanism in the case of an applied electrical potential gradient [47]. To aid in development of the model, the works of Park et al. [48] and Ballengee et al. [52] are used as references for describing the electrospinning approach and resulting membrane morphologies, and providing conductivity data for, AEMs and PEMs, respectively. The model is then used to predict membrane ion conductivities for an electrospun AEM composed of Chloromethylated polysulfone (CMPSF) nanofibers and poly(phenylsulfone) PPSU supporting matrix and a PEM composed of Nafion nanofibers and PPSU matrix, after calculating fiber conductivity to match a single experimental conductivity data point for each material. The model predictions agree well with experimental measurements for ionic conductivities, showcasing the FN model as a viable means of modeling charge transport behavior in fibrous ionomeric membranes. Results from a recently developed Effective Medium theory (EMT) are also presented for comparison to FN model predictions of electrospun AEM conductivity as additional validation of the approach. Based on insight gained from the FN model, simple resistor-based closed-form analytical solutions have been developed to predict conductivity of electrospun membranes given easily obtained structural parameters relevant to the electrospinning process and fitting a constant (accounting for nanofiber conductivity and fiber layering) to one experimental data point. To further illustrate the benefits of the models developed in this work, conductivity predictions using an existing transport model from Porous Media Theory (PMT) are compared to FN model predictions for an electrospun PEM. To apply PMT, estimates of tortuosity for various electrospun membranes are obtained via outputs from the FN model. The application of PMT and EMT to predicting transport in electrospun membranes is an example of using macrohomogeneous models to account for detailed microstructural effects that can arise in an actual system.

4.2 Charge Transport Modeling

4.2.1 Fiber Network Model

The goal of this model is to approximate the 3-D morphology of electrospun nanofiber composite membranes including membrane swelling in the presence of water, and compute resulting transport properties such as in-plane and thru-plane ionic conductivities. These resulting conductivities can be validated with experimental data and/or used to back out fiber conductivities for additional modeling and validation. The electrospinning processes detailed in Refs. [48] and [52] are used as the basis for developing this model. A basic picture of the electrospinning process taken from Ref. [48] is shown in Fig. 4.1a. Here, a syringe filled with the necessary polymer solutions (i.e. two simultaneously spun nanofibers) is pointing toward a rotating and laterally oscillating collector drum surface. When the fiber leaves the syringe (due to a voltage drop between the fiber and the syringe), instabilities in the fiber cause it to whip and deposit in a random pattern on the collector surface. This process is continued until a sufficient amount of fiber is deposited, whereupon the resulting composite polymer mat is processed into compacted membranes consisting of a conducting nanofiber network and a surrounding uncharged insulating polymer matrix. An SEM image of the resulting conducting fiber network taken from Ref. [48] is shown in Fig. 4.1b, where the insulating PPSU phase has been removed from the membrane for a clearer picture.

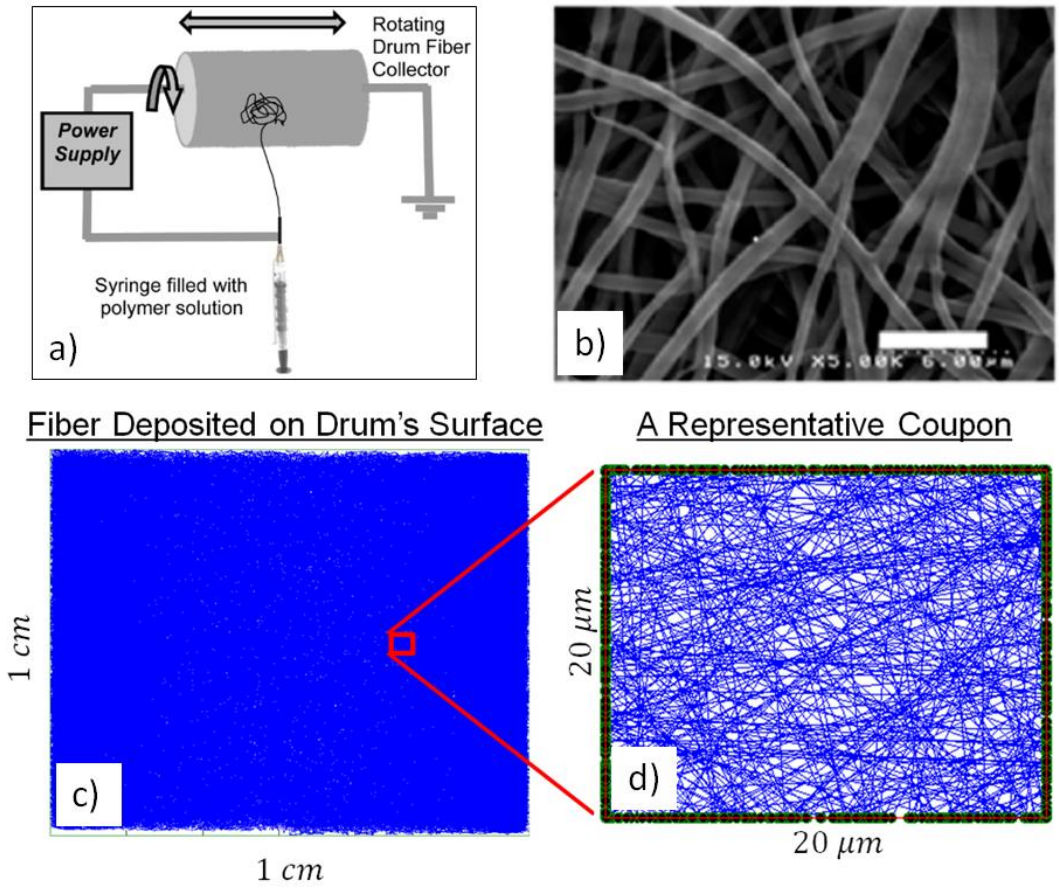

Figure 4.1. A simple schematic of the electrospinning process is shown (a), along with an SEM image of the resulting conducting fiber network after the inert PPSU phase was removed (b). A digitally constructed electrospun membrane from the FN model (c), and an extracted statistically representative coupon are also pictured (d). This figure was adapted from Ref. [48].

The Fiber Network model encompasses six steps, which will be listed here and discussed in detail below, including all relevant assumptions and procedures. They are:

1. Define user inputs to resemble a real system.
2. Generate a digital electrospun membrane by approximating the electrospinning fiber deposition process. Since a full-scale membrane would require too much time and

computer memory to analyze, representative coupons are generated and analyzed to predict the full membrane's transport properties.

3. Find all relevant contact points between conducting fibers.
4. Determine how the membrane changes during water swelling by approximating the swelling process.
5. Convert the deposited, swelled fiber network to a resistor network composed of cylindrical electrochemical fins in order to model the in-plane and thru-plane conduction cases.
6. Using Kirchhoff's circuit laws, solve the resistor network problem for both the in-plane and thru-plane cases, and compute relevant transport properties.

Following these steps, the outputs from the resistor network analysis can be used to generate any number of relevant plots, including the potential distribution throughout the structures in both the in-plane and thru-plane cases.

4.2.1.1 Model Input Parameters

The user input parameters for this model fall under four categories: fiber deposition parameters, coupon definition parameters, swelling parameters, and material properties/boundary conditions. The fiber deposition parameters of interest are the drum dimensions (width, diameter), drum rotational speed and lateral oscillation rate and amplitude, the size of the fiber whipping region as it is deposited, and the conducting fiber flow rate. In order to define the representative coupon (representing the membrane), the conducting fiber radius and volume fraction, and coupon dimensions (length, width, thickness) must be defined. The coupon thickness is defined based

on the thickness of one layer of fiber, δ, idealized as a 2-D sheet of deposited fiber, and the number of layers, n, that make up the coupon. Additional details on fiber layering will be provided below. The parameters that define membrane swelling are the density ratio of conducting fiber to PPSU, the density ratio of PPSU to water, and the fractional weight gain of a membrane after it is swelled with water. Finally, the material properties of interest are the fiber ionic conductivity and surface charge transfer resistance, and the boundary conditions that may be defined are either electrode voltages (Dirichlet type) or currents (Neumann) for both the in-plane and thru-plane cases.

4.2.1.2 Digital Structure Generation

The real electrospinning process is complex, and consists of many steps including preparation of conducting fiber material, electrospinning of two simultaneous polymers via applied voltages on moving drums, cross-linking of fibers, membrane compaction, vapor exposure, quaternization, etc. The FN model aims to approximate this process such that it results in a pre-swelled, compacted membrane composed of layered, geometrically and spatially-defined conducting fibers, assumed to be completely surrounded by a solid PPSU insulating matrix phase. To do this, a number of assumptions must be made.

First, only the conducting fiber is modeled as being deposited on the collector surface; the insulating matrix is assumed to surround the conducting fiber and fill in all void space. Second, the fiber is assumed to whip randomly within a user-defined region as it is deposited. In the real deposition process, this fiber whipping occurs because of bending instabilities in the fiber as charge builds on the fiber surface [126], [127]. Third, the fibers are collected on the surface of a

drum that is rotating and laterally oscillating. This drum surface is approximated as flat (2-D), and the fibers are approximated as straight, connected, 2-D, randomly oriented line segments of varying length simulating electrospinning using a continuous fiber. Any 3-D orientation of the fiber in the real system is assumed to be small compared to the length of the fiber in the 2-D flat plane in which it resides, and is only taken into account when a resistor network is constructed. During the real electrospinning process described by Ref. [48], once all fiber has been deposited on the collector surface, 1 cm by 1 cm squares of fiber composite are cut out and are then processed to become membranes. In the FN model, it is assumed that small coupons on the order of single to tens of microns can be extracted from the 1 cm by 1 cm membranes whose resultant transport properties are statistically representative of the entire membrane. Thus, during the modeled deposition process, only fibers that lay within the user-defined coupon region are of interest and kept for further analysis. For an illustration of this step, see Fig. 4.1c and d.

The steps for the digital deposition process are as follows. Beginning with the fiber instability region (syringe location) at an arbitrary location on the collector's surface, a straight randomly oriented line segment is created, whereupon the position of the instability region with respect to the collector's surface is then moved according to the fiber flow rate (or, how much time has passed). This process is repeated many times with each newly laid fiber being connected to the previous one. Since we are only interested in the representative coupon, only pieces of fiber that fully or partially lay inside the coupon or cross the coupon boundaries are kept, and are cut at the coupon boundaries. Therefore, while the fiber that is laid on the collector's surface is continuous and all segments are connected, depending on the coupon size most of the fibers will be disconnected fibers that span the boundaries of the coupon. No fiber is kept that is laid

completely outside the coupon during this process. An alternative means of filling a user-defined coupon with fiber is to simply define a 2-D coupon size, such as $20\ \mu m$ by $20\ \mu m$, and then continuously fill the coupon with randomly oriented fibers that span the coupon boundaries. The resulting morphology is effectively the same as that produced by the deposition process outlined above, and requires much less time to generate.

Regardless of the deposition method chosen, the process is stopped when the total length of fiber deposited inside the user-defined coupon meets requirements specified by the user. The total length of fiber inside the coupon is defined according to the definition of volume fraction (total volume of conducting fiber divided by total coupon volume), and is shown in Eq. 4.1.

$$L_f = \frac{fTwL}{A_f} \tag{4.1}$$

Here, f is the user-defined volume fraction of conducting fiber, $L, w,$ and T are the length, width and thickness of the coupon, respectively, and A_f is the cross-sectional area of the fiber. This process can be used to construct coupons that are composed of n layers, where statistically, the length of conducting fiber that composes each layer is L_f/n.

4.2.1.3 Determine Fiber Contact Points

The coupon resulting from the deposition process now contains a total length of fiber L_f, which is distributed between n layers. The number of layers n is user defined, and all the layers are virtually stacked on top of each other to form a pseudo-three-dimensional volume. However, at this point, defining a third spatial coordinate (z) for any of the fibers is not necessary, and will only come into play when constructing the resistor network, thus each of the fibers is only

defined in 2-D space. Additionally, since a typical coupon is very small compared to the fiber instability region during deposition, most of the fibers within the coupon traverse the entire coupon laterally; only rarely does a fiber endpoint fall within the coupon's interior.

Within each layer, fibers that cross each other in 2-D space are assumed to have ionic contact between them, that is, ions are allowed to flow between fibers by travelling through their points of contact. At the contact point between any two fibers, the fibers themselves are assumed to not deform plastically, thereby maintaining their cross-sectional shape. Every contact point within a layer is book-kept as a valid contact point, and is referred to as an *intra-layer contact point*. Since there are multiple layers within the coupon and they are stacked on top of one another, it is assumed that there is also ionic contact between adjacent layers. Therefore, contact points between any two fibers that lay in adjacent layers are also book-kept as valid points, and are referred to as *inter-layer contact points*. Any contact points in 2-D space between any two fibers that have one or more layer separating them, i.e. they are in non-adjacent layers, are not kept as they are invalid contact points. For an illustration of valid contact points and layering within a coupon, see Fig. 4.2. In Fig. 4.2, a single layer of conducting fibers is shown (Fig. 4.2a), whereupon numerous layers are stacked (Fig. 4.2b), and a full coupon is constructed (Fig. 4.2c). *Inter-* and *intra-layer* contact points are shown and the valid contact points for a sample coupon are marked with red crosses (Fig. 4.2c).

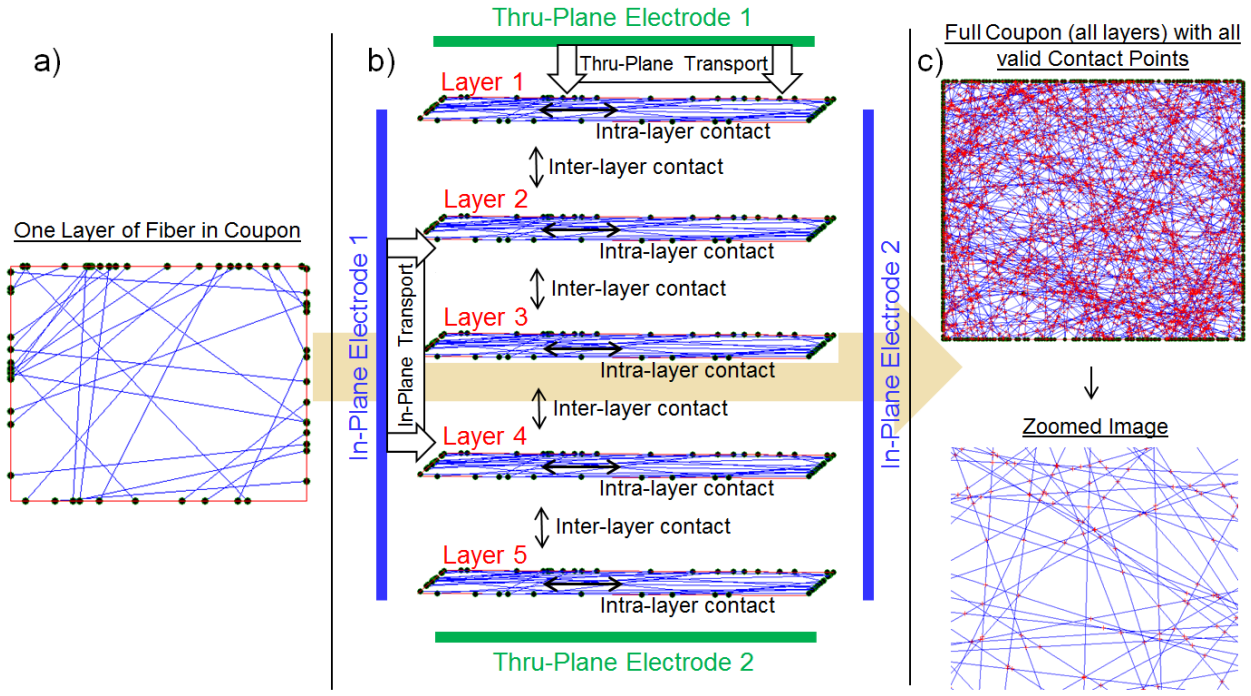

Figure 4.2. A single layer of fiber (a), stacked with additional layers of fiber (b) to produce a full coupon (c). Inter and intra-layer contact points are shown qualitatively (b) and marked for a sample coupon with red crosses (c). The directions of transport and electrode locations for the in-plane and thru-plane cases are also shown (b). This figure is from Ref. [123].

With all relevant contact points found in a coupon, we can now define the concept of nodes and segments. Based on the fiber network morphology, a *node* is defined as any fiber endpoint or valid contact point in the structure. A *segment* is defined as any length of fiber that forms a connection between two nodes. With those defined, the coupon's boundary conditions may now be determined. For the in-plane conduction case, within all layers of the coupon, any node that lies on a coupon boundary that is chosen as an in-plane electrode is considered a boundary node and is assigned the corresponding boundary condition. An example for the in-plane case is shown in Fig. 4.2b. In this figure, in the case of Dirichlet-Dirichlet boundary conditions, all nodes (fiber endpoints or contact points) that lie on the left boundary will be assigned the voltage

of electrode 1. All of the nodes lying on the right boundary will be assigned the voltage of electrode 2. For the thru-plane case, in a coupon composed of n layers, all nodes (fiber endpoints and contact points) that lie in layer 1 and layer n are set as boundary nodes. For the example shown in Fig. 4.2b, all nodes that exist in layer 1 will be assigned the voltage of electrode 1, and all nodes that exist in layer 5 will be assigned the voltage of electrode 2.

4.2.1.4 Membrane Swelling Model

In a real IEM system, the membranes are swelled with water to facilitate transport of ions, and all experimental conductivity measurements taken on the membrane are in its swelled state. Therefore, beginning with the dry, as-spun coupon as described by the previous steps, it is desired to compute the amount of swelling that will occur in the presence of water and how the coupon morphology will change accordingly.

It is first assumed that the PPSU material that forms the insulating matrix phase surrounding the conducting fiber is completely hydrophobic, thus any water absorbed by the membrane is taken up entirely by the conducting fiber. The resulting change in volume experienced by the conducting fiber leads to change in total coupon volume, i.e. the coupon expands when swelled; therefore it is assumed that the PPSU matrix is amenable to allowing expansion and is not rigid, but does not change in volume. This swelling also is reflected in a change in volume fraction for the two phases, which must be accounted for. During swelling, it is assumed that any fiber contact points that were valid before swelling are still valid. In other words, the connectivity of the coupon remains the same after the swelling process. The amount of swelling by weight is also assumed to vary with dry (pre-swelling) volume fraction. Consistent with Refs. [48] and

[52], in general, the more conducting fiber that is present in the dry membrane, the more the coupon swells. This occurs because the presence of the supporting PPSU matrix inhibits swelling, thus lower volume fractions of PPSU allow the conducting fiber to swell with less restraint.

Finally, the coupon dimensions and fiber dimensions must change when the total coupon volume changes. In this work, two cases were implemented in the FN model. The first case is that of isotropic volume expansion. In this case, each of the coupon dimensions expands isotropically (length, width, thickness), according to a scale factor that is determined by the amount of total coupon swelling. For this swelling model, since the coupon has experienced areal swelling (i.e. the planform of the coupon is swelled), the fiber length must also swell proportional to this scale factor. To accommodate the remaining swelling in the volume, the fiber radius must then increase. The second case is that of anisotropic, or constrained, volume swelling. This case assumes that no areal swelling of the coupon occurs, and volume expansion only occurs in the thickness direction. Accordingly, only the fiber radius is allowed to swell, while the fiber length remains the same. It is envisioned that a real system will exhibit swelling behavior that falls somewhere between these two models, depending on the structure of the membrane. According to Ref. [52], a membrane composed of hydrophobic PPSU nanofibers embedded in an ion conducting matrix will tend to swell mostly in the thickness direction due to minimal PPSU connectivity in the thickness direction, resulting in low mechanical resistance to swelling in that direction. Furthermore, in the case of conducting nanofibers embedded in a PPSU matrix, there is high 3-D connectivity for both phases; thus there is no preferred swelling direction, resulting in isotropic coupon swelling.

For a conceptual picture of isotropic coupon swelling, see Fig. 4.3. In order to compute coupon and fiber dimensions after swelling, we start with a definition of dry and wet volume fractions of the conducting fiber, shown by Eqs. 4.2 and 4.3, respectively.

$$f = \frac{V_f}{V_f + V_p} \tag{4.2}$$

$$f_w = \frac{V_{f,w}}{V_{f,w} + V_p} \tag{4.3}$$

From the definition of gravimetric swelling as proposed by Park et al. [48], swelling parameter s is defined by Eq. 4.4.

$$s = \frac{\frac{\rho_w}{\rho_p}\left(\frac{V_{f,w}}{V_p} - \frac{V_f}{V_p}\right)}{1 + \frac{\rho_f}{\rho_p}\frac{V_f}{V_p}} \tag{4.4}$$

Combining Eqs. 4.2, 4.3, and 4.4, and rearranging leads to the following expression for swelled volume fraction of the conducting fiber:

$$f_w = \frac{\left(\frac{f}{1-f}\right)\left[s\frac{\rho_p}{\rho_w}\frac{\rho_f}{\rho_p} + 1\right] + s\frac{\rho_p}{\rho_w}}{1 + \left(\frac{f}{1-f}\right)\left[s\frac{\rho_p}{\rho_w}\frac{\rho_f}{\rho_p} + 1\right] + s\frac{\rho_p}{\rho_w}} \tag{4.5}$$

Similarly, the ratio of the total volume of the coupon when swelled to the total volume of the coupon pre-swelling is shown by Eq. 4.6.

$$\frac{V_{t,w}}{V_t} = \frac{1 + \left(\frac{f}{1-f}\right)\left[s\frac{\rho_p}{\rho_w}\frac{\rho_f}{\rho_p} + 1\right] + s\frac{\rho_p}{\rho_w}}{1 + \frac{f}{1-f}} \tag{4.6}$$

In the isotropic swelling case, all three coupon dimensions must scale according to the same scale factor. The scale factor is defined by Eq. 4.7, below.

$$SF = \sqrt[3]{\frac{V_{t,w}}{V_t}} \tag{4.7}$$

From Eq. 4.7, the new coupon dimensions and total conducting fiber length inside the coupon can be defined by Eqs. 4.8-11.

$$L_w = SF * L \tag{4.8}$$

$$w_w = SF * w \tag{4.9}$$

$$T_w = SF * T \tag{4.10}$$

$$L_{f,w} = SF * L_f \tag{4.11}$$

Since the coupon morphology and connectivity is to remain the same after swelling, the number of layers in the coupon is kept constant, thus $n_w = n$. Accordingly, the layer thickness of the coupon must scale as $\delta_w = SF * \delta$. Finally, the fiber diameter (or radius) can be determined after swelling by Eq. 4.12.

$$\frac{d_{f,w}}{d_f} = \sqrt{\frac{1}{SF}\left[\left(s\frac{\rho_p}{\rho_w}\frac{\rho_f}{\rho_p} + 1\right) + s\frac{\rho_p}{\rho_w}\right]} \tag{4.12}$$

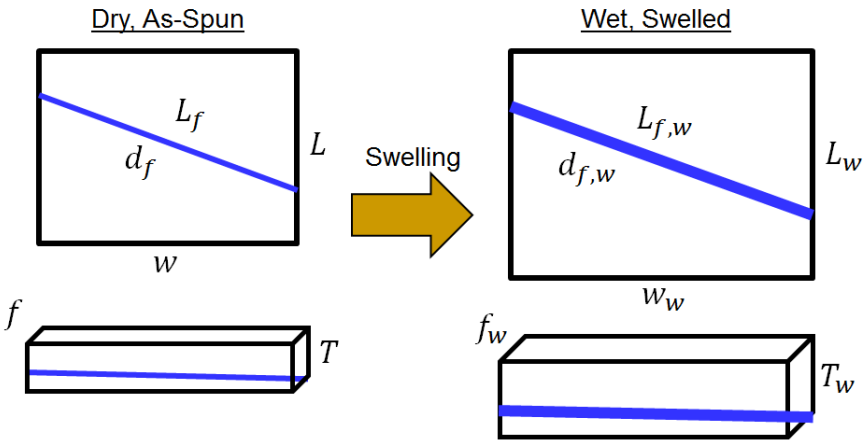

Figure 4.3. Isotropic swelling of a coupon, where coupon dimensions and fiber dimensions all expand to accommodate water uptake. This figure is from Ref. [123].

The anisotropic swelling model assumes that all volumetric swelling is manifested in an increase in coupon thickness, and the fiber only swells radially. Thus, coupon length and width, along with fiber length, remain the same. However, layer thickness and total coupon thickness can be computed by:

$$\delta_w = \left(\frac{V_{t,w}}{V_t}\right)\delta \tag{4.13}$$

$$T_w = \left(\frac{V_{t,w}}{V_t}\right)T \tag{4.14}$$

The corresponding increase in fiber diameter can be calculated by Eq. 4.15.

$$\frac{d_{f,w}}{d_f} = \sqrt{\left(s\frac{\rho_p}{\rho_w}\frac{\rho_f}{\rho_p} + 1\right) + s\frac{\rho_p}{\rho_w}\left(\frac{f}{1-f}\right)} \tag{4.15}$$

4.2.1.5 Constructing the Electrochemical Fin Network

The fiber network morphology after swelling must now be converted into a resistor network for transport calculations. For this step, an existing electrochemical fin theory [83], [87] is adapted to construct and solve the resistor network. Since we are interested in both the in-plane and thru-plane cases, two separate resistor networks must be created to reflect the two cases. Within the resistor networks, the properties of the resistive components are modified depending on which conduction case is being modeled.

In order to construct resistor networks, we first assume that all valid contact points between fibers have zero resistance to ion flow. Instead, the length of fiber between nodes provides the resistance to ion flow; however, the lengths of the resistive components are defined differently in the in-plane and thru-plane cases (see following discussion). To apply the electrochemical fin theory, each fiber in the resistor network is assumed to be an axisymmetric, cylindrical electrochemical fin of constant cross-section. Since we are not interested in electrochemical reactions, surface charge transfer is neglected, thus only bulk ionic diffusion is being modeled. In order to define an electrochemical fin, the fiber radius, resistive length, and conductivity are needed. The fiber radius is simply found by Eq. 4.12 or 4.15 depending on the swelling model chosen, and the fiber conductivity is a user input. Finally, to construct the resistor network, each fiber segment in the fiber network is assigned a resistor number, which is then bookended by two network nodes. This provides a convenient mapping of the network's connectivity.

To define resistive length for the electrochemical fins, we must first make some assumptions for the in-plane and thru-plane cases. For a schematic of the swelled coupon, in terms of layer

location in 3-D and relevant coordinate axes, see Fig. 4.4a. In the case of in-plane ionic conduction, the major potential gradient is assumed to occur in the x or y-direction. Thus, choosing any (x,y) coordinate in the coupon will yield, approximately, a constant voltage along all z. In other words, all layers in a coupon will have approximately the same potential distribution, therefore negligible transport is assumed to occur between layers. For the thru-plane case, the major potential gradient is assumed to be in the z-direction, therefore 3-D transport becomes important. Thus, for the thru-plane case, z coordinates must be given to each of the nodes in the structure to approximate z-direction transport. To do this, we return to Fig. 4.4. As shown by Fig. 4.4a, in a coupon of swelled thickness T_w and composed of n layers, each layer occupies some 2-D plane in 3-D space. The first (lowest) layer is chosen to occupy $z = \frac{\delta_w}{2}$, and the final (highest) layer occupies $z = T_w - \frac{\delta_w}{2}$. Intermediate layers occupy intermediate values of z. The distance between any two consecutive layers is always δ_w, and conceptually, assuming in the real system the fibers are oriented slightly out of plane, this value of δ_w should always be of the same order of magnitude and slightly higher than $d_{f,w}$. All intra-layer contact points and fiber endpoints must take on the z-value of the layer that contains them (solid lines in Fig. 4.4a), while all inter-layer contact points take on a z-value that is half way between the two layers that make up the contact point (dashed lines of Fig. 4.4a).

The resistive length of a fiber is now defined as an approximate length of the flow path that ions must traverse when traveling through a fiber in a coupon. The geometric length of a fiber, on the other hand, is simply the 2-D length of any fiber within a layer, which holds true for both in-plane and thru-plane cases. For reference, see Fig. 4.4b. As shown in Fig. 4.4b, the in-plane resistive length is merely defined as the geometric length for a given fiber segment since z-

direction transport is assumed to be negligible. Conversely, thru-plane resistive length is calculated as the sum (not the vector sum) of the geometric length of a fiber and the difference between the z-coordinates of the nodes that define that fiber segment, or resistor.

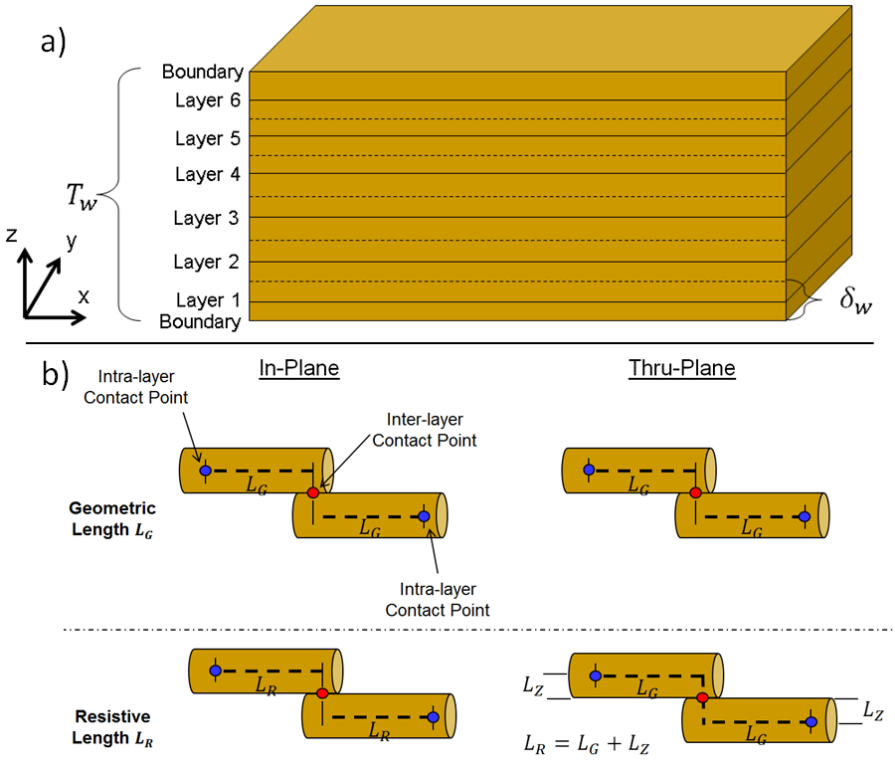

Figure 4.4. The locations of layers in 3-D for a swelled coupon in the FN model (a), and resistive and geometric fiber length definitions for the FN model (b) for the in-plane and thru-plane case. The length that is counted is represented by the bold dashed lines. This figure is from Ref. [123].

4.2.1.6 Fin Network Solution

To solve the resistor networks described above, an identical approach is taken as discussed in Refs. [4], [102]. Assuming Kirchhoff's circuit laws, a set of linear equations is solved, resulting

in the currents passing through each resistor (fiber segment), and the potential at each node. These outputs are distinct for the in-plane and thru-plane cases. In order to compute the effective ionic conductivity of the fiber networks, the total current must first be found by summing all currents passing through either of the faces where boundary conditions were applied. Effective conductivity is then computed by Eq. 4.16.

$$\sigma_{eff} = \frac{D * I}{\Delta V * A} \tag{4.16}$$

Here, D is the distance between the boundary faces where voltages were applied, I is the resulting total current in the structure, ΔV is the potential difference imposed on the structure, and A is the cross-section area of the coupon that is perpendicular to the direction of transport. In the in-plane case, D is the width or length of the coupon (depending on which boundary faces are selected), and in the thru-plane case D is the coupon thickness. Once effective conductivity is computed given an input fiber conductivity σ_f, σ_f can be adjusted in order to match experimental effective conductivity data in the literature. The resulting fiber conductivity is a backed-out conductivity that can be compared to values of nanofiber conductivity reported in the literature for different materials.

4.2.2 Effective Medium Theory

The extended EMT of Myles et al. [9], [74] is adapted in this work to estimate the effective conductivity of electrospun membranes that contain fiber-like inclusions. Typically, EMT relies on idealizing the morphology of a mixture such that analytical solutions of the electric field are possible (e.g. Laplace's equation); then combines these solutions to obtain an estimate for the effective conductivity of the mixture. This EMT is based on Bruggeman's unsymmetrical

theory, and was developed to simulate transport behavior of heterogeneous mixtures composed of an arbitrary number of inclusion types where each type has a unique shape (within the bounds of a spheroid), conductivity, and orientation (as specified by the orientation distribution function). The goals of applying this EMT model to the electrospun membranes was to first approximate a fiber conductivity that can be compared to the FN model, and then predict effective conductivity at different volume fractions for additional validation. To apply EMT, the fiber network morphology of an electrospun AEM [48] shown in Fig. 4.1b is first coarsely approximated by a collection of rods and spheres, where the rods represent the conducting phase and the spheres are the insulating material. The spheres have no preferred orientation and are randomly dispersed in the mixture, while the rods (prolate spheroids) are randomly oriented in a planar distribution, thereby approximating fiber layering. Based on these mixtures, effective in-plane and thru-plane conductivities can then be found and compared to experimental data.

4.2.3 Analytical Conductivity Models

Additional validation of the FN model may be obtained by deriving and applying simple analytical models to describe the behavior of in-plane and thru-plane effective conductivity with respect to membrane volume fraction. In this work, analytical models are developed to predict in-plane and thru-plane conductivity for both the isotropic and anisotropic swelling models presented above.

The analytical in-plane conductivity model is based on the assumption that in the in-plane case, charge transport only occurs within each layer. In other words, as stated above, all layers in a coupon will have approximately the same potential distribution, therefore negligible transport is

assumed to occur between layers. Following this assumption, a highly simplified coupon morphology can be created where in a coupon of n layers, each layer is composed of a number of fibers that run parallel to one another and span both in-plane electrodes. Since each of these fibers within a layer can be modeled as a simple resistor, the effective resistance of each layer can be found as:

$$R_{eff,L} = \frac{R_f}{n_{FL}} \tag{4.17}$$

where n_{FL} is the number of fibers in a layer, found by Eq. 4.18, below, and R_f is the resistance of each fiber, found by Eq. 4.19.

$$n_{FL} = \frac{fw\delta}{A_f} \tag{4.18}$$

$$R_f = \frac{l_f}{\sigma_f A_{f,w}} \tag{4.19}$$

Based on the assumptions used in developing the two swelling models, the number of fibers in a layer, n_{FL}, is the same before and after swelling. An effective resistance for the entire coupon can be determined noting that each of the n layers runs parallel to one another, and noting Eq. 4.17:

$$R_{eff} = \frac{R_f}{n_{FL}n} \tag{4.20}$$

The in-plane effective conductivity of the coupon can be found by inserting Eq. 4.20 directly into Eq. 4.16, noting the resistance of a fiber is found by Eq. 4.19 and $R_{eff} = \frac{\Delta V}{I}$. To simplify the model, a proportionality constant, k, is used, resulting in Eq. 4.21.

$$\sigma_{eff,IP} = k\frac{n_{FL}\sigma_f d_{f,w}^2}{\delta_w l_f} \tag{4.21}$$

Since we want the conductivity to be a function of swelled volume fraction, the volume fraction of conducting fiber in the entire coupon after swelling needs to be determined. To do this, we first assume that the total volume of conducting fiber is found by multiplying the volume of a single fiber that spans the in-plane electrodes by the total number of fibers in a coupon. The total number of fibers in the coupon is found simply by multiplying the number of fibers in a layer, n_{FL}, by the total number of layers, n. The total coupon volume is then determined by multiplying the volume of a single layer by the total number of layers, n. Noting that n appears in both the numerator and denominator, it can be cancelled out resulting in Eq. 4.22, below.

$$f_w = \frac{n_{FL}\frac{\pi}{4}d_{f,w}^2 l_f}{w_w^2 \delta_w} \tag{4.22}$$

Rearranging Eq. 4.22 and inserting into Eq. 4.21 yields Eq. 4.23, assuming $l_f = w_w$ (each fiber is the same length as the coupon along the primary transport direction). Here, any constants (such as $\frac{\pi}{4}$) are collected in the proportionality constant k.

$$\sigma_{eff,IP} = k\sigma_f f_w \tag{4.23}$$

Since the fiber conductivity is assumed to be constant, Eq. 4.23 can be adjusted to:

$$\sigma_{eff,IP} = C_1 f_w \tag{4.24}$$

where C_1 is a fitting parameter. Eq. 4.24 is valid for both the isotropic and anisotropic swelling cases, since swelled volume fraction of conducting fiber does not vary between models. The result of this model development is that regardless of the swelling model used, the in-plane effective conductivity for a coupon should vary linearly with the swelled volume fraction of conducting fiber.

The analytical thru-plane model assumes that for ions to travel from one layer to the next, they must pass through a series of resistors that combines in-plane transport in the two layers and thru-plane transport between layers (through a contact point). A picture of this simple resistor network is shown in Fig. 4.5a. Similar to the procedure of the in-plane model, an effective thru-plane resistance for each layer can be determined as:

$$R_{eff,L} = R_{IP} + R_{TP} \tag{4.25}$$

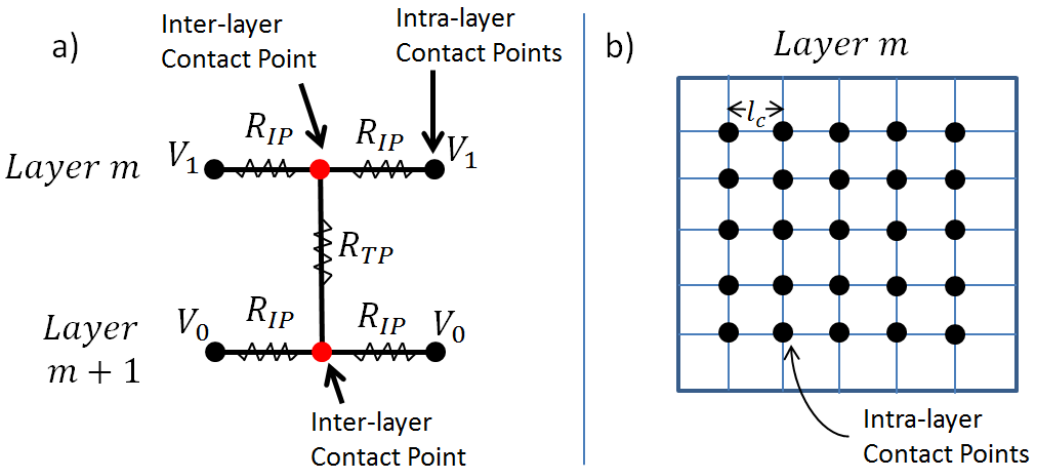

Figure 4.5. A simple resistor network schematic depicting the analytical thru-plane conductivity model between layers (a) and the formation of contact points within a layer (b). This figure is from Ref. [123].

An effective thru-plane resistance for the entire coupon can be determined by first assuming the thru-plane resistance of each layer is in series with one another, thus $R_{eff} = nR_{eff,L}$. Next, it is assumed that many of these thru-plane resistance paths are present in the coupon and each runs parallel to one another. The total resistance of the coupon can be found by simply assuming parallel resistors, and the effective thru-plane conductivity of the coupon is found by Eq. 4.26.

$$\sigma_{eff,TP} = \frac{\delta_w n_{TP}}{w_w^2 R_{eff,L}} \tag{4.26}$$

Here, n_{TP} is the number of thru-plane resistor paths running parallel to one another in the coupon, which is determined by considering Fig. 4.5b. Here, all of the fibers in each layer are assumed to form a grid-like pattern, where each of the contact points represents one thru-plane flow path. Assuming the number of fibers in a layer is still determined by Eq. 4.18, n_{TP} is determined by Eq. 4.27, below. The distance between two neighboring contact points in Fig. 4.5b can then be found by Eq. 4.28. Finally, the in-plane and thru-plane resistor components, R_{IP} and R_{TP} respectively, are derived and shown by Eqs. 4.29 and 4.30.

$$n_{TP} = \left(\frac{n_{FL}}{2}\right)^2 \tag{4.27}$$

$$l_c = \frac{w_w}{\left(\frac{n_{FL}}{2} + 1\right)} \tag{4.28}$$

$$R_{IP} = \frac{w_w}{n_{FL}\sigma_f A_{f,w}} \tag{4.29}$$

$$R_{TP} = \frac{\delta_w}{\sigma_f A_{f,w}} \tag{4.30}$$

Inserting Eqs. 4.29 and 4.30 into Eq. 4.26, and rearranging for total conducting fiber volume fraction from Eq. 4.22 yields:

$$\sigma_{eff,TP} = \frac{\sigma_f \delta_w^2 f_w n_{FL}}{4w_w^2 \left(\frac{1}{n_{FL}} + \frac{\delta_w}{w_w}\right)} \tag{4.31}$$

This equation is valid for both the isotropic and anisotropic swelling cases. In both cases, the number of fibers per layer, n_{FL}, can be determined from Eq. 4.18. To easily incorporate the relations governing both swelling models, Eq. 4.31 is modified to Eq. 4.32, below. Finally, the

thru-plane conductivity can be determined by Eqs. 4.33 and 4.34 for the isotropic and anisotropic swelling models, respectively.

$$\sigma_{eff,TP} = \frac{\sigma_f \delta^2 \left(\frac{\delta_w}{\delta}\right)^2 f_w n_{FL}}{4w^2 \left(\frac{w_w}{w}\right)^2 \left(\frac{1}{n_{FL}} + \frac{\delta}{w}\frac{\left(\frac{\delta_w}{\delta}\right)}{\left(\frac{w_w}{w}\right)}\right)} \tag{4.32}$$

$$\sigma_{eff,TP,I} = \frac{C_2 \left(\frac{\delta_w}{\delta}\right)^2 f_w n_{FL}}{\left(\frac{w_w}{w}\right)^2 \left(\frac{1}{n_{FL}} + \frac{\delta}{w}\right)} \tag{4.33}$$

$$\sigma_{eff,TP,A} = \frac{C_3 \left(\frac{\delta_w}{\delta}\right)^2 f_w n_{FL}}{\left(\frac{1}{n_{FL}} + \frac{\delta_w}{w}\right)} \tag{4.34}$$

4.2.4 Porous Media Theory

An insightful comparison between the FN model and an existing model in the literature is accomplished by applying Porous Media Theory to predict in-plane PEM conductivity. In this part of the study, transport in the electrospun PEM fibers is assumed to be analogous to transport in hydrated pores. The equation for effective conductivity is based on an equation commonly used to predict mass diffusivity [34], and is shown in Eq. 4.35.

$$\sigma_{eff,PMT} = \left(\frac{\varepsilon}{\tau^2}\right)\sigma_{bulk} \tag{4.35}$$

Here, σ_{bulk} is the bulk conductivity of a given material, and the term in parentheses is the commonly used porosity-tortuosity factor, where ε is the porosity in typical diffusion studies assumed to be the volume fraction of conducting fiber after swelling, f_w, in this case. The parameter τ is the tortuosity of the structure, which can be estimated with a variety of methods,

including solution of Laplace's equation in a 3-D structure or experimental methods such as mercury intrusion porosimetry.

In this work, in-plane tortuosity is estimated via the simple analytical model for in-plane conductivity presented above and described by Eq. 4.21. However, instead of assuming $l_f = w_w$, effective conductivity predictions from the FN model can be used to determine an average l_f (i.e., an effective length) for the structures by solving Eq. 4.21 for l_f, whereupon a tortuosity estimate can be obtained by dividing the effective l_f by the distance between electrodes, w_w, as shown in Eq. 4.36.

$$\tau_{IP} = \frac{n_{IP}\sigma_f A_{f,w}}{\sigma_{eff}\delta_w w_w} \tag{4.36}$$

Here, n_{IP} is the number of nodes on the boundary face that forms in-plane electrode 1, which is an approximate total number of in-plane conducting pathways in the coupon.

Similarly, thru-plane tortuosity can be estimated by assuming all thru-plane transport paths in the coupon run parallel to each other, and have an effective length, on average, of L_{eff}. The resistance of any one of these paths can be calculated simply by Eq. 4.37, and the effective resistance of the coupon can then be described by Eq. 4.38.

$$R_f = \frac{L_{eff}}{A_{f,w}\sigma_f} \tag{4.37}$$

$$R_{eff} = \frac{R_f}{n_{TP}} \tag{4.38}$$

Inserting these equations into Eq. 4.16, rearranging for L_{eff}, and dividing by the thickness of the membrane yields the thru-plane tortuosity of the coupon, shown by Eq. 4.39.

$$\tau_{TP} = \frac{n_{TP}\sigma_f A_{f,w}}{\sigma_{eff,TP} w_w^2} \tag{4.39}$$

Here, n_{TP} is the number of thru-plane paths in the coupon, which in this case is estimated as the number of boundary nodes in the first layer in the thru-plane resistor network. It is important to note that these definitions of tortuosity, shown by Eqs. 4.36 and 4.39, are largely dependent on the resistive length that is used to define the fins in the resistor network, which are shown in Fig. 4.4, and other assumptions used in developing the FN model such as fibers being represented by 1-D line segments.

4.3 Results and Discussion

4.3.1 Anion Exchange Membranes

The FN model is first used to predict the conductivity behavior of electrospun AEMs. As a test case, the membranes fabricated in Ref. [48] are used for reference. In Ref. [48], the authors first electrospun CMPSF conducting fibers with the inert reinforcing polymer PPSU into a nanofiber composite mat. Both fiber types exhibited an average fiber diameter, before swelling, of roughly 700 nm, which can be seen from Fig. 4.1b. Processing of the electrospun mats into dense membranes was achieved by crosslinking some of the chloromethyl groups in the conducting fibers, softening the PPSU so it would fill the void space, and quaternizing the remaining chloromethyl groups. Their resulting membranes showcased high ion exchange capacity and mechanical strength in addition to high ionic conductivity. Two weight fractions of conducting fiber were fabricated, 55% and 65%, corresponding to conducting fiber volume fractions, before swelling, of 0.59 and 0.68. The membranes showed a high dependency of ionic conductivity on crosslinking degree, where a maximum was achieved at roughly 7%. The effective in-plane

conductivities at volume fractions of 0.59 and 0.68 and 7% crosslinking were 5.7 S/m and 6.5 S/m, respectively. These conductivity values were measured via a Bekktech test cell configuration after water swelling, where gravimetric swelling was found to be 108% and 144% for 0.59 and 0.68 volume fractions, respectively.

The critical input parameters for the FN model are summarized in Table 4.1. Instead of modeling the motion of the collector drum during fiber deposition, random fibers were simply deposited into a coupon, whose dimensions were chosen from preliminary tests to be statistically representative of an entire membrane, i.e. conductivity measurements of coupons had reached an asymptotic value, on average. Initially, the case of $f = 0.68$ was chosen to back-out a fiber conductivity to be used across all trials. For this case, pre-swelling layer thickness was determined to be 890 nm, which resulted in the in-plane conductivity being slightly higher than thru-plane conductivity at that volume fraction. Since the reported membrane morphology is that of ion conducting, hydrophilic nanofibers embedded in an interconnected hydrophobic matrix, the isotropic swelling model is chosen initially [52]. Gravimetric swelling s was set to 1.44 [48], whereupon swelled membrane and fiber dimensions could be computed. The density ratios of the CMPSF fiber (Chloromethylated Udel P-3500 polysulfone) to the PPSU (Radel R-5500 polysulfone) and PPSU to water were provided by Solvay Advanced Polymers, LLC. Fiber conductivity σ_f was then determined as 14.4 S/m in order to result in predicted in-plane conductivities of, on average, 6.5 S/m at $f = 0.68$. Once this value was known, all parameters were fixed except for pre-swelled volume fraction f and gravimetric swelling s, which is dependent on f and determined by fitting a polynomial through the three data points provided in Ref. [48]; that being $s = 0$ at $f = 0$, $s = 1.08$ at $f = 0.59$, and $s = 1.44$ at $f = 0.68$. After

swelling, the swelled layer thickness δ_w is always roughly 10% greater than the swelled fiber diameter, which verifies that conceptually, fibers within a layer will be aligned slightly out of plane in a real membrane. For each volume fraction studied, 10 trials were run to illustrate the spread of conductivity that is measured by the FN model due to randomness in the coupon morphology after fiber deposition. The results are shown in Fig. 4.6, where effective in-plane and thru-plane conductivity is plotted against the volume fraction of conducting fibers after swelling, f_w. In addition, predictions of the EMT model are shown for the two volume fractions studied in Ref. [48]. To consolidate the data, all pre-swelling volume fractions were converted to swelled volume fractions using Eq. 4.5. Thus, the volume fractions of 0.59 and 0.68 that Ref. [48] record have been modified to $f_w = 0.81$ and $f_w = 0.88$, respectively, to take into account swelling.

Parameter	Value
d_f	700 nm
δ	890 nm
n	14
L	20 μm
w	20 μm
σ_f	14.4 S/m
ρ_f/ρ_p	0.87
ρ_p/ρ_w	1.29

Table 4.1. Fiber network model input parameters to predict AEM conductivities [48]. This table is from Ref. [123].

The first thing to note is that the fiber conductivity calculated from the EMT model was 12.3 S/m, in order to match experimental in-plane conductivity at $f = 0.68$ ($f_w = 0.88$). The fiber conductivity calculated from the FN model was 14.4 S/m, which compares reasonably well to the EMT predictions. Experimental measurements for the conductivity of individual nanofibers are difficult to obtain in practice, and are not presented for this material. From Fig. 4.6, the FN model accurately predicts in-plane conductivity of the electrospun AEM at $f = 0.59$ ($f_w = 0.81$). The experimental measurement of 5.7 S/m falls within the range of FN model predictions that occurs due to randomness in the coupon morphology. The EMT prediction for in-plane conductivity at $f_w = 0.81$ is lower than the experiment by roughly 9%; however it reasonably

predicts the trend given the simplifications made in applying the theory, and not accounting for fiber connectivity.

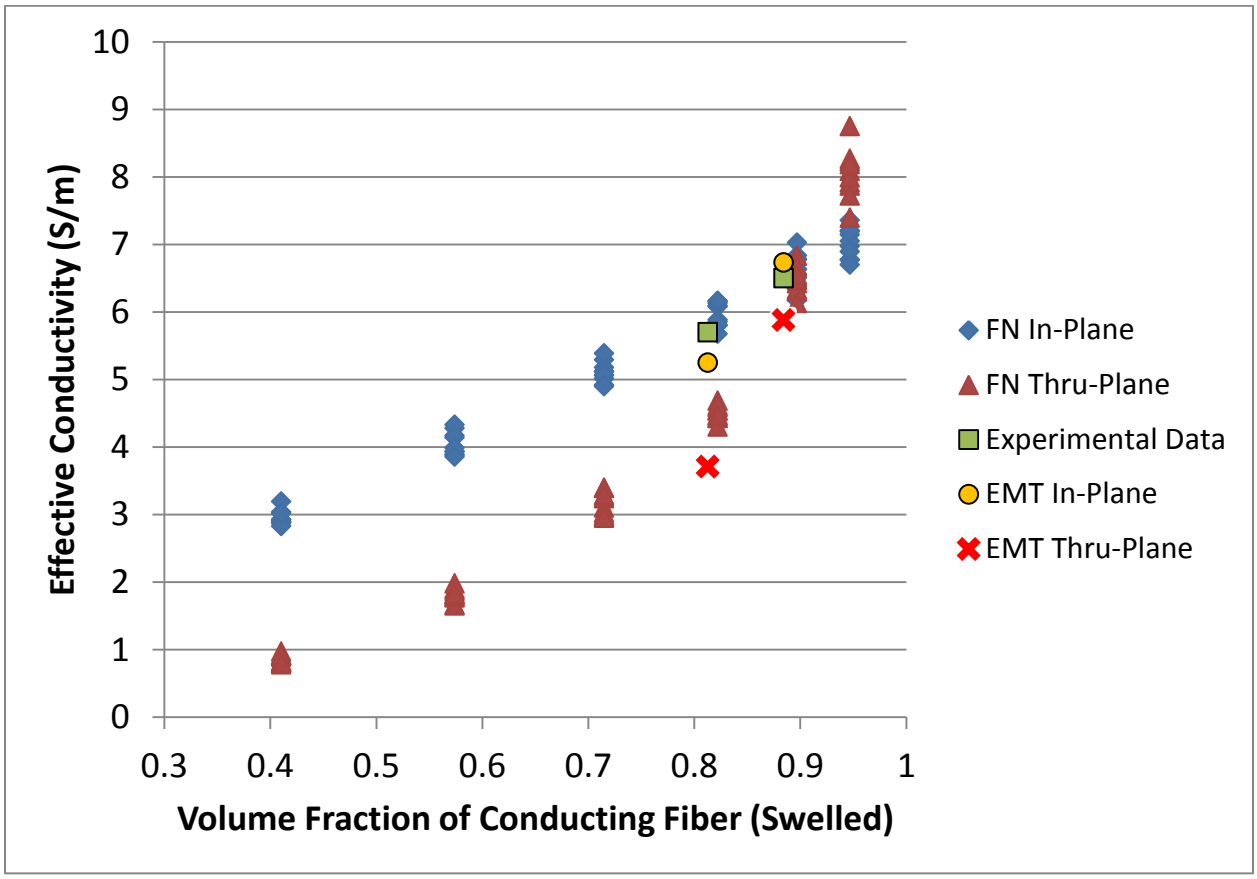

Figure 4.6. Fiber network and EMT model predictions for in-plane and thru-plane ionic conductivity of electrospun AEMs versus swelled volume fraction, and experimental measurements of in-plane conductivity. Experimental data is provided in Ref. [48]. This figure is from Ref. [123].

Extending FN model predictions of in-plane conductivity for the remaining volume fractions yields a linear behavior, which is consistent with the analytical in-plane conductivity model presented in this work. Thru-plane conductivity, however, appears to vary non-linearly with

volume fraction. A general trend is observed that low volume fractions yield thru-plane conductivity that is lower than in-plane conductivity. When the volume fraction is increased past the experimental volume fraction of $f = 0.68$, thru-plane conductivity becomes higher than in-plane conductivity.

The different trends observed with in-plane and thru-plane conductivity will be discussed considering the analytical models presented above. Fig. 4.7 is a plot of in-plane and thru-plane conductivity predictions using both the FN model and the analytical models for both the isotropic and anisotropic swelling cases. In this graph, the FN model data points are averages of 10 trials at each volume fraction, thus representing an average coupon behavior over numerous random network morphologies. The fitting parameters $C_2$and C_3 in Eqs. 4.33 and 4.34 have been chosen to match the FN model data at a swelled volume fraction of 0.88 ($f = 0.68$). The excellent agreement between models indicates that the behavior of conductivity with volume fraction for the different cases can be explained by considering how the inter-connectivity of the fiber network structures change with volume fraction. In the case of in-plane conductivity, beginning with a fiber that spans a coupon between electrodes, adding additional fibers (thus increasing volume fraction) does not decrease the distance ions must travel between electrodes. Instead, additional fibers merely act as additional resistors that are roughly in parallel with one another, and of approximately the same length; resulting in conductivity that varies linearly with volume fraction. The in-plane analytical model captures this behavior, and is equivalent in the case of isotropic and anisotropic swelling.

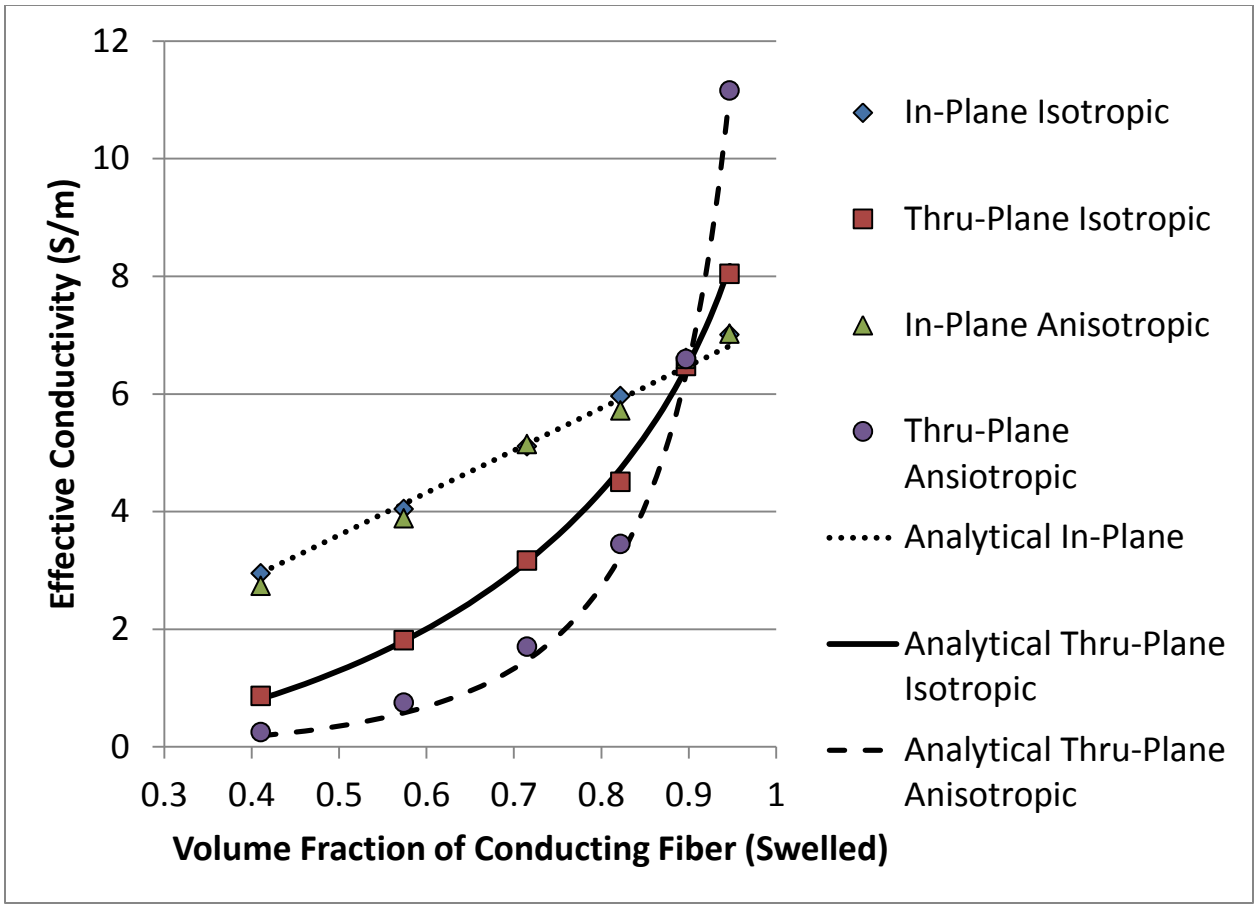

Figure 4.7. A comparison of developed analytical conductivity models for isotropic and anisotropic swelling cases to FN model predictions of in-plane and thru-plane conductivity. The FN model data points are averages over 10 trials at each volume fraction. This figure is from Ref. [123].

Regarding thru-plane conduction, when relatively few fibers exist in a coupon, few thru-plane transport paths exist because of a weak presence of intra and inter-layer contact points. Thus, in a discrete network, ions must travel a significant distance within each layer (in-plane) in addition to between layers to span electrodes. High volume fractions of conducting fiber result in additional contact points and thus additional thru-plane transport pathways (note the non-linear increase in contact points with the number of fibers in a layer). In the analytical model, these

transport pathways are parallel to each other, whereas in the FN model they form a complex interconnected network where the dominant transport direction is along the thru-plane paths. In the discrete FN model, the increased number of transport paths effectively reduces the in-plane distance ions must travel to traverse the network (effectively reducing l_c in Fig. 4.5b). The isotropic and anisotropic swelling models behave differently with volume fraction because an increase in volume fraction (i.e. the number of fibers in a layer in the simple model) yields different swelling behaviors of the membrane. As volume fraction is increased, fiber length does not increase in the anisotropic swelling model; therefore much higher effective conductivities of the entire coupon at high volume fractions result since only the diameter of conducting fibers is increasing. In contrast, the increase in fiber length and slightly lower increase in fiber diameter in the isotropic swelling model yields a more moderate increase in effective conductivity at high volume fractions. For low volume fractions, the low connectivity of the structures is assumed to dominate, where dramatically increased z-direction distances that result from anisotropic swelling are hypothesized to result in lower conductivities than the corresponding isotropic swelling case.

Returning to Fig. 4.6, the spread of conductivities over the range of volume fractions differs for the in-plane and thru-plane cases. The spread of conductivities due to randomness remains relatively constant for the in-plane case, yielding results that span roughly 0.5 S/m. On the other hand, thru-plane conductivity tends to have a larger spread at higher volume fractions, spanning roughly 1.5 S/m at the highest volume fraction, indicating a stronger dependence on specific network morphologies that may arise when randomly depositing more conducting fibers in a volume (i.e. due to node clustering). This spread highlights the discrete nature of the FN model,

which can be contrasted with the averaged approach of EMT and the simple analytical models developed. The FN model is useful for determining the sensitivity of a given fibrous structure to randomness during the fiber deposition process, which could influence design decisions. In addition, the FN model gives an absolute prediction of conductivity, given that fiber conductivity is known a priori, while the analytical models require a fitting parameter and only determine the trend of how conductivity varies with volume fraction.

These results of the model may have implications on how to design electrospun IEMs, since thru-plane is the dominant transport direction in operating cells and the membranes appear to exhibit strong anisotropy in transport behavior. Optimized membranes should thus strike a balance between having high enough volume fractions of conducting fiber for sufficient thru-plane conductivity, while also maintaining good mechanical strength and resistance to mechanical degradation via the presence of a supporting inert matrix. This balance must also consider the effects of membrane swelling, as swelling behavior (e.g., isotropic or anisotropic swelling) will also have a significant impact on both transport and mechanical stability.

4.3.2 Proton Exchange Membranes

To assess the FN model's capabilities to predict PEM conductivity and membrane swelling, and compare predictions to PMT, the electrospun membranes of Ref. [52] are targeted. In this work, the authors dual-spun Nafion and PPSU nanofibers, whereupon processing steps were taken to produce two distinctly different membrane morphologies. The first morphology was produced by allowing the PPSU to soften and fill void space around the Nafion fibers; this approach is similar in principle to that used in Ref. [48]. The second was created by allowing the Nafion

fibers to soften and fill void space around the PPSU fiber network. Since the FN model currently accommodates conducting nanofibers and an insulating matrix, we are interested in modeling the first structure type. A new set of parameters was used to predict conductivities and swelling in the PEM case, which are summarized in Table 4.2. First, the Nafion nanofiber diameter before swelling was determined to be 340 nm on average [52], which is roughly half of the CMPSF fiber diameters used for AEMs above. The coupon dimensions were scaled accordingly, to $\delta = 410\ nm$, $w = 10\ \mu m$, and $L = 10\ \mu m$, while n was fixed at 14 layers. The density ratio for PPSU to water was set to 1.29, and the ratio for Nafion to PPSU was found via the specific gravity of Nafion 212 at 50% RH. The swelling parameter s was determined from the gravimetric swelling measurements provided in Ref. [52] for the range of volume fractions studied. In Ref. [52], membranes with pre-swelling volume fractions ranging from 0.09 to 0.68 were created, and volumetric, gravimetric, and areal swelling was measured for most of these cases. A Nafion fiber conductivity was calculated by matching in-plane conductivity data presented at $f = 0.68$. Once fiber conductivity was found, five trials were run at each volume fraction analyzed with the FN model in order to show the spread attributed to random fiber deposition.

The fiber conductivity for the Nafion nanofibers was determined by the FN model to be 16.75 S/m, which is slightly higher than that predicted for the CMPSF fibers for AEMs. In Ref. [128], Nafion nanofibers of 400 nm diameter were measured as having conductivities of up to 150 S/m at 90% RH. However, this value is seen to be highly dependent on RH and fiber diameter. A fiber conductivity of roughly 20 S/m is achieved when RH is 70% at a fiber diameter of 400 nm, while at 50% RH it is approximately 2 S/m. Though the current fiber network model does not

explicitly model the effects of RH, the FN model predictions are seen to satisfactorily agree with these experimental measurements since the FN predictions fall in the published range. A plot of the in-plane effective ionic conductivity versus pre-swelled volume fraction as predicted by the FN model and that given by Ref. [52] is shown in Fig. 4.8a. A high level of agreement is achieved, with all experimental measurements falling within the spread of the FN model in each case. Fig. 4.8b shows the predicted volumetric and areal swelling in the FN model, assuming completely isotropic coupon swelling, compared to experimental measurements. Volumetric swelling with water is accurately predicted in the FN model, however areal swelling shows some significant discrepancy. This discrepancy arises because the thickness swelling of the membranes studied in Ref. [52] is more prominent than areal swelling, thus the membranes do not swell isotropically. If the FN model were modified to the anisotropic swelling case, areal swelling would be 1.00 (no swelling) for all volume fractions, thus the anisotropic and isotropic swelling models developed in this work bound the behavior of the real membrane.

Parameter	Value
d_f	340 nm
δ	410 nm
n	14
L	10 μm
w	10 μm
σ_f	16.75 S/m
ρ_f/ρ_p	1.52
ρ_f/ρ_p	1.29

Table 4.2. Fiber network model input parameters to predict PEM conductivities [52]. This table is from Ref. [123].

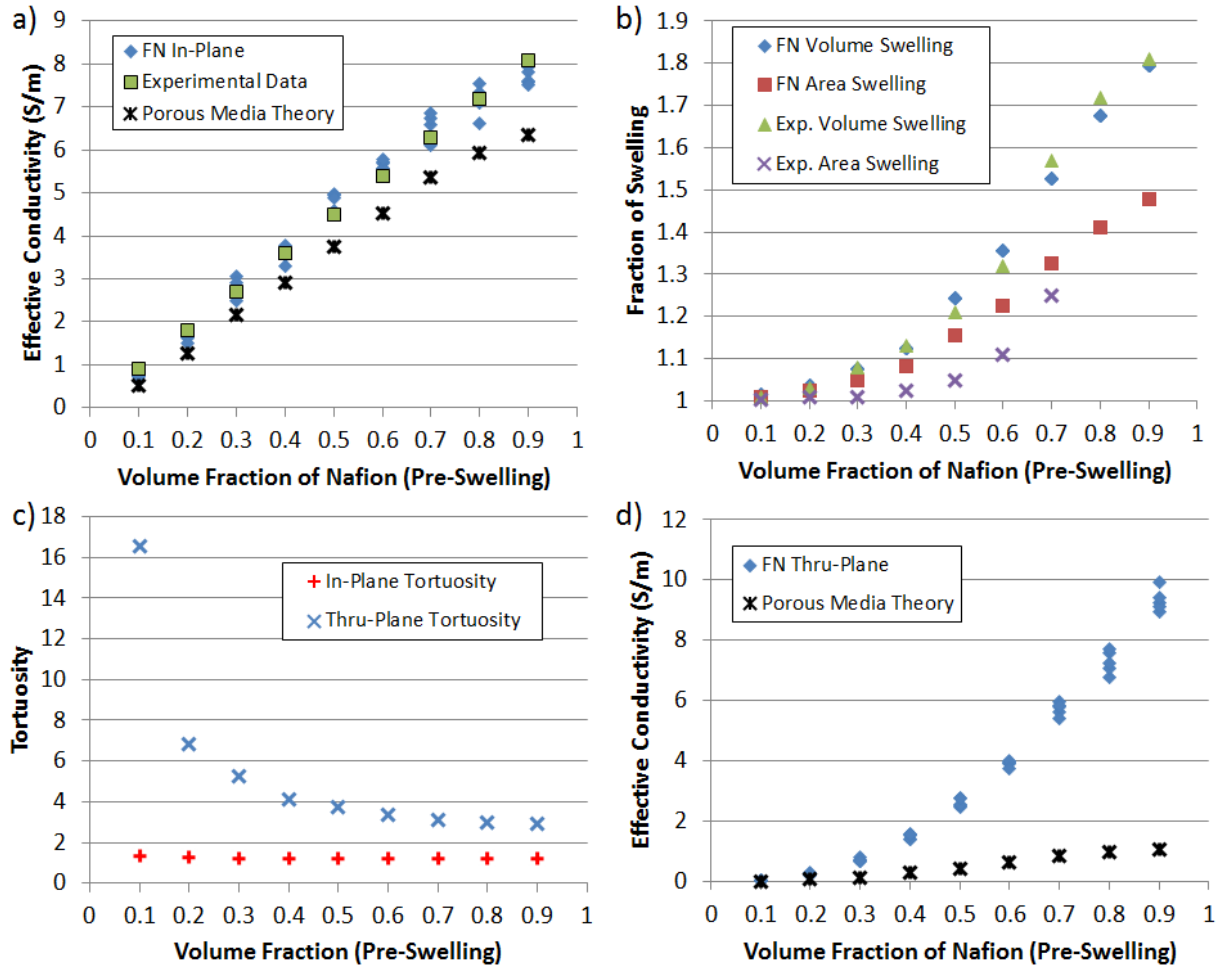

Figure 4.8. a) FN model predictions of in-plane conductivity compared to experimental data and PMT predictions and b) isotropic membrane swelling of electrospun PEMs. Experimental data is provided in Ref. [52]. c) In-plane and thru-plane tortuosity calculated by the FN model and d) FN model thru-plane conductivity compared to PMT calculations. This figure is from Ref. [123].

A final comparison between FN model and PMT conductivity predictions is also shown in Fig. 4.8. For a range of volume fractions, the in-plane and thru-plane tortuosities calculated by the FN model are shown in Fig. 4.8c. In both the in-plane and thru-plane cases, the tortuosity is much higher at low volume fractions due to the relatively low number of fibers in the coupon.

As the volume fraction of conducting fiber is increased, the tortuosity appears to decrease to an asymptotic value. However, it is clear from Fig. 4.8c that the calculated thru-plane tortuosity is much higher than in-plane across all volume fractions. The in-plane tortuosity calculated from the FN model ranges from 1.4 at $f = 0.1$ to 1.2 at $f = 0.9$. Conceptually, the in-plane tortuosity should approach 1 as f approaches 1 if sufficient transport occurs between fibers and the fibers meld into a continuum configuration in an actual membrane; therefore Eq. 4.36 is thought to estimate in-plane tortuosity reasonably well. Thru-plane tortuosity ranges from 16.5 at $f = 0.1$ to 3 at $f = 0.9$. It is thought that these exceptionally high thru-plane tortuosities result because of the basic assumptions used in the FN model. Individual fibers in the FN model are assumed to be 1-D line segments whose orientation dictates the direction of transport. Any 3-D transport within fibers is neglected in this formulation, therefore less tortuous paths that may arise in an actual electrospun membrane due to 3-D transport within fibers is not taken into account here. Therefore, the resistive lengths used to construct the in the in-plane and thru-plane resistor networks may be over-estimating the true length that ions travel in a fiber, especially for high volume fractions where larger contact areas between fibers are more prominent.

The bulk conductivity used with Eq. 4.35 was chosen as that of bulk Nafion 212, which is 9.5 S/m [52]. Based on Fig. 4.8a, Porous Media Theory predictions of in-plane conductivity compare fairly well to the experimental data provided in Ref. [52]. At low volume fractions, these predictions are more accurate than at high volume fractions, while FN model predictions maintain accuracy throughout the range of volume fractions. Fig. 4.8d shows a comparison of thru-plane conductivity predictions using both the FN model and PMT, using the tortuosity values shown in Fig. 4.8c. There is a clear discrepancy between the approaches here, where

PMT predictions are significantly lower than FN model predictions especially for higher volume fractions. In both the in-plane and thru-plane cases, the PMT results are highly dependent on tortuosity, therefore this discrepancy is assumed to be because of the high tortuosity values calculated by the FN model.

It is concluded from this comparison that the existing Porous Media Theory, which uses a volume-averaged approach to describing structure morphology, may be sufficient for predicting electrospun membrane conductivity given that reasonable estimates of ε and τ can be obtained and local information is not required. Tortuosity estimates may be obtained from the FN model, however the assumptions made in developing the model, such as using 1-D line segments to represent fibers and only maintaining contact at singular contact points, may result in over-prediction of tortuosity, especially for the thru-plane case and in general for high volume fractions of conducting fiber. Conversely, the sensitivity of the presented FN model to the electrospun morphologies and specific topological effects of a membrane's network structure make it highly relevant to electrospun membrane design studies. An additional advantage of the FN model is its ability to give an absolute prediction of conductivity without the use of a fitting parameter, given an estimate of layer thickness (based on fiber diameter) and fiber conductivity. When locally sensitive, absolute conductivity predictions are not warranted, quick estimates of conductivity trends for electrospun membranes may be found using the simplified analytical models presented.

4.4 Conclusions

In this chapter, a computational Fiber Network model was developed to predict charge transport in membranes with fibrous network morphologies. This model is predicated on approximating the network morphology that results from the established electrospinning technique, in which conducting nanofibers are deposited and subsequently processed to form highly inter-connected membrane structures with a supporting inert matrix phase. The fiber network morphology is then converted to a resistor network, which is solved via application of an existing electrochemical fin theory that treats each of the conducting fibers as a charge conducting electrochemical fin allowing bulk ionic conduction in the presence of a potential gradient.

The FN model has been shown to accurately predict in-plane hydroxide conductivity in electrospun AEMs and in-plane proton conductivity as well as membrane swelling in electrospun PEMs for a wide range of volume fractions, after calculating fiber conductivity to match experimental data at a single volume fraction. The model is also able to predict thru-plane conductivity for any given structure by implementing thru-plane boundary conditions. It was shown that thru-plane conductivity behaves differently than in-plane conductivity when volume fraction is changed, indicating a potential area of concern for fabricating highly efficient membranes. The trends that arise when different swelling models are used indicate a significant dependence of performance on a membrane's swelling directionality. An extended EMT model and a simplified analytical model have been applied to the fiber network problem to predict in-plane and thru-plane conductivity, which also show agreement with the FN model and can be used to explain the model's conductivity trends. Lastly, an existing Porous Media Theory was used in conjunction with tortuosity values calculated by the FN model to predict PEM

conductivity for a range of structures. Comparisons between the volume-averaged Porous Media approach and models developed specifically for the fiber network morphologies indicate that structural information, such as tortuosity, must be accurately characterized for PMT performance predictions to be acceptable. The analytical models for in-plane and thru-plane conductivity overcome this issue by relating conductivity to more easily estimated fiber network parameters, but require fitting at one data point. The excellent agreement between these models and the FN model predictions highlight these models' applicability in predicting performance trends of electrospun membranes when local information is not desired.

The FN model presented currently relies on simplification of ion transport to strictly a bulk diffusion mechanism; however it may be used with other models to account for more complex transport scenarios. For instance, accompanying theories such as Dusty Fluid model could be used to more accurately predict fiber conductivity in the presence of water and additional transport phenomena. In the case of hydroxide transport in AEMs, predictions from the FN model accounting for fiber network topology and morphology can be combined with models accounting for CO_2 absorption. In light of the assumptions made in developing the FN model, it is seen as a useful tool for the prediction of charge transport in systems with a fiber network microstructure.

Chapter 5: Conclusions

5.1 Key Findings and Contributions

Solid oxide fuel cells and polymer electrolyte membrane fuel cells are two types of electrochemical energy conversion and storage devices that are of interest to meet current and future societal energy demands for portable and stationary power generation. While these devices have different configurations, both rely on the effective transport of numerous species including fuel, electrons and ions in order to function. Significant research is underway to improve these technologies toward commercialization, which includes a better basic understanding of the underlying transport and electrochemical processes that drive their performance. Specifically, there has been a focus on understanding how these processes relate to the structures of materials that constitute fuel cell components on the micro and nano-scales. In this thesis, a combination of methods is used to further understanding of how microstructure can play a role in relevant transport processes. These methods include three-dimensional microstructural imaging, and transport modeling that is sensitive to microstructure encountered in both SOFC and PEM fuel cell materials. These methods are envisioned to be useful for future materials design efforts targeting fuel cell and related energy systems.

Chapter 2 details an imaging technique, synchrotron-based TXM, which is used in this thesis and employed extensively in basic fuel cell research to obtain digital three-dimensional images of a real material's underlying microstructure. Critical to this imaging process is a number of processing steps that must be performed to digital images once they have been obtained via TXM before the images can be used for accurate modeling and simulation.

In Chapter 3, this imaging technique, along with a methodology for artificially generating ideal microstructures, is used to obtain three-dimensional images of representative SOFC electrode microstructures and related materials. A new microstructural transport model based on an existing electrochemical fin theory is developed and utilized to study charge transport in these structures. For validation of the model, existing transport models are used; including a volume-averaged percolation theory and detailed finite element simulations. The electrochemical fin model relies on the discretization of a three-dimensional structure into individual charge conducting transport pathways. These pathways form a transport network structure which may be represented by a network of resistive elements for transport property calculations. The sensitivity of this model to local network topology (i.e. the distribution and location of transport paths) and transport channel morphology (size and shape) enables it to more accurately assess the effects of microstructure on transport than volume-averaged approaches such as percolation theory. Structures with conducting phases near their percolation threshold were shown to have conductivities that could differ an order of magnitude from percolation theory predictions, indicating a strong reliance of microstructural performance on network topology. Furthermore, comparisons with mesh-based finite element models showed that the fin model can give good approximations of conductivity with significantly reduced computational requirements. This was achieved mainly via the fewer elements needed to construct an electrochemical fin network than a finite element model. The proximity of the ECF and FE model predictions indicates that network performance may be more dependent on transport network topology than local amorphous morphology, assuming transport paths are not too constrictive.

In Chapter 4, a host of numerical and analytical transport models were applied to study charge transport in electrospun PEMs. Membranes fabricated by electrospinning showcase distinct fibrous network microstructures which may significantly impact performance. A Fiber Network model is developed here which assumes the electrospun PEM microstructure can be represented by random resistor networks composed of charge conducting electrochemical fins. In-plane and thru-plane ionic conduction is modeled and compared to experimental data for in-plane conductivity of both proton-exchange and anion-exchange membranes. The model and experimental data show excellent agreement in both cases, which lead to the development of a simplified resistor-based analytical model describing conductivity in electrospun membranes. The FN model was also used to calculate in-plane and thru-plane tortuosity of the numerically constructed membranes, allowing a comparison between an existing volume-averaged Porous Media Theory and the fiber network models. The results from these studies indicate a strong dependence of electrospun PEM ionic transport on the underlying fiber networks. Ionic transport is highly dependent on the volume fraction of conducting fiber in the PEM, which dictates the amount of swelling that occurs in the presence of water and the membranes' network topology. Ionic conductivities were also seen to be anisotropic in nature, where thru-plane conductivity follows a significantly different trend than in-plane, highlighting a potential area of concern for newly fabricated membranes.

5.2 Opportunities for Future Work

The modeling studies presented here are relatively new and have mainly been applied in validation studies in this thesis. There are many opportunities going forward to enhance the

accuracy and applicability of these models, and an infinite number of studies that can be run utilizing them.

The electrochemical fin model presented in Chapter 3 relies strongly on the partitioning tool that discretizes the structure into its constituent transport channels. As discussed in Chapter 3, the calculation of surface area and volume by this tool may not be accurately capturing microstructural morphology within material junctions. Additionally, a simple surface area to volume parameter was used to fit electrochemical fin shapes to actual transport channels. Immediate future work could be carried out to improve the accuracy of this procedure, including using shape-fitting algorithms that more accurately account for the transport characteristics of a given channel. Furthermore, in terms of ideal structures, only simple packed sphere structures of varying volume fractions were studied and compared to finite element simulations. It may be of interest to determine the ECF model's sensitivity to varying neck sizes and other axisymmetric particle shapes, as an intermediate validation step. These studies could be used to gain a better insight into how transport is affected by structure using well-controlled case studies, as real microstructures are very complex.

The transport models presented in Chapter 4, including the FN model, are to be combined with other transport models that take into account more complex transport mechanisms of ions in a hydrated PEM. In order to study AEM performance degradation, an existing model accounting for CO_2 absorption may be adjusted based on outputs from the FN model, thus studying the effect of the electrospun membrane morphologies on AEM functionality in adverse operating conditions. Additional studies could be performed to aid in fabrication of electrospun PEMs,

including sensitivity of membranes to various topological characteristics such as fiber clustering (i.e. nanofiber location bias during spinning) or orientation. The use of electrochemical fin theory in the FN model also allows more complicated fiber morphologies to be studied via application of the previously developed analytical solutions, which could include beaded fibers or fibers with distinct curvature. The incorporation of fin shapes aside from cylinders has not yet been studied, and is a possibility for the near future.

Nomenclature

Chapter 1:

a	cross-sectional radius, m
A_1	cross-sectional area at fin entry, m^2
A_2	cross-sectional area at fin exit, m^2
i	local current, A
i_{surf}	surface exchange current, A
L	fin or segment length, m
R	charge transfer resistance, $\Omega\, m^2$
z	axial coordinate, m

Greek

σ	intrinsic ionic conductivity, S/m
φ	potential, V

Chapter 3:

a	cross-sectional radius, m
a_1	cross-sectional radius at fin entry, m
a_2	cross-sectional radius at fin exit, m
$a_{particle}$	cross-sectional radius at channel bulges, m
a_{neck}	cross-sectional radius at channel necks, m
A_c	cross-sectional area, m^2
$A_{c,b}$	cross-sectional area at fin base, m^2
$A_{c,V}$	cross-sectional area of overall volume, m^2
A_1	cross-sectional area at fin entry, m^2
A_2	cross-sectional area at fin exit, m^2
A_s	surface area, m^2

d	diameter, m
i	local current, A
i_{surf}	surface exchange current, A
i_{tot}	total current, A
k	curvature or slope, m^{-1}
L	fin or segment length, m
L_V	length of overall volume, m
n	number fraction
n_c	critical number fraction
R	charge transfer resistance, $\Omega\, m^2$
SQ	sintering quality
V	volume, m^3
z	axial coordinate, m
z_0	axial offset, m
Z	coordination number

Greek

γ	neck size parameter
ε	void fraction
ρ_{ct}	charge transfer resistivity, $\Omega\, m$
ρ_{io}	ionic resistivity, $\Omega\, m$
σ_0	intrinsic ionic conductivity, S/m
σ_{eff}	effective ionic conductivity, S/m
$\bar{\sigma}_{eff}$	normalized effective ionic conductivity
φ	potential, V
φ_b	potential at fin base, V
φ^*	dimensionless potential

$\Delta\varphi_V$	potential difference across volume, V

Chapter 4:

A	Cross-sectional area, m^2
D	Distance between electrodes, m^2
d	Diameter, m
f	Volume fraction of conducting fiber
I	Total current, A
L	Coupon length, m
l	Individual length of a fiber, m
l_c	Distance between neighboring contact points, m
L_f	Total length of fiber in a coupon, m
n	Number of layers in a coupon
n_{FL}	Number of fibers in a layer
n_{IP}	Number of in-plane conducting paths
n_{TP}	Number of thru-plane conducting paths
R	Resistance, Ω
SF	Swelling scale factor
T	Total coupon thickness, m
V	Volume, m^3
w	Coupon width, m

Greek

ΔV	Potential difference, V
δ	Layer thickness, m
ε	Porosity
ρ	Density, g/m^3
σ	Ionic conductivity, S/m
τ	Tortuosity

Subscripts

A	Anisotropic swelling
$bulk$	Bulk property
eff	Effective property
f	Fiber
I	Isotropic swelling
IP	In-plane
L	Layer
P	Supporting matrix
t	Property of total coupon
TP	Thru-plane
w	After swelling

Bibliography

1. J. Larminie and A. Dicks, *Fuel Cell Systems Explained*, 2nd ed., Wiley, New York, 2003.

2. S. C. Singhal and K. Kendall, Eds., *High Temperature Solid Oxide Fuel Cells: Fundamentals, Design and Applications*, Elsevier, 2003.

3. B. Kenney, M. Valdmanis, C. Baker, J. G. Pharoah, and K. Karan, Computation of TPB Length, Surface Area and Pore Size from Numerical Reconstruction of Composite Solid Oxide Fuel Cell Electrodes, *J. Power Sources*, Vol. 189, pp. 1051–1059, 2009.

4. M. B. DeGostin, A. Nakajo, B. N. Cassenti, A. A. Peracchio, G. J. Nelson, and W. K. S. Chiu, Geometric Sensitivity of Electrochemical Fin Shape on Three Dimensional Microstructure Network Conductivity Analysis, *J. Power Sources*, Vol. 291, pp. 181–194, 2015.

5. J. R. Wilson, W. Kobsiriphat, R. Mendoza, H.-Y. Chen, J. M. Hiller, D. J. Miller, K. Thornton, P. W. Voorhees, S. B. Adler, and S. A. Barnett, Three-Dimensional Reconstruction of a Solid-Oxide Fuel-Cell Anode, *Nat. Mater.*, Vol. 5, no. July, pp. 541–544, 2006.

6. V. Dusastre and J. A. Kilner, Optimisation of Composite Cathodes for Intermediate Temperature SOFC Applications, *Solid State Ionics*, Vol. 126, pp. 163–174, 1999.

7. A. V. Virkar, J. Chen, C. W. Tanner, and J. W. Kim, Role of Electrode Microstructure on Activation and Concentration Polarizations in Solid Oxide Fuel Cells, *Solid State Ionics*, Vol. 131, no. 1, pp. 189–198, 2000.

8. K. L. Reifsnider, W. K. S. Chiu, K. S. Brinkman, Y. Du, A. Nakajo, F. Rabbi, and Q. Liu, Multiphysics Design and Development of Heterogeneous Functional Materials for Renewable Energy Devices: The HeteroFoaM Story, *J. Electrochem. Soc.*, Vol. 160, no. 4, pp. F470–F481, 2013.

9. T. D. Myles, A. A. Peracchio, and W. K. S. Chiu, Extension of Anisotropic Effective Medium Theory to Account for an Arbitrary Number of Inclusion Types, *J. Appl. Phys.*, Vol. 117, p. 025101, 2015.

10. P. Costamagna, P. Costa, and V. Antonucci, Micro-Modelling of Solid Oxide Fuel Cell Electrodes, *Electrochim. Acta*, Vol. 43, no. 97, pp. 375–394, 1998.

11. Y. Zhang, Y. Wang, Y. Wang, F. Chen, and C. Xia, Random-Packing Model for Solid Oxide Fuel Cell Electrodes with Particle Size Distributions, *J. Power Sources*, Vol. 196, no. 4, pp. 1983–1991, 2011.

12. H. Zhu and R. J. Kee, Modeling Distributed Charge-Transfer Processes in SOFC Membrane Electrode Assemblies, *J. Electrochem. Soc.*, Vol. 155, p. B715, 2008.

13. S. H. Chan, X. J. Chen, and K. A. Khor, Cathode Micromodel of Solid Oxide Fuel Cell, *J. Electrochem. Soc.*, Vol. 151, p. A164, 2004.

14. D. Chen, W. Bi, W. Kong, and Z. Lin, Combined Micro-Scale and Macro-Scale Modeling of the Composite Electrode of a Solid Oxide Fuel Cell, *J. Power Sources*, Vol. 195, no. 19, pp. 6598–6610, 2010.

15. D. Chen, Z. Lin, H. Zhu, and R. J. Kee, Percolation Theory to Predict Effective Properties of Solid Oxide Fuel-Cell Composite Electrodes, *J. Power Sources*, Vol. 191, pp. 240–252, 2009.

16. A. Bertei, H. W. Choi, J. G. Pharoah, and C. Nicolella, Percolating Behavior of Sintered Random Packings of Spheres, *Powder Technol.*, Vol. 231, pp. 44–53, 2012.

17. K. Rhazaoui, Q. Cai, C. S. Adjiman, and N. P. Brandon, Towards the 3D Modeling of the Effective Conductivity of Solid Oxide Fuel Cell Electrodes: I. Model Development, *Chem. Eng. Sci.*, Vol. 99, pp. 161–170, 2013.

18. J. Ott, B. Volker, Y. Gan, R. McMeeking, and M. Kamlah, A Micromechanical Model for Effective Conductivity in Granular Electrode Structures, *Acta Mech. Sin.*, Vol. 29, pp. 682–698, 2013.

19. S. Sunde, Calculation of Conductivity and Polarization Resistance of Composite SOFC Electrodes from Random Resistor Networks, *J. Electrochem. Soc.*, Vol. 142, no. 4, p. L50, 1995.

20. S. Sunde, Monte Carlo Simulations of Polarization Resistance of Composite Electrodes for Solid Oxide Fuel Cells, *J. Electrochem. Soc.*, Vol. 143, no. 6, p. 1930, 1996.

21. J. Abel, Correlated Resistor Network Study of Porous Solid Oxide Fuel Cell Anodes, *J. Electrochem. Soc.*, Vol. 144, no. March, p. 4253, 1997.

22. L. C. R. Schneider, C. L. Martin, Y. Bultel, D. Bouvard, and E. Siebert, Discrete Modelling of the Electrochemical Performance of SOFC Electrodes, *Electrochim. Acta*, Vol. 52, pp. 314–324, 2006.

23. A. Abbaspour, J.-L. Luo, and K. Nandakumar, Three-Dimensional Random Resistor-Network Model for Solid Oxide Fuel Cell Composite Electrodes, *Electrochim. Acta*, Vol. 55, no. 12, pp. 3944–3950, 2010.

24. A. P. Cocco, G. J. Nelson, W. M. Harris, A. Nakajo, T. D. Myles, A. M. Kiss, J. J. Lombardo, and W. K. S. Chiu, Three-Dimensional Microstructural Imaging Methods for Energy Materials, *Phys. Chem. Chem. Phys.*, Vol. 15, no. 39, pp. 16377–407, 2013.

25. A. Bertei, B. Nucci, and C. Nicolella, Microstructural Modeling for Prediction of Transport Properties and Electrochemical Performance in SOFC Composite Electrodes, *Chem. Eng. Sci.*, Vol. 101, pp. 175–190, 2013.

26. C. C. Chueh, A. Bertei, J. G. Pharoah, and C. Nicolella, Effective Conductivity in Random Porous Media with Convex and Non-Convex Porosity, *Int. J. Heat Mass Transf.*, Vol. 71, pp. 183–188, 2014.

27. H.-W. Choi, A. Berson, J. G. Pharoah, and S. B. Beale, Effective Transport Properties of the Porous Electrodes in Solid Oxide Fuel Cells, *Proc. Inst. Mech. Eng. Part A J. Power Energy*, Vol. 225, pp. 183–197, 2011.

28. N. S. K. Gunda, H. W. Choi, A. Berson, B. Kenney, K. Karan, J. G. Pharoah, and S. K. Mitra, Focused Ion Beam-Scanning Electron Microscopy on Solid-Oxide Fuel-Cell Electrode: Image Analysis and Computing Effective Transport Properties, *J. Power Sources*, Vol. 196, no. 7, pp. 3592–3603, 2011.

29. A. Çeçen, E. A. Wargo, A. C. Hanna, D. M. Turner, S. R. Kalidindi, and E. C. Kumbur, 3-D Microstructure Analysis of Fuel Cell Materials: Spatial Distributions of Tortuosity, Void Size and Diffusivity, *J. Electrochem. Soc.*, Vol. 159, no. 3, p. B299, 2012.

30. Q. Cai, C. S. Adjiman, and N. P. Brandon, Modelling the 3D Microstructure and Performance of Solid Oxide Fuel Cell Electrodes: Computational Parameters, *Electrochim. Acta*, Vol. 56, no. 16, pp. 5804–5814, 2011.

31. J. Laurencin, R. Quey, G. Delette, H. Suhonen, P. Cloetens, and P. Bleuet, Characterisation of Solid Oxide Fuel Cell Ni-8YSZ Substrate by Synchrotron X-Ray Nano-Tomography: From 3D Reconstruction to Microstructure Quantification, *J. Power Sources*, Vol. 198, pp. 182–189, 2012.

32. J. Sanyal, G. M. Goldin, H. Zhu, and R. J. Kee, A Particle-Based Model for Predicting the Effective Conductivities of Composite Electrodes, *J. Power Sources*, Vol. 195, no. 19, pp. 6671–6679, 2010.

33. L. Holzer, B. Iwanschitz, T. Hocker, L. Keller, O. Pecho, G. Sartoris, P. Gasser, and B. Muench, Redox Cycling of Ni-YSZ Anodes for Solid Oxide Fuel Cells: Influence of Tortuosity, Constriction and Percolation Factors on the Effective Transport Properties, *J. Power Sources*, Vol. 242, pp. 179–194, 2013.

34. A. S. Joshi, K. N. Grew, J. R. Izzo, A. A. Peracchio, and W. K. S. Chiu, Lattice Boltzmann Modeling of Three-Dimensional, Multicomponent Mass Diffusion in a Solid Oxide Fuel Cell Anode, *J. Fuel Cell Sci. Technol.*, Vol. 7, p. 011006, 2010.

35. Y. Suzue, N. Shikazono, and N. Kasagi, Micro Modeling of Solid Oxide Fuel Cell Anode Based on Stochastic Reconstruction, *J. Power Sources*, Vol. 184, pp. 52–59, 2008.

36. N. Shikazono, D. Kanno, K. Matsuzaki, H. Teshima, S. Sumino, and N. Kasagi, Numerical Assessment of SOFC Anode Polarization Based on Three-Dimensional Model Microstructure Reconstructed from FIB-SEM Images, *J. Electrochem. Soc.*, Vol. 157, pp. B665–B672, 2010.

37. K. Matsuzaki, N. Shikazono, and N. Kasagi, Three-Dimensional Numerical Analysis of Mixed Ionic and Electronic Conducting Cathode Reconstructed by Focused Ion Beam Scanning Electron Microscope, *J. Power Sources*, Vol. 196, no. 6, pp. 3073–3082, 2011.

38. M. Kishimoto, H. Iwai, K. Miyawaki, M. Saito, and H. Yoshida, Improvement of the Sub-Grid-Scale Model Designed for 3D Numerical Simulation of Solid Oxide Fuel Cell Electrodes Using an Adaptive Power Index, *J. Power Sources*, Vol. 223, pp. 268–276, 2013.

39. K. D. Kreuer, Ion Conducting Membranes for Fuel Cells and Other Electrochemical Devices, *Chem. Mater.*, Vol. 26, pp. 361–380, 2014.

40. Y. Zhao, H. Yu, F. Xie, Y. Liu, Z. Shao, and B. Yi, High Durability and Hydroxide Ion Conducting Pore-Filled Anion Exchange Membranes for Alkaline Fuel Cell Applications, *J. Power Sources*, Vol. 269, pp. 1–6, 2014.

41. Y. C. Cao, X. Wang, and K. Scott, The Synthesis and Characteristic of an Anion Conductive Polymer Membrane for Alkaline Anion Exchange Fuel Cells, *J. Power Sources*, Vol. 201, pp. 226–230, 2012.

42. K. Matsumoto, T. Fujigaya, H. Yanagi, and N. Nakashima, Very High Performance Alkali Anion-Exchange Membrane Fuel Cells, *Adv. Funct. Mater.*, Vol. 21, no. 6, pp. 1089–1094, 2011.

43. K. N. Grew, X. Ren, and D. Chu, Effects of Temperature and Carbon Dioxide on Anion Exchange Membrane Conductivity, *Electrochem. Solid-State Lett.*, Vol. 14, no. 12, p. B127, 2011.

44. K. Borka and P. Ekdunge, Oxygen and Hydrogen Permeation in Bulk and Recast Films, *J. Appl. Electrochem.*, Vol. 27, pp. 117–123, 1997.

45. B. B. Jeffrey A. Kolde and W. L. Gore, Advanced Composite Polymer Electrolyte Fuel Cell Membranes, *Proc. First Int. Symp. Prot. Conduct. Membr. Fuel Cells , Electrochem. Soc. Inc.*, Vol. 95–23, pp. 193–201, 1995.

46. B. Smitha, S. Sridhar, and a. a. Khan, Solid Polymer Electrolyte Membranes for Fuel Cell Applications - A Review, *J. Memb. Sci.*, Vol. 259, no. 1–2, pp. 10–26, 2005.

47. G. Merle, M. Wessling, and K. Nijmeijer, Anion Exchange Membranes for Alkaline Fuel Cells: A Review, *J. Memb. Sci.*, Vol. 377, pp. 1–35, 2011.

48. A. M. Park, F. E. Turley, R. J. Wycisk, and P. N. Pintauro, Electrospun and Cross-Linked Nanofiber Composite Anion Exchange Membranes, *Macromolecules*, Vol. 47, pp. 227–235, 2014.

49. J. R. Varcoe, P. Atanassov, D. R. Dekel, A. M. Herring, M. A. Hickner, P. A. Kohl, A. R. Kucernak, W. E. Mustain, K. Nijmeijer, K. Scott, T. Xu, and L. Zhuang, Anion-Exchange Membranes in Electrochemical Energy Systems, *Energy Environ. Sci.*, Vol. 7, pp. 3135–3191, 2014.

50. W. Zhang and P. N. Pintauro, High-Performance Nanofiber Fuel Cell Electrodes, *ChemSusChem*, Vol. 4, pp. 1753–1757, 2011.

51. J. Choi, K. M. Lee, R. Wycisk, P. N. Pintauro, and P. T. Mather, Nanofiber Composite Membranes with Low Equivalent Weight Perfluorosulfonic Acid Polymers, *J. Mater. Chem.*, Vol. 20, p. 6282, 2010.

52. J. B. Ballengee and P. N. Pintauro, Composite Fuel Cell Membranes from Dual-Nanofiber Electrospun Mats, *Macromolecules*, Vol. 44, pp. 7307–7314, 2011.

53. H.-L. Lin, S.-H. Wang, C.-K. Chiu, T. L. Yu, L.-C. Chen, C.-C. Huang, T.-H. Cheng, and J.-M. Lin, Preparation of Nafion/poly(vinyl Alcohol) Electro-Spun Fiber Composite Membranes for Direct Methanol Fuel Cells, *J. Memb. Sci.*, Vol. 365, no. 1–2, pp. 114–122, 2010.

54. D. Li and Y. Xia, Electrospinning of Nanofibers: Reinventing the Wheel?, *Adv. Mater.*, Vol. 16, no. 14, pp. 1151–1170, 2004.

55. H. Zhang and P. K. Shen, Advances in the High Performance Polymer Electrolyte Membranes for Fuel Cells, *Chem. Soc. Rev.*, Vol. 41, p. 2382, 2012.

56. T. Chakrabarty, M. Kumar, K. P. Rajesh, V. K. Shahi, and T. S. Natarajan, Nano-Fibrous Sulfonated Poly(ether Ether Ketone) Membrane for Selective Electro-Transport of Ions, *Sep. Purif. Technol.*, Vol. 75, no. 2, pp. 174–182, 2010.

57. J. B. Ballengee and P. N. Pintauro, Morphological Control of Electrospun Nafion Nanofiber Mats, *J. Electrochem. Soc.*, Vol. 158, no. 5, p. B568, 2011.

58. H. Chen, J. D. Snyder, and Y. A. Elabd, Electrospinning and Solution Properties of Nafion and Poly (acrylic Acid), *Macromolecules*, Vol. 41, pp. 128–135, 2008.

59. S. V Fridrikh, J. H. Yu, M. P. Brenner, and G. C. Rutledge, Controlling the Fiber Diameter during Electrospinning, *Phys. Rev. Lett.*, Vol. 90, p. 144502, 2003.

60. A. Z. Weber and J. Newman, Modeling Transport in Polymer-Electrolyte Fuel Cells, *Chem. Rev.*, Vol. 104, no. 10, pp. 4679–4726, 2004.

61. A. M. Kiss, T. D. Myles, K. N. Grew, A. A. Peracchio, G. J. Nelson, and W. K. S. Chiu, Calculating Hydroxide Conductivity in Alkaline Anion Exchange Membranes, *ECS Trans.*, Vol. 41, no. 1, pp. 1827–1835, 2011.

62. T. Thampan, S. Malhotra, H. Tang, and R. Datta, Modeling of Conductive Transport in Proton-Exchange Membranes for Fuel Cells, *J. Electrochem. Soc.*, Vol. 147, no. 9, p. 3242, 2000.

63. K. N. Grew, D. Chu, and W. K. S. Chiu, Ionic Equilibrium and Transport in the Alkaline Anion Exchange Membrane, *J. Electrochem. Soc.*, Vol. 157, p. B1024, 2010.

64. K. N. Grew and W. K. S. Chiu, A Dusty Fluid Model for Predicting Hydroxyl Anion Conductivity in Alkaline Anion Exchange Membranes, *J. Electrochem. Soc.*, Vol. 157, p. B327, 2010.

65. M. R. Hibbs, M. A. Hickner, T. M. Alam, S. K. McIntyre, C. H. Fujimoto, and C. J. Cornelius, Transport Properties of Hydroxide and Proton Conducting Membranes, *Chem. Mater.*, Vol. 20, no. 3, pp. 2566–2573, 2008.

66. A. Biyikoglu, Review of Proton Exchange Membrane Fuel Cell Models, *Int. J. Hydrogen Energy*, Vol. 30, pp. 1181–1212, 2005.

67. T. E. Springer, T. A. Zawodzinski, and S. Gottesfeld, Polymer Electrolyte Fuel Cell Model, *J. Electrochem. Soc.*, Vol. 138, no. 8, pp. 2334–2342, 1991.

68. D. Cheddie and N. Munroe, Review and Comparison of Approaches to Proton Exchange Membrane Fuel Cell Modeling, *J. Power Sources*, Vol. 147, pp. 72–84, 2005.

69. E. Spohr, P. Commer, and A. A. Kornyshev, Enhancing Proton Mobility in Polymer Electrolyte Membranes : Lessons from Molecular Dynamics Simulations Enhancing Proton Mobility in Polymer Electrolyte Membranes : Lessons from Molecular Dynamics Simulations, *Structure*, pp. 10560–10569, 2002.

70. R. Jinnouchi and K. Okazaki, Molecular Dynamics Study of Transport Phenomena in Perfluorosulfonate Ionomer Membranes for Polymer Electrolyte Fuel Cells, *J. Electrochem. Soc.*, Vol. 150, no. 1, p. E66, 2003.

71. P. K. Das, X. Li, and Z. S. Liu, Effective Transport Coefficients in PEM Fuel Cell Catalyst and Gas Diffusion Layers: Beyond Bruggeman Approximation, *Appl. Energy*, Vol. 87, no. 9, pp. 2785–2796, 2010.

72. D. Song, Q. Wang, Z. Liu, T. Navessin, M. Eikerling, and S. Holdcroft, Numerical Optimization Study of the Catalyst Layer of PEM Fuel Cell Cathode, *J. Power Sources*, Vol. 126, no. 1–2, pp. 104–111, 2004.

73. T. D. Myles, A. A. Peracchio, U. Pasaogullari, and W. K. S. Chiu, Application of an Effective Medium Formulation to Account for Transport Due to Fiber and Web-like Inclusions in Gas Diffusion Layers, *J. Electrochem. Soc.*, Vol. 162, no. 7, pp. F645–F650, 2015.

74. T. D. Myles, A. A. Peracchio, and W. K. S. Chiu, Effect of Orientation Anisotropy on Calculating Effective Electrical Conductivities, *J. Appl. Phys.*, Vol. 115, no. 20, p. 203503, 2014.

75. S. D. Druger, A. Nitzan, and M. A. Ratner, Dynamic Bond Percolation Theory: A Microscopic Model for Diffusion in Dynamically Disordered Systems. I. Definition and One-Dimensional Case, *J. Chem. Phys.*, Vol. 79, no. 6, p. 3133, 1983.

76. Q. Wang, M. Eikerling, D. Song, Z. Liu, T. Navessin, Z. Xie, and S. Holdcroft, Functionally Graded Cathode Catalyst Layers for Polymer Electrolyte Fuel Cells, *J. Electrochem. Soc.*, Vol. 151, no. 7, p. A950, 2004.

77. E. Passalacqua, F. Lufrano, G. Squadrito, a. Patti, and L. Giorgi, Nafion Content in the Catalyst Layer of Polymer Electrolyte Fuel Cells: Effects on Structure and Performance, *Electrochim. Acta*, Vol. 46, no. 6, pp. 799–805, 2001.

78. J. R. Izzo, A. S. Joshi, K. N. Grew, W. K. S. Chiu, A. Tkachuk, S. H. Wang, and W. Yun, Nondestructive Reconstruction and Analysis of SOFC Anodes Using X-Ray Computed Tomography at Sub-50 Nm Resolution, *J. Electrochem. Soc.*, Vol. 155, pp. B504–B508, 2008.

79. G. J. Nelson, W. M. Harris, J. J. Lombardo, J. R. Izzo, W. K. S. Chiu, P. Tanasini, M. Cantoni, J. Van Herle, C. Comninellis, J. C. Andrews, Y. Liu, P. Pianetta, and Y. S. Chu, Comparison of SOFC Cathode Microstructure Quantified Using X-Ray Nanotomography and Focused Ion Beam-Scanning Electron Microscopy, *Electrochem. Commun.*, Vol. 13, no. 6, pp. 586–589, 2011.

80. J. S. Cronin, Y. K. Chen-Wiegart, J. Wang, and S. A. Barnett, Three-Dimensional Reconstruction and Analysis of an Entire Solid Oxide Fuel Cell by Full-Field Transmission X-Ray Microscopy, *J. Power Sources*, Vol. 233, pp. 174–179, 2013.

81. Y. K. Chen-Wiegart, J. S. Cronin, Q. Yuan, K. J. Yakal-Kremski, S. A. Barnett, and J. Wang, 3D Non-Destructive Morphological Analysis of a Solid Oxide Fuel Cell Anode Using Full-Field X-Ray Nano-Tomography, *J. Power Sources*, Vol. 218, pp. 348–351, 2012.

82. K. N. Grew, Y. S. Chu, J. Yi, A. A. Peracchio, J. R. Izzo, Y. Hwu, F. De Carlo, and W. K. S. Chiu, Nondestructive Nanoscale 3D Elemental Mapping and Analysis of a Solid Oxide Fuel Cell Anode, *J. Electrochem. Soc.*, Vol. 157, pp. B783–B792, 2010.

83. G. J. Nelson, A. A. Peracchio, and W. K. S. Chiu, Analytical Investigations of Varying Cross Section Microstructures on Charge Transfer in Solid Oxide Fuel Cell Electrodes, *J. Power Sources*, Vol. 196, no. 10, pp. 4695–4704, 2011.

84. C. W. Tanner, K.-Z. Fung, and A. V. Virkar, The Effect of Porous Composite Electrode Structure on Solid Oxide Fuel Cell Performance: I. Theoretical Analysis, *J. Electrochem. Soc.*, Vol. 144, no. 1, pp. 21–30, 1997.

85. G. J. Nelson, B. N. Cassenti, A. A. Peracchio, and W. K. S. Chiu, Two-Dimensional Charge Transfer and Space Charge Effects in Extended Surface Solid Oxide Fuel Cell Electrodes, *J. Power Sources*, Vol. 205, pp. 48–56, 2012.

86. S. B. Adler, Electrode Kinetics of Porous Mixed-Conducting Oxygen Electrodes, *J. Electrochem. Soc.*, Vol. 143, no. 11, p. 3554, 1996.

87. B. N. Cassenti, G. J. Nelson, M. B. DeGostin, A. A. Peracchio, and W. K. S. Chiu, Analytical Solutions for Extended Surface Electrochemical Fin Models, *J. Power Sources*, Vol. 265, pp. 282–290, 2014.

88. M. B. DeGostin, A. P. Cocco, and W. K. S. Chiu, Synchrotron-Based Transmission X-Ray Microscopy: A Tool for Three-Dimensional Spectroscopic Imaging and Numerical Simulations, *Submitted*, 2015.

89. G. J. Nelson, W. M. Harris, J. R. Izzo, K. N. Grew, W. K. S. Chiu, Y. S. Chu, J. Yi, J. C. Andrews, Y. Liu, and P. Pianetta, Three-Dimensional Mapping of Nickel Oxidation States Using Full Field X-Ray Absorption near Edge Structure Nanotomography, *Appl. Phys. Lett.*, Vol. 98, pp. 10–13, 2011.

90. Y.-T. Chen, T.-N. Lo, Y. S. Chu, J. Yi, C.-J. Liu, J.-Y. Wang, C.-L. Wang, C.-W. Chiu, T.-E. Hua, Y. Hwu, Q. Shen, G.-C. Yin, K. S. Liang, H.-M. Lin, J. H. Je, and G. Margaritondo, Full-Field Hard X-Ray Microscopy below 30 nm: A Challenging Nanofabrication Achievement, *Nanotechnology*, Vol. 19, no. 39, pp. 395302–1–395302–5, 2008.

91. J. Vila-Comamala, Y. Pan, J. J. Lombardo, W. M. Harris, W. K. S. Chiu, C. David, and Y. Wang, Zone-Doubled Fresnel Zone Plates for High-Resolution Hard X-Ray Full-Field Transmission Microscopy, *J. Synchrotron Radiat.*, Vol. 19, pp. 705–709, 2012.

92. W. M. Harris, G. J. Nelson, A. M. Kiss, J. R. Izzo, Jr., Y. Liu, M. Liu, S. Wang, Y. S. Chu, and W. K. S. Chiu, Nondestructive Volumetric 3-D Chemical Mapping of Nickel-Sulfur Compounds at the Nanoscale, *Nanoscale*, Vol. 4, no. 5, pp. 1557–1560, 2012.

93. J. J. Lombardo, R. A. Ristau, W. M. Harris, and W. K. S. Chiu, Focused Ion Beam Preparation of Samples for X-Ray Nanotomography, *J. Synchrotron Radiat.*, Vol. 19, no. Pt 5, pp. 789–796, 2012.

94. A. C. Kak and M. Slaney, *Principles of Computerized Tomographic Imaging*, Society of Industrial and Applied Mathematics, 2001.

95. E. X. Miqueles and A. R. De Pierro, Iterative Reconstruction in X-Ray Fluorescence Tomography Based on Radon Inversion, *IEEE Trans. Med. Imaging*, Vol. 30, no. 2, pp. 438–50, 2011.

96. G.-F. Rust and J. Weigelt, X-Ray Fluorescent Computer Tomography with Synchrotron Radiation, *IEEE Trans. Nucl. Sci.*, Vol. 45, no. 1, pp. 75–88, 1998.

97. A. Markoe, *Analytic Tomography*, Cambridge Univ Press, 2006.

98. D. Gürsoy, F. De Carlo, X. Xiao, and C. Jacobsen, TomoPy: A Framework for the Analysis of Synchrotron Tomographic Data, *J. Synchrotron Radiat.*, Vol. 21, no. 5, pp. 1–6, 2014.

99. F. Marone and M. Stampanoni, Regridding Reconstruction Algorithm for Real-Time Tomographic Imaging, *J. Synchrotron Radiat.*, Vol. 19, no. 6, pp. 1029–1037, 2012.

100. H. Andrä, N. Combaret, J. Dvorkin, E. Glatt, J. Han, M. Kabel, Y. Keehm, F. Krzikalla, M. Lee, C. Madonna, M. Marsh, T. Mukerji, E. H. Saenger, R. Sain, N. Saxena, S. Ricker, A. Wiegmann, and X. Zhan, Digital Rock Physics Benchmarks-Part I: Imaging and Segmentation, *Comput. Geosci.*, Vol. 50, pp. 25–32, 2013.

101. Q. Wu, F. A. Merchant, K. R. Castleman, and C. Kenneth R., *Microscope Image Processing*, 2008.

102. G. J. Nelson, A. Nakajo, B. N. Cassenti, M. B. DeGostin, K. R. Bagshaw, A. A. Peracchio, G. Xiao, S. Wang, F. Chen, and W. K. S. Chiu, A Rapid Analytical Assessment Tool for Three Dimensional Electrode Microstructural Networks with Geometric Sensitivity, *J. Power Sources*, Vol. 246, pp. 322–334, 2014.

103. E. Maire, P. Colombo, J. Adrien, L. Babout, and L. Biasetto, Characterization of the Morphology of Cellular Ceramics by 3D Image Processing of X-Ray Tomography, *J. Eur. Ceram. Soc.*, Vol. 27, pp. 1973–1981, 2007.

104. H. Bale, M. Blacklock, M. R. Begley, D. B. Marshall, B. N. Cox, and R. O. Ritchie, Characterizing Three-Dimensional Textile Ceramic Composites Using Synchrotron X-Ray Micro-Computed-Tomography, *J. Am. Ceram. Soc.*, Vol. 95, pp. 392–402, 2012.

105. A. Kaestner, E. Lehmann, and M. Stampanoni, Imaging and Image Processing in Porous Media Research, *Adv. Water Resour.*, Vol. 31, pp. 1174–1187, 2008.

106. M. D. Abràmoff, P. J. Magalhães, and S. J. Ram, Image Processing with imageJ, *Biophotonics Int.*, Vol. 11, pp. 36–41, 2004.

107. P. Iassonov, T. Gebrenegus, and M. Tuller, Segmentation of X-Ray Computed Tomography Images of Porous Materials: A Crucial Step for Characterization and Quantitative Analysis of Pore Structures, *Water Resour. Res.*, Vol. 45, pp. 1–12, 2009.

108. D. Müter, S. Pedersen, H. O. Sørensen, R. Feidenhans'l, and S. L. S. Stipp, Improved Segmentation of X-Ray Tomography Data from Porous Rocks Using a Dual Filtering Approach, *Comput. Geosci.*, Vol. 49, pp. 131–139, 2012.

109. F. Brun, L. Mancini, P. Kasae, S. Favretto, D. Dreossi, and G. Tromba, Pore3D: A Software Library for Quantitative Analysis of Porous Media, *Nucl. Instruments Methods Phys. Res. Sect. A Accel. Spectrometers, Detect. Assoc. Equip.*, Vol. 615, no. 3, pp. 326–332, 2010.

110. W. M. Harris, J. J. Lombardo, M. B. DeGostin, G. J. Nelson, H. Luebbe, J. A. Schuler, J. Van Herle, J. C. Andrews, Y. Liu, P. Pianetta, Y. C. Karen Chen, J. Wang, and W. K. S. Chiu, Three-Dimensional Microstructural Mapping of Poisoning Phases in the Neodymium Nickelate Solid Oxide Fuel Cell Cathode, *Solid State Ionics*, Vol. 237, pp. 16–21, 2013.

111. D. Bouvard and F. F. Lange, Relation between Percolation and Particle Coordination in Binary Powder Mixtures, *Acta Metall. Mater.*, Vol. 39, no. 12, pp. 3083–3090, 1991.

112. W. M. Harris and W. K. S. Chiu, Determining the Representative Volume Element Size for Three-Dimensional Microstructural Material Characterization, Part 1: Predictive Models, *J. Power Sources*, Vol. 282, pp. 552-561, 2015.

113. W. M. Harris and W. K. S. Chiu, Determining the Representative Volume Element Size for Three-Dimensional Microstructural Material Characterization, Part 2: Application to Experimental Data, *J. Power Sources*, Vol. 282, pp. 622-629, 2015.

114. C. Metcalfe, O. Kesler, T. Rivard, F. Gitzhofer, and N. Abatzoglou, Connected Three-Phase Boundary Length Evaluation in Modeled Sintered Composite Solid Oxide Fuel Cell Electrodes, *J. Electrochem. Soc.*, Vol. 157, pp. B1326–B1335, 2010.

115. W. M. Harris, K. S. Brinkman, Y. Lin, D. Su, A. P. Cocco, A. Nakajo, M. B. DeGostin, Y. K. Chen-Wiegart, J. Wang, F. Chen, Y. S. Chu, and W. K. S. Chiu, Characterization of 3D Interconnected Microstructural Network in Mixed Ionic and Electronic Conducting Ceramic Composites, *Nanoscale*, Vol. 6, no. 9, p. 4480, 2014.

116. L. Zhang, N. Xu, X. Li, S. Wang, K. Huang, W. H. Harris, and W. K. S. Chiu, High CO2 Permeation Flux Enabled by Highly Interconnected Three-Dimensional Ionic Channels in Selective CO2 Separation Membranes, *Energy Environ. Sci.*, Vol. 5, no. 8, p. 8310, 2012.

117. G. J. Nelson, K. N. Grew, J. R. Izzo, Jr., J. J. Lombardo, W. M. Harris, A. Faes, A. Hessler-Wyser, J. van Herle, S. Wang, Y. S. Chu, A. V. Virkar, and W. K. S. Chiu, Three-

Dimensional Microstructural Changes in the Ni–YSZ Solid Oxide Fuel Cell Anode during Operation, *Acta Mater.*, Vol. 60, no. 8, pp. 3491–3500, 2012.

118. M. E. Lynch, D. Ding, W. M. Harris, J. J. Lombardo, G. J. Nelson, W. K. S. Chiu, and M. Liu, Flexible Multiphysics Simulation of Porous Electrodes: Conformal to 3D Reconstructed Microstructures, *Nano Energy*, Vol. 2, no. 1, pp. 105–115, 2013.

119. C. D. Lorenz and R. M. Ziff, Universality of the Excess Number of Clusters and the Crossing Probability Function in Three-Dimensional Percolation, Vol. 8147, p. 14, 1998.

120. Ł. Kurzawski and K. Malarz, Simple Cubic Random-Site Percolation Thresholds for Complex Neighbourhoods, *Reports Math. Phys.*, Vol. 70, no. 2, pp. 163–169, 2012.

121. Q. Cai, C. S. Adjiman, and N. P. Brandon, Investigation of the Active Thickness of Solid Oxide Fuel Cell Electrodes Using a 3D Microstructure Model, *Electrochim. Acta*, Vol. 56, no. 28, pp. 10809–10811, 2011.

122. K. Zheng, L. Li, and M. Ni, Investigation of the Electrochemical Active Thickness of Solid Oxide Fuel Cell Anode, *Int. J. Hydrogen Energy*, Vol. 39, pp. 12904–12912, 2014.

123. M. B. DeGostin, A. A. Peracchio, T. D. Myles, B. N. Cassenti, and W. K. S. Chiu, Charge Transport in the Electrospun Nanofiber Composite Membrane's Three-Dimensional Fibrous Structure, *Submitted*, 2015.

124. J. Choi, K. M. Lee, R. Wycisk, P. N. Pintauro, and P. T. Mather, Nanofiber Network Ion-Exchange Membranes, *Macromolecules*, Vol. 41, pp. 4569–4572, 2008.

125. T. D. Myles, K. N. Grew, A. A. Peracchio, and W. K. S. Chiu, Transient Ion Exchange of Anion Exchange Membranes Exposed to Carbon Dioxide, *J. Power Sources*, 2015.

126. D. H. Reneker, A. L. Yarin, H. Fong, and S. Koombhongse, Bending Instability of Electrically Charged Liquid Jets of Polymer Solutions in Electrospinning, *J. Appl. Phys.*, Vol. 87, no. 2000, pp. 4531–4547, 2000.

127. M. M. Hohman, M. Shin, G. Rutledge, and M. P. Brenner, Electrospinning and Electrically Forced Jets. II. Applications, *Phys. Fluids*, Vol. 13, no. 2001, pp. 2221–2236, 2001.

128. B. Dong, L. Gwee, D. Salas-De La Cruz, K. I. Winey, and Y. A. Elabd, Super Proton Conductive High-Purity Nafion Nanofibers, *Nano Lett.*, Vol. 10, pp. 3785–3790, 2010.